STUDY OF AN All-VANADIUM PHOTOELECTROCHEMICAL CELL FOR HIGH-EFFICIENCY SOLAR ENERGY STORAGE

by

ZI WEI

Presented to the Faculty of the Graduate School of

The University of Texas at Arlington in Partial Fulfillment

of the Requirements

for the Degree of

DOCTOR OF PHILOSOPHY

THE UNIVERSITY OF TEXAS AT ARLINGTON

August 2016

Acknowledgements

First of all, I would like to express deepest gratitude to my advisor and committee chair, Professor Fuqiang Liu, who guide me and inspire me with his genius: He taught me the essences doing research—a pure attitude of unveiling the truth and never give up. Without his guidance and encouragement, I've not be able to finish this dissertation or make it through my 5 years of graduate studies.

I want to express my appreciation to committee members, Professor Choong-Un Kim, Professor Yaowu Hao, Professor Kyungsuk Yum, Professor Brian Dennis and Professor Desheng Meng for their time and valuable suggestions. I would also like to thank Dr. Jiechao Jiang, David Yan for their efforts to help me using the facilities in CCMB, and Jennifer, Beth who helped me a lot in my life and studies.

In addition, I would like to thank my lab mates, Amir H Salehi Gilani, Dr Md. N Siddique, Dr Syed D Sajjad, and Hsiao-Chien Wu. They always share ideas with me and I learned a lot from them. Dr Chia Jen Hsu, Dr Dong Liu and Yi Shen worked closely with me on this project, without their support and contribution I cannot go this far. I Also I want to thank my dear friend Lixue Tong, Qianyun Xu, Xin Zhou, Wenjing E,Yijia Zhao, Mengyin Yuan, Minghui Zhang, Huandi Gu, Cancan Xu, Yuan Shi, Feng Mei, Yun Liu, Xing Wang, Yuan Zheng, Jie Zhao who are always there for me during my PhD study when I face difficulties. I also want to thank my first teacher, Yi Hou, she is the one who taught me to be kind, patient and strong.

Finally, I would like to express my gratitude to the love of my parents, Xubo Wei and Hong chen, they gave me the precious life and raise me up, and always being the sunshine in my heart.

To the memory of my dear grandfather, Kuan Chen.

August 15, 2016

Abstract

STUDY OF AN All-VANADUIM PHOTOELECTROCHEMICAL CELL

FOR HIGH-EFFICIENCY SOLAR ENERGY STORAGE

Zi Wei, PhD

The University of Texas at Arlington, 2016

Supervising Professor: Fuqiang Liu

In an attempt to explore a clean and renewable alternative to existing energy sources such as fossil fuel, we studied the feasibility of using vanadium redox species to store the inexhaustible solar energy via photoelectrochemical (PEC) reactions with photogenerated charge carriers from semiconductor photocatalysts such as TiO_2. Based on our fundamental study of the compatibility of vanadium redox and TiO_2, modification of TiO_2 such as carbon coating and geometry enhancement, and development of a continuous-flow solar energy storage cell, we demonstrated high-efficiency solar energy storage cell.

The research focuses on the following four directions. Firstly, a highly-efficient all-vanadium (all-V) PEC storage cell (PESC) has been developed. It showed a Faradaic efficiency of 95% without external bias and 12% incident photon-to-current efficiency (IPCE) at 350 nm. This PEC cell takes advantage of fast electrochemical kinetics of vanadium redox couples of VO^{2+}/VO_2^{+} and V^{3+}/V^{2+}. The charge carriers created on the

employed TiO_2 photocatalyst have been demonstrated to be able to convert the two pairs of vanadium active species.

Secondly, the amount of carbon coating on the surface commercial p25 TiO_2 in the photoelectrode has been tuned through a facile high-temperature sintering procedure, which enhanced the photocurrent of the all-V PESC. The applied carbon coating was demonstrated to be beneficial to the conductivity of the photoelectrode in the all-V PESC, as it provides an interconnected layer for the transport of photogenerated charge carriers.

Thirdly, a unique stirring-assisted hydrothermal synthesis method has been developed to create geometrically enhanced TiO_2 nanobelts (TNBs), resulting a doubled photocurrent in the all-V PESC. The all-V PESC demonstrated a peak IPCE of ~22% without any external bias, double that of commercial P25 TiO_2 (~11%) that we used in the previous case.

Finally, an all-vanadium continuous-flow PEC cell was designed, resulting in 5 and 3 times increase in photocurrent and state of charge (SOC), respectively, compared to the all-V PESC with stagnant electrolytes. The improvement was mainly ascribed to the enhanced electrochemical charge transfer as well as boosted PEC reactions introduced by the forced convective flow.

Table of Contents

List of Illustrations

List of Tables

Chapter 1

Introduction and Overview

The goal of this research is to explore efficient storage of the inexhaustible solar energy using an all-vanadium photoelectrochemical cell which provides a sustainable solution to the existing problem of energy shortage.

There is an increasing demand for utilization of solar energy. As a natural fusion reactor, the sun produces unfathomable amount of energy which has been harnessed by human beings since ancient times, by means of solar thermal power. Ever since the discovery of the photoelectric effect by Edmond Becquerel in 1839, to efficiently convert solar energy into electricity or clean chemical fuels at low cost has become a critical and primary mission for scientists [1]. Photovoltaic cells have enabled semiconductors such as doped silicon to capture the sun light to generate electron-hole pairs and then electricity.

The rising popularity of using solar energy has been driven by the increasing energy demand together with the drastic climate change. Until now, our energy sources have been dominated by fossil fuels (82% share in global mix), which will be used up eventually. Besides, utilization of fossil fuels creates greenhouse gas emissions that lead to disastrous consequences for the earth - “a damaged planet” [2]. The growing concerns for energy depletion as well as environment deterioration stimulate the search for clean, eco-friendly and renewable energy solutions. Currently, the dominance of fossil fuels has been challenged by renewable energy sources (RESs), which possesses enormous potential if utilized properly, and they can meet many times the world’s energy demand [3]. The most extensive RESs (19% of world’s energy production in 2007) in application are hydroelectric, photovoltaic (PV), and wind [4]. Other RESs such as biomass, solar thermal, geothermal are also playing their important roles in specific areas or applications.

Among them, the sun light provides the most gigantic amount of energy. Every hour, the solar energy striking onto the earth is more than the entire global energy needs in a year. It is indisputable that the scale of the sun as solar energy resource is huge; the question is how to increase the efficiency of power conversion at the same time decreasing the prime cost.

There are several issues that need to be addressed to efficiently utilize solar energy: the conversion efficiency, the cost of facility and equipment, the extent of environment benignity, and most important, the intermittency. Conventional photovoltaic technologies mostly employ doped silicon/amorphous silicon based photoelectrode. The highest efficiency for confirmed terrestrial cells achieved by single junction GaAs thin film is 29% [5]. These solid-state materials present reasonable high efficiency and good reliability, but require delicate fabrication procedure and high capital cost [6].

The most serious challenge for this type of solar cells is that their electricity generation is related the availability of the sun (e.g., night and cloudy weather) [7]. To overcome the intermittent nature of solar power, an energy storage capability integrated with energy generation unit can be most desirable. One famous process called photoelectrochemical (PEC) water splitting has received massive attention since its discovery in 1972 by Fujishima and Honda, in which hydrogen and oxygen can be liberated from water, either by PEC process or photocatalysis [8]. Yet the storage and transportation of hydrogen as the solar fuel remain a severer issue. In this regard, tremendous amount of efforts have been devoted to innovative processes for efficient solar energy conversion and storage. Several pioneer works integrating energy storage systems such as supercapacitors, lithium-ion batteries and redox flow batteries in solar energy conversion have shown great promise for efficient capturing and storing the solar

energy simultaneously [9-13]; however, highly efficient solar energy storage still remains a great challenge.

In this research, a series of study have been carried out to develop an efficient solar energy conversion and storage system. First, aiming to build a prototype all-vanadium PESC storage system, the feasibility and operating conditions of the device was investigated. Faradaic efficiency of 95% without external voltage bias and incident photon-to-current efficiency (IPCE) at 350 nm light of 12% were achieved by the fast kinetics of the vanadium species. Subsequently, the light absorbing and converting component, i.e., TiO_2 photoanode, has been modified with a facile procedure to create amorphous carbon coating at the surface, resulting in improved photocurrent due to the enhanced photogenerated charge carrier separation. Then a unique stirring assisted hydrothermal synthesis method was adopted to geometrically tune morphology of TiO_2 nanobelts, and the PEC performance of the all-vanadium system has been enhanced by 2 times using TiO_2 nanobelts in comparison with commercial p25 TiO_2. The photocurrent representing the electrochemical performance of the TiO_2 photoanode has been found to be enhanced with increased stirring speed during the synthesis since higher energy facets of TiO_2 were exposed. Moreover, a continuous-flow all-vanadium PEC cell was developed to further improve efficiency of solar energy storage. Both the photoccurent and the depth of charging of the continuous-flow solar energy storage cell have been enhanced by 5 times and 3 times, respectively.

Chapter 2

Background and Objective

2.1 Overview

In this chapter, the prevalent semiconductors for solar cells and photocatalyst materials will be first introduced, followed by the two innovative approaches of storing sun light: solar to fuel and solar battery. Then the overall objective and organization of this dissertation will be discussed.

2.2 Research towards Improved Solar Energy Utilization

2.2.1 Light absorbing materials.

The “golden triangle” for solar energy harvesting includes cost, efficiency and durability. Currently, the goal of constructing commercial silicon solar panels is to achieve 25 years of operation life time and a payback period of less than 2.5 years. Although we’ve seen a dramatic decrease of the primary cost of Si based solar cells (Figure 2-1 (a) and (b)), scientists and engineers are still working together to lower the price of relatively high efficient photoactive materials. Clearly, for a sustainable photovoltaic (PV) market, to lower the price of the PV devices while maintaining considerable efficiency and maximized stability is the inevitable trend of this field. To this end, numerous innovative ideas evolved aiming at building a cost-effective solar energy harvesting device, especially in the material perspective, such as single crystal, polycrystalline, thin film, organic, earth abundant, and quantum dot materials. This section will provide a brief discussion about such photoactive materials.

2.2.1.1 Crystalline Silicon

Crystalline silicon based PV devices lean on a flat Si substrate, where a p-n junction is formed by doping which allows charge separation to produce photocurrent and

photovoltage. The capital cost of commercial Si solar panel has decreased by 20% due to the progress of technology, and energy conversion efficiency of Si based solar panels ranges from 16 to 21% [14]. Through optimized manufacturing processes, including polymer packaging, screen-printing and systemic production of Si wafers, a sustained construction of solar panel has been realized [15]. To further reduce the cost, integration of wider band-gap materials or architecture of scalable higher-efficiency tandem devices can be the direction for future Si based solar panel development.

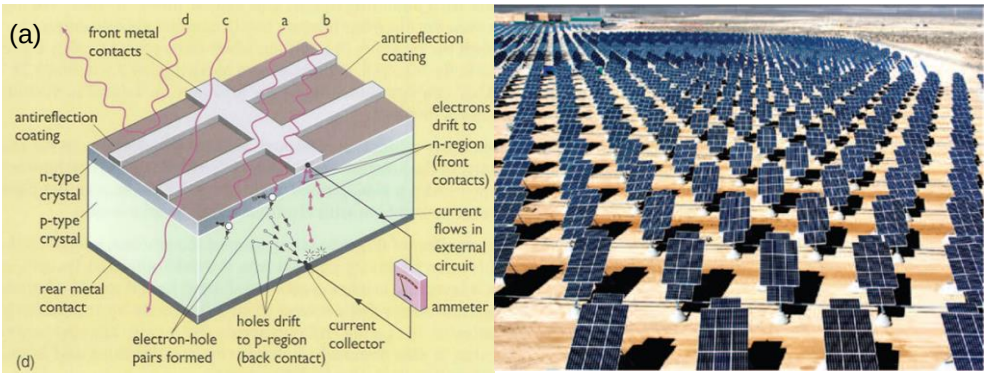

Figure 2-1 (a) Schematic of a solar cell. (b) Nellis Solar Power Station, a 14-MW PV installation at Nellis Air Force Base, NV.

2.2.1.2 Gallium Arsenide

Single junction and multijunction photovoltaic devices which employ highly efficient Gallium arsenide and other “III–V” materials are expensive and often utilized on satellites [5]. Compared to Si (band gap 1.1ev with 100μm thickness), GaAs (band gap 1.43ev) based solar cells have thin films (few micrometers in thickness) for absorbing the sun light. Geometry design such as one-dimensional (1D) and 2D, as well as implementation of low cost methods are deployed to grow highly efficient GaAs material.

2.2.1.3 Thin Film

Thin-film materials such as hydrogenated amorphous Si, CdTe, and $CuInGaSe_2$ are emerging due to their low cost. The main drawbacks of CdTe and other thin film

materials are low conversion efficiency, difficulties of doping, scarcity of Te resources, relatively lower efficiency compared to Si, large resistance and tendency of charge recombination. Studies of CdTe have been focused on investigating the instability, carrier transport, diffusion length, depletion width, primary hetero/back junction, grain-boundary passivation and tuning junction thickness to address the performance issue of the device, e.g., incorporation of CdS to reduce the recombination at the junction interface of CdTe. The reduced system installation cost is the major subsequent advantage of using thin-film PV materials. The toxicity issue, which is related with Cd pollution and draws great concerns in Europe, has been resolved with active material encapsulation and recycle programs.

The past four years have seen unprecedentedly rapid emergence of perovskites materials such as $CaTiO_3$ [16]. The power conversion efficiency of lead halide perovskite based thin film photovoltaic devices has increased from 3.8% to 17% with the dramatic development through simple deposition techniques [17]. The real challenge of this type of material is to enhance the long-term stability over a broad range of conditions.

2.2.1.4 Earth-abundant light absorbers

Zn_3P_2, $ZnSnN_2$, and Cu_2O are earth-abundant light absorbers that receive renaissance recently ever since their discovery in 1980s [18]. Studies involve understanding the fundamental properties of such materials and investigation of their toxicity upon dissolution in water, as well as their efficiency and durability. Complex factors such as environmental, economic, technological and politics need to be taken into considerations in development of solar energy harvesting systems.

2.2.1.4 Organic PV cells

Research of organic PV cells involves chemical control over the compositional properties and junction components of the system [19]. Poly-phenylenevinyelene (PPV)

based bulk heterojunction organic solar cell has received intensive attention. To achieve long term stability of the solar cell, side reactions of the organic materials under full spectrum need to be eliminated. Dye sensitized solar cells (DSSCs) utilizing molecular sensitizers will be discussed in the later part of this chapter [20].

2.2.1.5 Quantum-confined systems

Inorganic quantum dots capture photons that have twice greater energy of its band gap, while polymer quantum dots proceed the similar singlet fission process [21, 22]. This property results in breakthroughs in the theoretical limit of conventional Shockley Queisser single junction material, and the high photovoltage has been obtained by quantum confinement effect. The multijunction cells also exceed the theoretically limit which present more than 40% light conversion efficiency under high concentration illumination [5].

2.2.2 Solar to fuel

2.2.2.1 H_2

In 2010, the annual production of hydrogen reaches 40 million tons and it has been utilized in the production of ammonia, petroleum and other chemicals, such as to form methane through the Sabatier reaction, to create hydrocarbons combined with carbon monoxide through the Fischer–Tropsch process, to synthesize methanol with carbon dioxide, and to generate synthetic gasoline from liquefied coal.

As a clean and renewable fuel, hydrogen only produces water during combustion process other than hydrocarbon fuels that emits CO_2 to the atmosphere. For example, hydrogen gas can be efficiently transferred to electricity in fuel cells. The current prevailing method to produce hydrogen is through splitting methanol or via electrolysis of water.

Photoelectrochemical generation of hydrogen, as a way to store solar energy, is

capturing a lot of attention recently. The “brute force” approach is to use a set of silicon photovoltaic cells connected in series to generate electricity that is subsequently passed into a commercial-type water electrolyser. However, solar-to-chemical conversion efficiency obtained from such system is only ~7%. Much higher efficiencies in the range of 12-20% have been reported [23, 24] based on III/V semiconductors, but these materials are expensive for large-scale terrestrial applications.

On the other hand, *in-situ* PEC generation of hydrogen and oxygen by photocatalyst [25], from water by reactions with photo-generated electrons and holes has been widely studied. In 1972, Fujishima and Honda proposed PEC water splitting, and this solar to fuel approach has been studied extensively ever since its discovery [8]. TiO_2 was employed as the semiconductor photocatalyst and hydrogen can be released in PEC reactions using photogenerated charge carriers. This artificial photosynthesis is actually based on enduring blueprint that nature provides. The green plants absorb sunlight and convert it to chemical energy, for example, to split water, and release oxygen and NADPH.

Figure 2-2 displays the water splitting mechanism (herein TiO_2 has been employed as an exemplary photocatalyst)—TiO_2 absorbs sun light, the absorbed photon excites an electron from the valence band of TiO_2 and leaves a hole (an electron vacancy). The hole oxidize H_2O into O_2 at the TiO_2 surface, while the electron conducts through the external circuit to the other electrode, typically Pt, and reduce H_2O into H_2. With this process, H_2 can be collected for future usage [26].

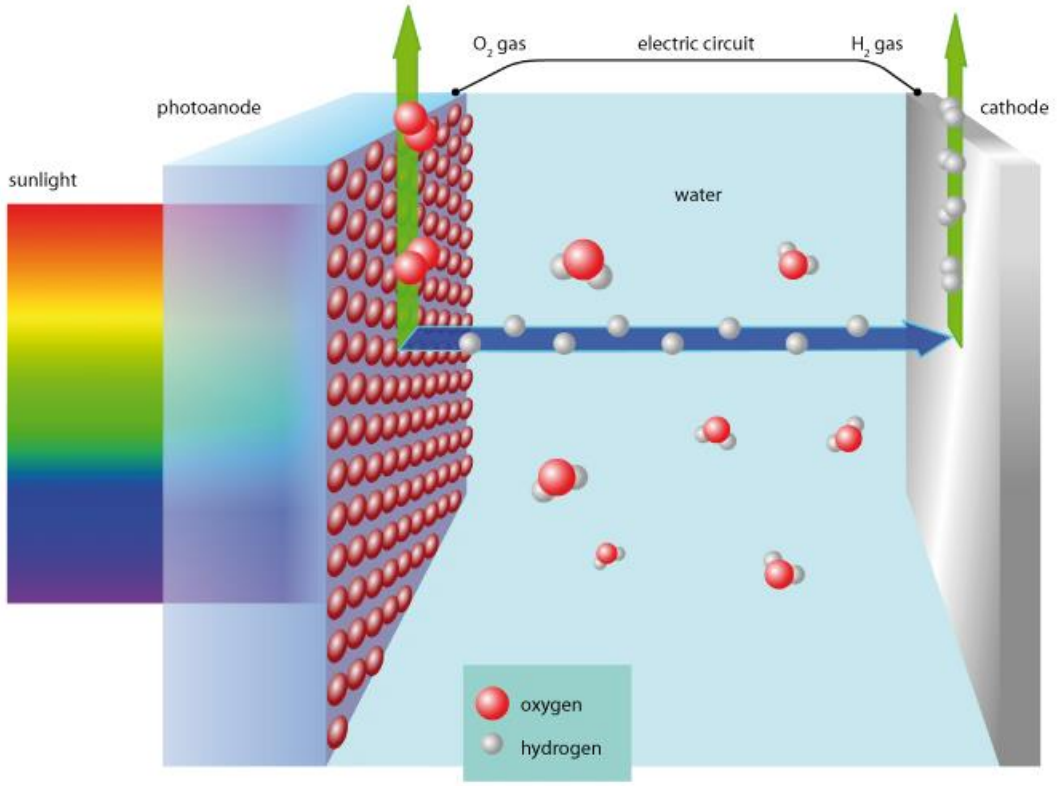

Figure 2-2 Illustration of photocatalytic water splitting to produce hydrogen and oxygen.

The uphill PEC reaction is described as:

$$H_2O \rightarrow H_2\,(g) + 1/2O_2\,(g) \quad \text{.....2.1}$$

The thermodynamic barrier of such reaction is gentle, with a 237.178 Kj/mol Gibbs free energy, corresponding to a 1.229V electrochemical potential and the light source with less than 1mm wavelength (visible and near-infrared light, consisting 80% of full solar spectrum) can be captured.

On top of this, the PEC cell can be built by incorporating photocatalysts such as TiO_2 into the light absorbing electrode, and hydrogen is generated at the cathode while oxygen is created at the anode in two independent chambers.

While much progress [27-29] has been made since the pioneering experiments [30] more than 30 years ago, efficient and cost-effective photocatalytic water splitting is in need. For optimal photogeneration of hydrogen, the desired semiconductor must have band gap energy within the visible light spectrum, and its band edges must be beyond the potential range of hydrogen and oxygen evolution. More than 100 inorganic materials have been studied as photoelectrochemical water splitting catalyst [31]. TiO_2 receives the most intensive attention due to its high conversion efficiency, low cost and durability. However, its large band gap (3.0 eV) corresponding to UV light needs to be compensated by doping or co-catalyst to capture visible light. Doping creates localized light absorption centers, shifts conducting/valance band edges, but introduces large amount of trap states that reduce the mobility of holes leading to an intensified electron hole recombination. WO_3, $BiVO_4$, and Fe_2O_3 absorb a large portion of solar spectra to split water, and only with the presence of sacrificial electron accepters such as Ag^+ under an external bias due to their positive conduction band or negative valence band compared to hydrogen or oxygen redox potentials [32-34]. Developing stable and narrow-band-gap semiconductors has been attempted by varying metal cations [35-37], doping [38-46], sensitization [47-51], and employing co-catalyst [52-57] and metal nanoparticles (NPs) [58]. Yet these strategies may not lend themselves to practical implementation because of the difficulty in matching the band gap energies with hydrogen and oxygen evolution potentials, high cost, as well as photocorrosion. It has been a challenge to develop ideal semiconductors with the required photoactivity and durability.

In addition, one of the most important limitations of photocatalysis of water splitting is that the process is rather inefficient primarily due to the fact that reduction/oxidation of water are complex multistep reactions which require significant overpotential, especially at the photoanode (oxygen evolution). As a compromise, the

common practice relies on sacrificial molecules such as alcohol or NaS/Na_2SO_3 mixtures as electron donors to improve H_2 production, as holes are scavenged by these molecules and recombination is greatly reduced. However, to maintain sustainability the sacrificial additives have to be constantly replenished and the waste products have to be removed. Most important, since conduction bands of most stable semiconductors are not negative enough to drive hydrogen evolution reaction (the band structure is just a thermodynamic requirement but reaction kinetics of photocatalytic hydrogen generation requires more negative value), the highest quantum yield reported is only 5.9% at 420-440nm [59], far below the commercializable value of 30% at 600nm [37].

Moreover, some fundamental elements of solar energy storage/conversion by splitting hydrogen from water may be missing. For example, although molecular hydrogen has very high energy density on a mass basis, as the gas at ambient conditions, it has very low energy density by volume. Pressurization and liquefaction increase volumetric density, but both techniques require energy and so further reduce the net energy ratio of the hydrogen. Besides, both forms of hydrogen storage are prone to leaks. Hydrogen in storage will leak at a rate of at least 1.7% per day [60]. In fact, all forms of pure hydrogen are difficult to store. Moreover, sluggish kinetics of photolysis of water and gas evolution reactions contributes to a low efficiency.

2.2.2.2 Carbon Dioxide to fuel

Gasoline is one of the major energy resources for transportation and living, and limited reserves of fossil fuel (gasoline and diesel) renders the energy crisis. It is estimated that every year due to combustion of hydrocarbon fuels, the CO_2 that emits to the atmosphere is 40 billion metric tons. To resolve the issue of greenhouse effect as a consequence of CO_2 emission, the most promising and environmentally benign approach is to utilize the inexhaustible solar energy. A number of promising technologies to

generate fuel from water and CO_2 under sun light with photocatalysts have been developed, such as coupling photovoltaics with water electrolysis, PEC cells and nanostructured catalyst suspension in liquid, to generate hydrocarbon fuels [61-63]. As early as 1970s, C1 hydrocarbons such as methane, methanol, formic acid were produced from CO, CO_2 and water in a photoelectrochemical reactor or CO_2-saturated aqueous solution [64, 65]. Other subsequent researches generate ethane, ethanol, acetic acid, propanol, butanol, pentane, hexane, olefins and branched paraffins, yet the detailed generation mechanism are missing. More recently, direct gas-phase photothermocatalytic synthesis of hydrocarbons including liquid alkanes, aromatics, and oxygenates (carbon numbers ranges from C1 up to C13) has been proposed through which a sustainable and carbon-neutral liquid fuel cycle could be realized [66, 67]. However, this photothermochemical process requires elevated operating temperature ranging from 110°C to 200°C and a flow photo electrochemical reactor.

2.2.3 Solar to chemical energy

2.2.3.1 Dye Sensitized Solar Cell (DSSC)

In 1991, Graztel et al reported a low cost, dye-coated TiO_2 based high-efficiency dye sensitized solar cell, which exhibits commercially realistic light-to-electric conversion efficiency of 12% in diffuse day light [68]. The 10 μm thin film, which consists of colloidal TiO_2 nanoparticles (a few nano meters in size), is coated with a mono layer trimeric ruthenium complex, absorbing 46% of solar spectrum and converting 80% incident photon to electric current.

Studies of this type of cell have been mostly focused on the photocatalyst materials and dyes. For example, highly ordered transparent TiO_2 nanotube arrays of 46-nm pore diameter, 17-nm wall thickness and 360-nm length (the thickness of the photocathode is also 360nm) have been grown perpendicularly on a fluorine-doped tin

oxide (FTO) substrate through anodic oxidation followed by $TiCl_4$ treatment, and was then integrated into a DSSC sensitized by a ruthenium dye. Under simulated AM 1.5 illumination the photocurrent reaches 7.9mA/cm^2 with a 2.9% efficiency. With the highly ordered TiO_2 arrays, the electron lifetimes are greatly enhanced with uniform pathways for electron transport [69]. As an alternative to the mainstream metal oxide substrate such as FTO and ITO (Indium Tin oxide), ultrathin graphene films are obtained from graphite oxide exfoliation [70]. These films are transparent (more 70 %), conductive (550 S/cm) and chemically and thermally stable.

Different dyes have been attempted. An amphiphilic heteroleptic ruthenium complex sensitizer *cis*-RuLL combined with a quasi-solid-state polymer gel electrolyte for triiodide/iodide, reached an efficiency of >6% in air mass full sunlight (100 mW cm^{-2}) while maintaining thermostability [71]. Molecularly engineered cobalt complexes have inappreciable absorption in the visible light, and they can substitute the traditional I_3^-/I^- redox shuttle redox in DSSCs [72]. A SM315 porphyrin dye has a donor–π-bridge–acceptor structure which is compatible with cobalt (II/III) redox shuttle electrolyte and has improved light absorption, exhibiting an open-circuit voltage of 0.91 V, short-circuit current density of 18.1 mA cm^{-2}, fill factor of 0.78 and a power conversion efficiency of 13% [73].

Besides, ultra-fast charge separation in DSSCs was revealed by a femtosecond time-resolved diffuse reflectance spectroscopy. It is discovered that charge injection from the Z907 dye in TiO_2 morphologies takes place in the sub-200 fs time scale rather than the generally accepted microseconds scale while the charge separation in Y123 dye based DSSCs happens in a longer time scale of two picoseconds [74].

2.2.3.2 Solar Battery

As alternative to solar to fuel production, previous attempts employ rechargeable batteries [75, 76] in photoelectrochemical energy storage, integrating hydrogen bromine-imbedded Si system (Texas Instruments) and fuel cells into a regenerative system, and solid-phase storage couples such as Ag^{+}/Ag and Cu^{2+}/Cu for higher capacity. Besides, research has been carried out during 1980s utilizing redox couple to store solar energy. Photocatalysts such as $BaTiO_3$, n-Pb_3O_4, n-Fe_2O_3, n-SrTiO, were coupled with two sets of redox pairs including Cr^{4+}/Cr^{3+} and Fe^{3+}/Fe^{2+}, Fe^{3+}/Fe^{2+} and IO_3^{-}/I^{-}, Fe^{3+}/Fe^{2+} and I_2/I^{-}, and $Fe^{3+}/Fe^{2+}$with $Fe(CN)_6^{3-}/Fe(CN)_6^{4-}$ [77]. It has been proved that the match between the photocatalyst and redox pairs can lead more effective charge separation. However, efficiency obtained in those systems is yet to be improved due to lack of efficient photocatalysts and kinetically fast reversible redox species.

More recently, photoelectrochemical solar energy storage underwent a remarkable renaissance [13, 78], in part due to availability of many reversible redox pairs, such as iron/chromium, all-vanadium, vanadium/bromine, bromine/polysulfide, zinc/bromine, etc. [79]. These redox species have been widely employed in low-cost and large-scale energy storage systems, i.e., redox flow batteries, for application in power grid and renewable sources [80]. However, one question that still remains is how photoelectrochemical efficiency can be improved by developing state-of-the-art novel materials in combination with recent advances in electrical energy storage.

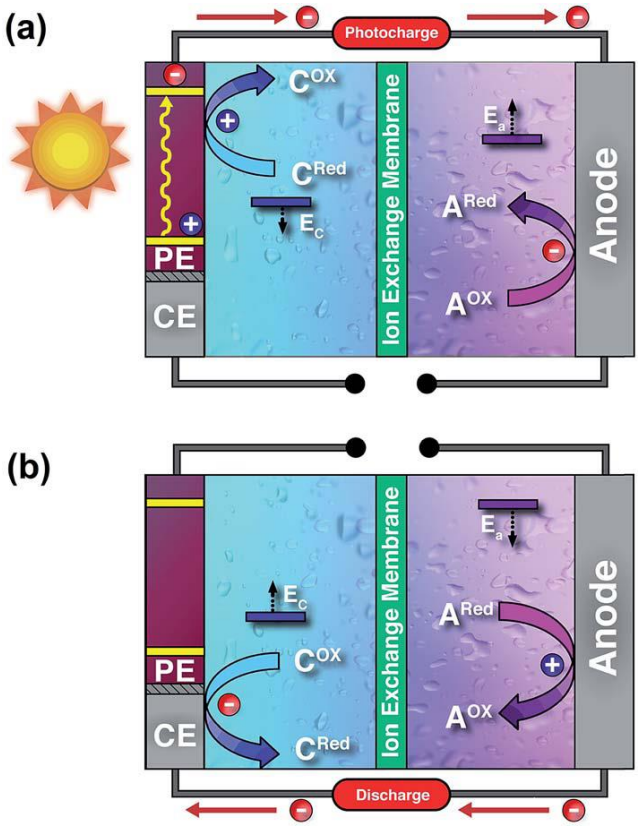

Figure 2-3 General operating principle of a solar battery

Figure 2-3 illustrates the general operating principle of a solar battery. The two yellow bands (upper and lower) on the photoelectrode (PE) represent the semiconductor's conduction band minimum (CBM) and valence band maximum (VBM) [81]. Upon illumination, as illustrated in Figure 2-3 (a) the PE absorbs incident photons and generates electron–hole pairs (equation 2.2). The photo-generated holes present in the valence band diffuse to bulk electrolyte and oxidize the catholyte (equation 2.3), while the photo-generated electrons in the conduction band move to the anode side through the external circuit and reduce anolyte redox species (equation 2.4). A charge balance is realized by net ion transport through the separator. At the same time, the Nernst potential of the C^{ox}/C^{red} couple (E_c) increases while the Nernst potential of the A^{ox}/A^{red} couple (E_a)

reduces with the energy input from photogenerated electrons and holes.

$$PE + hv \rightarrow e^- + h^+ \text{.....2.2}$$

$$h^+ + C^{red} \rightarrow C^{ox} \text{ .....2.3}$$

$$e^- + A^{ox} \rightarrow A^{red} \text{ .....2.4}$$

In the process of discharging, shown in Figure 2-3 (b), the cathode and anode are connected to an external load. Electrical current from the anode into the cathode, driven by the electrochemical energy stored during the photocharging process, reduces the catholyte and oxidizes the active species on the anode side according to equation 2.5 and 2.6:

$$C^{ox} + e^- \rightarrow C^{red} \text{ .....2.5}$$

$$A^{red} \rightarrow A^{ox} + e^- \text{ .....2.6}$$

The concept of sulfur based solar batteries was first proposed by Hodes et al. in 1976 [82]. They used polycrystalline CdSe (1.4 eV) as the PE immersed in an aqueous S/S^{2-} electrolyte, the conduction band bottom of this material locates at -1.0 V (vs. NHE). The redox potential of $S/S^{2-}$and Ag_2S/Ag couples lies at -0.45 V at pH of 14 and –0.69 V, respectively, which is thermodynamically favorable for the electrochemical oxidation of S^{2-} and reduction of Ag^+. In 1987, Licht et al constructed a solar battery using a piece of single crystalline $Cd(Se_{0.65}Te_{0.35})$ semiconductor as the PE, a CoS thin film as the CE, and a polysulfide-based aqueous electrolyte (1.0 M Cs_2S_4, 0.8 M CsHS and 0.8 M CsOH) as the catholyte [83].

In 2002, Hauch and Orel et al. proposed the first I_3^-/I^- redox based solar battery adopting a two-electrode design with a N3-senstized TiO_2 mesoporous PE [84]. They utilized a LiI/LiI_3/propylene carbonate (PC) catholyte, and a Pt-coated counter electrode (CE), a WO_3 layer underneath the PE acting as the anode. I_3 anions are produced in the catholyte by regenerating the oxidized dye molecules. Segawa's group reported an

optimized three-electrode design in with a LiI/LiI_3/MeCN catholyte solution mixture, and the anolyte was a $LiClO_4$/MeCN solution separated by a Li^+-Nafion membrane. They investigated a conducting polymer, polypyrrole (PPy) on FTO substrate via electro-polymerization deposition, as the anode material [85]. Gao et al explored iodine redox flow solar batteries, which is advantageous in terms of mass energy storage since the energy capacity of the system can be simply varied by changing the amount of the catholyte and anolyte, similar to redox flow batteries (RFBs) [78]. They attempted a $DMFc^+$/DMFc redox couple as the anolyte, LiI/LiI_3/$LiClO_4$/PC as the catholyte, which are chemically reversible). They also investigated the feasibility of using the Li_2WO_4/$Li_{2+x}WO_4$ and quinoxaline redox couples which showed higher working voltage of 0.8 V compared to 0.6 V of their first design [86]. However, the low ion conductivity of the ceramic membrane separator renders a large voltage polarization and low efficiency of their design for large-scale application. In 2015, Wu et al. proposed the concept of a photoassisted aqueous lithium–iodine (Li–I) solar flow battery [11]. They use the dye-sensitized TiO_2 as the PE, the I_3/I^- couple as the catholyte, and the Li^+/Li couple as the anolyte. An external voltage input is required for the charging process under illumination since the redox potential of the Li^+/Li couple (-3.04 V) is much more negative than the conduction band of TiO_2. 20% of energy was saved compared to conventional Li-I batteries due to the sunlight input. Several intrinsic drawbacks of the Iodine based solar battery need to be addressed before practical implementation, such as high molecular weight of iodine, the relatively low energy storage specific capacity of the iodine catholyte, the difficulty of back-side illumination, visible light absorption of the triiodine/iodine catholyte, and poison of metals due to the corrosive nature of iodine electrolyte.

2.4 Objective and Scope of Studies

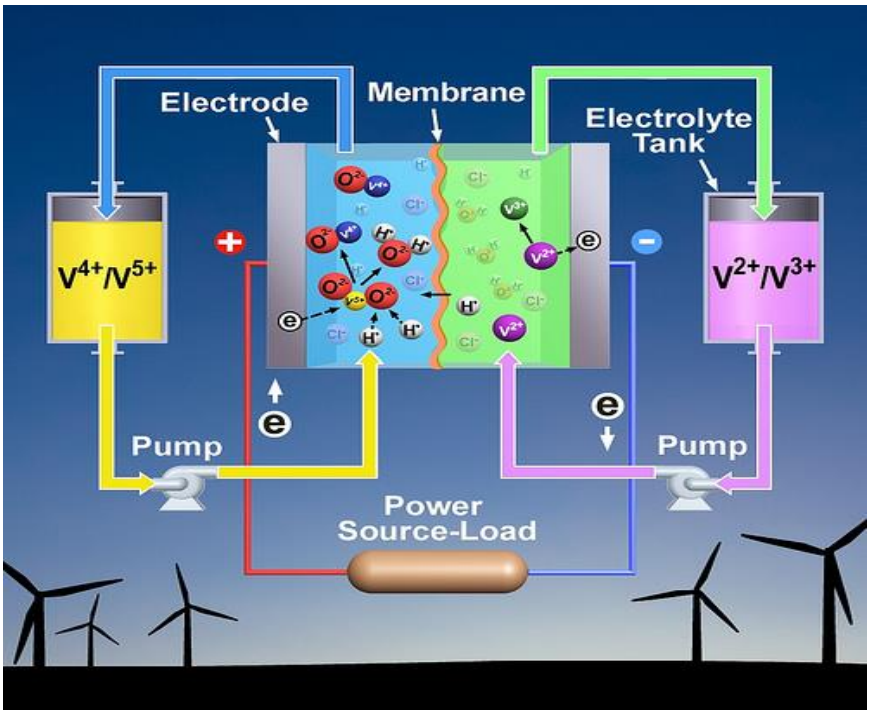

Figure 2-4 Schematic of all vanadium redox flow battery [87].

The primary objective of this study is to integrate all-vanadium redox flow batteries and photoelectrochemical devices for efficient solar energy storage. This research is driven by a central hypothesis that the solar energy storage efficiency and capacity can be dramatically improved by employing an all-vanadium photoelectrochemical cell using nanostructured semiconductors as photocatalyst. In general, true flow batteries with redox-couple reactants that remain in the liquid form during both photocharge and discharge are advantageous since they provide excellent efficiencies, decoupled and scalable power and energy, and reasonable storage volumes. It is worth underlining that our approach obviates the need for externally hooking up a PV system with a battery and in this regard, and shares much of the same logic behind a PEC water splitting device as opposed to a hybrid PV-water electrolyzer combination.

Our design takes advantage of all-vanadium redox flow batteries, compared to other electrochemical devices, offering advantages for long cycle life and high efficiency. An all-vanadium redox flow battery (VRFB, Figure 2-4) consists of a positive and a negative electrode which are in contact with the anolyte and catholyte, respectively. A membrane separates the two electrolytes and allows selective conduction of ionic charges. Compared to other types of flow batteries, VRFBs have obvious advantages of eliminating cross-contamination of electrolytes since both the catholyte and anolyte contain the same redox species. During charge or discharge cycles, electricity is instantly converted to chemical potential (charge) or the other way around (discharge) at electrodes while the liquid electrolytes flow through the cell. This process is the same as traditional batteries which can store and release electricity. The other merit of VRFBs rather than conventional batteries is that energy is stored in liquid electrolytes instead of electrodes. In this sense, the power storage capacity is not limited by the size of electrodes but can be extended by increasing volume of electrolyte storage tanks.

Figure 2-5 Different oxidation states of vanadium ions

As indicated in Figure 2-5, vanadium has four oxidation states: V^{2+}, V^{3+}, VO^{2+}, and VO_2^+. During charge and discharge of a VRFB, the following electrochemical reactions take place at the cathode and anode (equation 2.7 and 2.8), respectively [79]:

$V^{2+} \leftrightharpoons V^{3+} + e^-$, E_0 =0.26V vs. RHE.....2.7

$VO^{2+} + H_2O \leftrightharpoons VO_2^+ + 2H^+ + e^-$ E_0 =1.00V vs. RHE.....2.8

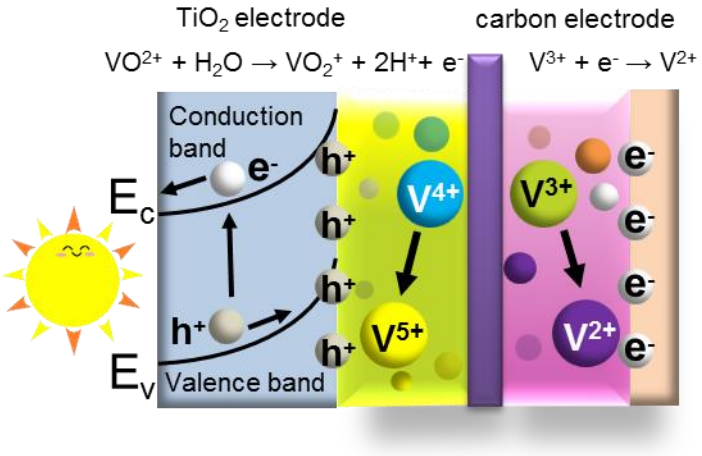

Figure 2-6 The energy diagram of a solar battery of an all-V PESC.

In this study, the vanadium electrolyte species are chosen because of their fast kinetics which allows them to quickly scavenge photogenerated electrons and holes thus reducing recombination at the photo catalyst surface. Upon illumination, as illustrated in Figure 2-6, the TiO_2 photoanode absorbs incident photons and generates electron–hole pairs. The photo-generated holes present in the valence band diffuse to bulk electrolyte and oxidize the VO^{2+} to VO_2^+, while the photo-generated electrons in the conduction band move to the anode side through the external circuit and reduce V^{3+} redox species to V^{2+}. A charge balance is realized by net ion transport through the separator nafion 117. Nanostructured TiO_2 photocatalysts are selected because they are widely applied in photoelectrochemistry due to their stability and low cost [88]. Utilizing two reversible photoelectrochemical reactions of vanadium ions, changes taking place in the system during illumination can be reversed in the dark when the generated chemical change drives a spontaneous discharge reaction. The key advantage of using vanadium redox

couples is that they are photoelectrochemically reversible (*i.e*., facile oxidation and reduction), stable and kinetically fast. This will significantly improve charge transfer at semiconductor-electrolyte interface, leading to both enhanced energy efficiency and depressed photocorrrosion [89]. Besides, by using the all-vanadium system the storage capacity of the storage cell could be improved. The theoretical energy density of 10M of redox ions (assuming reaction of one ion releases one electron) is much higher than the ambient and closed to 100-atm hydrogen. Most important, up to 95% of charge/discharge round-trip efficiency reported for the redox species [90] (*e.g.,* VO_2^+/VO^{2+} and V^{3+}/V^{2+}) would raise the "practical" energy density equivalent to the hydrogen at 200 atm pressure with an assumed efficiency ~ 35% (the chemical to electrical energy conversion efficiency achieved in a typical H_2 fuel cell).

Research in this Ph.D. dissertation is organized in four stages: a) developing an all vanadium photoelectrochemical storage cell (all-V PESC) as a proof of concept; b) optimizing the porous photoelectrode from material perspective, i.e., tuning the carbon coating at the surface of TiO_2 photocatalyst to enhance electron transport; c) creating nanostructured semiconductors, i.e., TiO_2 nanobelts using a unique stirring-assisted hydrothermal synthesis, for improving efficiency in solar energy storage; and d) developing a continuous-flow PESC to increase the energy storage performance and extend the state of charge during photocharge with the aid of forced convective flow of electrolytes.

Chapter 3

Development of All-Vanadium Photolectrochemical Cell

3.1 Introduction

A highly-efficient all-vanadium photoelectrochemical storage cell has been demonstrated in this chapter. This storage cell takes advantage of fast electrochemical kinetics of vanadium redox couples of VO^{2+}/VO_2^{+} and V^{3+}/V^{2+}, and appears as a promising alternative to photoproduction of hydrogen from water. Continuous photocharging for 25 h revealed a VO^{2+} conversion rate of 0.0042 μmol/h and Faradaic efficiency of 95% without external voltage bias. The incident photon-to-current efficiency (IPCE) at 350 nm light was calculated to be ~12%.

In this chapter, for the first time, we demonstrated combining PEC energy storage with a vanadium redox-flow battery (VRB), a well commercialized energy storage system for large-scale terrestrial applications. Such an all-vanadium PEC storage cell possesses all merits inherent to VRBs: fast electrochemical kinetics, high charge/discharge round-trip efficiency (up to 90% [91]), low capital cost, minimal safety issues. Our previous studies [92] have demonstrated facile photooxidation kinetics of VO^{2+} by a wide-band-gap TiO_2 photoanode, presenting the promise of a drastic enhancement in efficiency of the all-vanadium PEC storage cell.

3.2 Experiment

The schematic of the all-vanadium PEC storage cell is illustrated in Figure 3-1.The cell consists a TiO_2 working electrode as the photoanode, a Pt-mesh counter electrode, and two redox couples, i.e., VO_2^{+}/VO^{2+} and V^{3+}/V^{2+}, separated by a Nafion 117 membrane. 3M H_2SO_4 was used as the supporting electrolyte throughout the experiments. The photoanode on a fluorine doped tin oxide (FTO) glass was fabricated using a slurry consisting of 0.5 g TiO_2 powders (VP AEROPERL® P

25/20), 0.25 g ethyl cellulose, 0.062 g polyvinylidene fluoride (PVDF), and 2.15 g α Terpineol. After sintering in air the photoelectrode had a thickness of 10 μm and an active area of 6.45 cm^2.

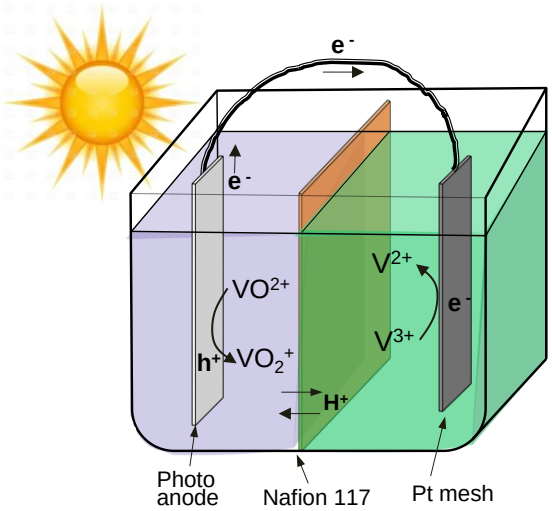

Figure 3-1 Schematic illustration of the all-vanadium redox PEC storage cell.

Photoelectrochemical studies were conducted using a potentiostat (Princeton Applied Research, PARSTAT 2273) and a customized two-chamber H-cell. Electrolytes of 0.01 and 0.1M VO^{2+} were prepared by dissolving $VOSO_4 \cdot xH_2O$ (99.9%, Alfa Aesar) in 3M H_2SO_4. The V^{3+} solution was prepared from a VO^{2+} electrolyte in an electrochemical cell with static electrolyte under a constant current of 3 mA according to references [93, 94]. The light source was an ozone-free solar simulator system (Newport, USA). A 300 W Xe lamp with a series of long-pass filters was used to illuminate the photoelectrode. Small amount of the electrolyte in a quartz cuvette was analyzed using a UV-Vis spectrophotometer (PerkinElmer Lambda 35) to determine the electrolyte composition change. For the incident photon-to-current efficiency (IPCE) measurements, the wavelength of the incident

light was controlled by a monochromator (Optometrics). The IPCE was calculated according to the following equation 3.1:

$$IPCE = (1240I)/(\lambda \cdot J_{light}) \quad .....3.1$$

where I (A/cm^2) is the measured photocurrent density at a specific wavelength, λ (nm) is the wavelength of incident light, and J_{light} (W/cm^2) is the light irradiance determined by a photodetecter (Newport, USA). Photocurrent was measured under Zero Resistance Ammetry (ZRA), i.e., short-circuit conditions.

3.3 Result and discussion

Figure 3-2 compares the proposed all-vanadium redox PEC storage with photocatalytic water splitting in terms of TiO_2 band positions and the corresponding PEC reactions. Figure 3-2 (a) indicates that the TiO_2 conduction band (CB) electrons may not be energetic enough to drive hydrogen evolution reaction, because the band structure is just a thermodynamic requirement but the sluggish reaction kinetics of photocatalytic hydrogen generation [95] requires a large overpotential. However, for the all-vanadium PEC storage cell shown in Figure 3-2(b), though the CB bottom of TiO_2 (around -0.5 V on the potential scale vs. NHE) seems not to be negative enough to drive the reduction reaction of $V^{3+} + e^- \rightarrow V^{2+}$ (E_0 = -0.26 V vs. NHE), fast electrochemical reaction kinetics of the vanadium ions [96], which is several orders of magnitude higher than that of H_2 evolution, may compensate the narrow potential window and result in a significant improvement in photocurrent.

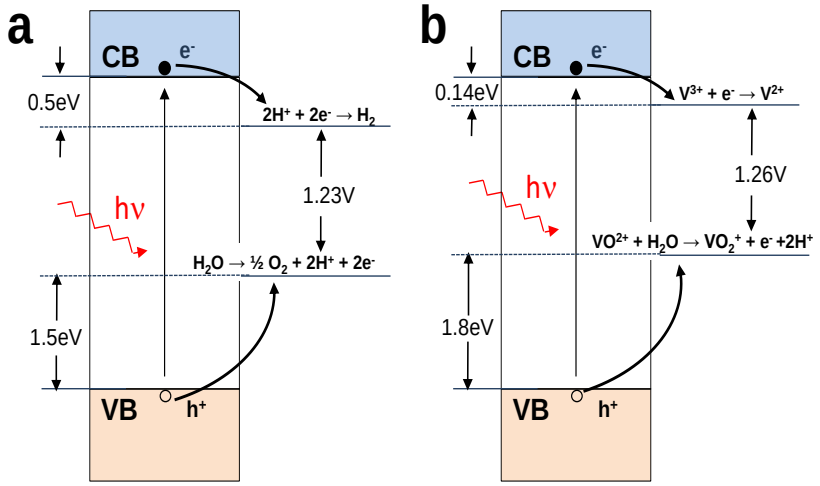

Figure 3-2 Band positions of TiO_2 and corresponding PEC reactions in (a) photocatalytic water splitting and (b) an all-vanadium redox PEC storage cell. CB and VB refer to conduction band and valence band, respectively. The energy differences between the semiconductor band edges and thermodynamic redox reactions are indicated in the figures.

The above analysis was confirmed by the PEC characterization of the storage cell in Figure 3-3 (a). Different combinations of electrolytes in a two-electrode setup were studied using zero resistance ammetry method without external voltage bias. Upon illumination, immediately there appeared the photocurrents whose magnitudes were closely dependent on the type of electrolytes. The photocurrent using 0.1 M vanadium redox species as both the anolyte and catholyte increased ca. 30% compared to that using 0.01 M, indicating that kinetics of adsorption/desorption and mass transport of the vanadium ions in the electrolyte, rather than their concentration, dominates the reactions. In addition, when the 0.1 M VO^{2+} and V^{3+} electrolytes in the all-vanadium PEC storage cell were replaced by 3 M H_2SO_4 at the photoanode (green curve in Figure 3-3(a)) and cathode (black curve), respectively, a

significant decrease of photocurrent was observed. For example, the photocurrent, taken at 120 s just before the air mass (AM) 1.5 filter was switched off, reduced 11.2 times when the catholyte was changed from 0.1 M V^{3+} to 3 M H_2SO_4 (the anolyte remained unchanged). This indicates that contribution of photocatalytic water splitting to the photocurrents measured from the all-vanadium PEC storage cell is negligible, even though very low molarities of vanadium ions (0.01 M and 0.1 M) were used.

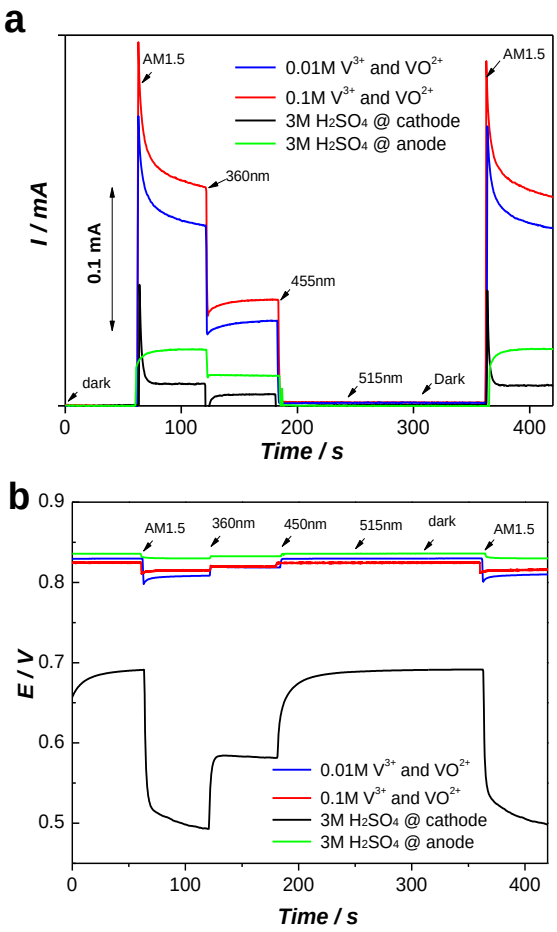

Figure 3-3 Photoelectrochemical response of the all-vanadium PEC storage cell to switching electrolyte solutions. (a) photocurrent and (b) cell voltage. A series of long-pass filters with different cut-on wavelengths were used to study the influence of light irradiation.

Figure 3-3 (b) presents the cell voltages as a function of time. The measured voltage between the photoanode and Pt counter electrode was determined by the quasi-Fermi level of the TiO_2 and the redox potentials of the electrolytes. When the Pt counter electrode (cathode) was in contact with 3 M H_2SO_4, the cell voltage was, as expected, lower than that of the all-vanadium PEC storage cell since the thermodynamic potential of H_2O/H_2 (0.0 V vs. NHE) is higher than that of V^{3+}/V^{2+} (-0.26 V vs. NHE). On the other hand, when the VO^{2+} electrolyte was replaced with 3 M H_2SO_4 as the anolyte, the change in cell voltage was barely noticeable even though the thermodynamic potential of O_2/H_2O (1.23 V vs. NHE) is about 200 mV higher than that of VO^{2+}/VO_2^+ (1.0 V vs. NHE). This may be related to the slow kinetics of PEC water splitting and extra overpotential is therefore needed to produce a photocurrent of similar magnitude.

It is worth mentioning that the test conditions in this work are fundamentally different to what has been conventionally reported for photoproduction of hydrogen. When hydrogen is produced in the electrolyte, it is naturally separated thus eliminating any reverse reaction, i.e., discharge reactions. However, in the all-vanadium PEC storage cell, spontaneous reverse reactions may occur along with the photocharging, which reduces the conversion efficiency. To study this effect, a continuous 25h photocharging was conducted using 0.01 M VO_2^+ and V^{3+} as the anolyte and catholyte, respectively. Low molarity was used to ensure short photocharging time and detectable change in concentration of vanadium ions. Figure 3-4 shows a rapid decrease of photocurrent in the first 2 hours as a result of fast depletion of vanadium ions at the electrode/electrolyte interface, followed by a relatively stable photocurrent when equilibrium has been established. The sporadic spikes of photocurrent were caused by 120s dark periods that were intentionally introduced to examine the dark current. The currents reduced to almost zero upon

applying the dark periods, indicating a quick PEC response of the cell to illumination. The slight increase of photocurrents when light was resumed is due to re-establishment of the equilibrium between ion diffusion and reaction at the electrode surface. The inserted plot in Figure 3-4 (a) shows that the cell voltage increased during the photocharging, clearly suggesting that the all-vanadium PEC storage cell was being charged. Besides, in the all-vanadium PEC storage cell photogenerated holes are expected to be quickly scavenged to depress photocorrosion. Initial tests indicated that the photoanode was very stable in the vanadium electrolyte, suggesting the likelihood of long-term stable operation of the all-vanadium PEC storage cell.

To calculate the Faradaic efficiency, the anolyte was assayed using UV-Vis spectroscopy to determine the concentration of VO^{2+}. Assuming a linear relationship between the absorbance at the characteristic peak of VO^{2+} (at 765 nm) and concentration, i.e., the Beer's Law [97], the estimated anolyte concentration as a function of photocharging time is shown in the inset of Figure 3-4 (a). The photooxidation of VO^{2+} occurred quickly at the beginning of photocharging since more VO^{2+} was consumed, then slowly after 10h. The conversion rate of VO^{2+} over the entire test period is estimated at 0.0042 μmol/h. The Faradaic efficiency, defined as $\eta_F = F \cdot \Delta n / \Delta Q$, where Δn is the amount of reacted VO^{2+}, F is the Faraday's constant, and ΔQ is the charge, is calculated to be 95%.

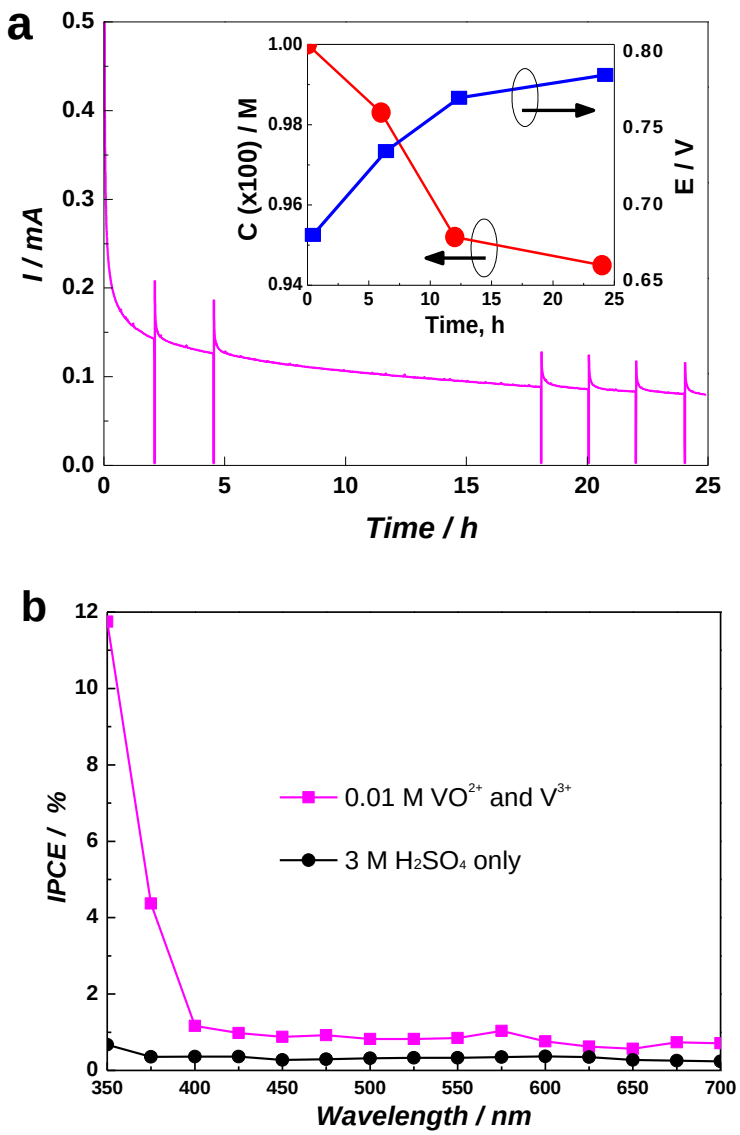

Figure 3-4 (a) Continuous 25h photocharging under AM 1.5 illumination using a TiO_2 photoelectrode. The inset shows the variation of cell voltage and VO^{2+} concentration in the anolyte. (b) IPCE spectra of the PEC storage cell with (0.01M VO^{2+} and V^{3+}) and without (3M H_2SO_4 only) vanadium redox species, collected at the incident wavelength range from 350 to 700nm using the ZRA method.

The incident photon-to-current efficiency (IPCE) of the all-vanadium PEC storage cell using 0.01 M vanadium ions is shown in Figure 3-4 (b). The all-vanadium PEC storage cell shows a much higher efficiency, particularly in the UV region, than the case where no vanadium ions were added. For example, at 350 nm light illumination, the IPCE of the former is close to 12% whereas the latter only shows an efficiency of 0.8%. This is due to the much faster electrochemical kinetics of the vanadium ions as previously discussed that could yield considerable photocurrents even at low concentrations (0.01 M). Further work should focus on optimization of the vanadium electrolyte and developing visible light sensitive semiconductors.

3.4 Conclusion

We have demonstrated, for the first time, a unique all-vanadium PEC storage cell for highly efficient solar energy storage. In the storage cell, two electrochemically reversible vanadium redox pairs were utilized to enhance photocurrent and energy conversion efficiency, and depress photocorrosion of the photocatalysts. A Faradaic efficiency of 95% and VO^{2+} conversion rate of 0.0042 μmol/h have been achieved in a continuous 25h photocharging. The IPCE under UV light of 350 nm was ~12% using 0.01M vanadium redox species.

Chapter 4

Carbon coated TiO_2 Photoanode for All-V PESC

4.1 Introduction

In this chapter, a carbon coated TiO_2 photoelectrode was designed in the all-vanadium redox photoelectrochemical cell. Facile high-temperature sintering approach was employed to tailor the amount of the carbon coating at the TiO_2 photoanode. Considerable enhancement in photocurrent has been observed using the carbon coated TiO_2 photoanode in the all vanadium photoelectrochemical system when compared to the carbon-free counterpart. Particularly, the photoanode containing 2.07 wt% of carbon displayed 40% improvement in photocurrent compared to the one with bare TiO_2 as the photoanode. It is proposed that the carbonaceous species created by high-temperature pyrolysis acted as a thin adsorption layer on the TiO_2 for vanadium redox to react with the photogenerated holes. Photocurrent enhancement of the carbon coated photoelectrodes is ascribed to a synergic effect between enhanced charge separation and high electronic conductivity.

4.2 Experiment

Herein, we utilized a simple sintering process at 500°C under N_2 flow to obtain the carbon coating on TiO_2 surface followed by post heat treatment in air for different duration time to tune the thickness. Three different CCT photoelectrode using commercial Degussa P25 TiO_2 were fabricated using the same carbon precursor (ethyl cellulose) but with different sintering procedures. The first electrode was sintered according to reference [94], labeled as BT (stands for bare TiO_2, as all of the carbon is removed by O_2). The other two electrodes were first sintered under N_2 at a heating rate of 10 ^oC/min till 500 ^oC and then the temperature was maintained for 30 min to preserve the carbon sources. The electrodes were subsequently treated in air at 500 °C for different time

periods such as 10 min and 30 min to tailor the amount of carbon in the photoelectrodes, respectively, designated hereafter as CCT10 and CCT30. The existence of carbon coating on TiO_2 was confirmed and studied by several characterization methods such as Raman spectroscopy, UV-vis diffuse reflectance spectra as well as energy dispersive X-ray spectroscopy (EDX).

The All-V PESC was assembled using a membrane-separated (Nafion 117) H-cell as shown in Figure 4-1. The anolyte (VO^{2+}) and catholyte (V^{3+}) were prepared according to reference [94]. A Pt mesh was employed as the counter electrode in contact with the catholyte (V^{3+}) while a Ag/AgCl electrode was placed in the anolyte (V^{4+}) chamber as a reference electrode (RE).

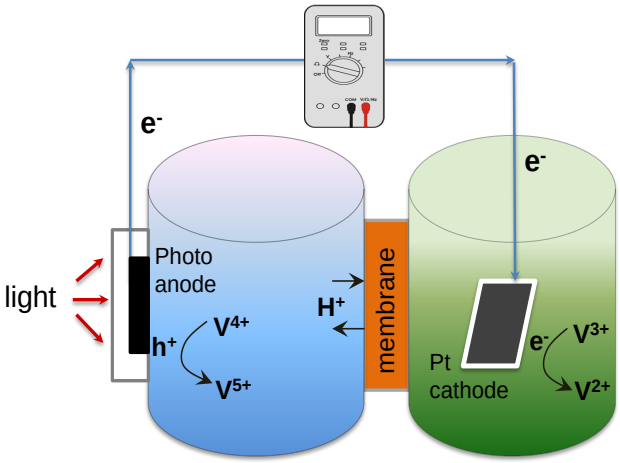

Figure 4-1 Schematic illustration of an all-V PESC. The carbon coated TiO_2 photoanode and a Pt counter electrode are coupled with two sets of reversible vanadium redox pairs (separated by a Nafion 117 membrane), *i.e.,* VO_2^+ (V^{5+})/VO^{2+}(V^{4+}) and V^{3+}/V^{2+}, which are oxidized and reduced by the photogenerated holes or electrons, respectively.

4.3 Result and discussion

The carbon coating on semiconductors could play an active role in photocatalysis, according to references [98-101], due to a possibly synergistic effect of better

conductivity of TiO_2 photo anode and enhanced charge transfer. Figure 4-2 indicates that heat treatment in air for 10 min preserves noticeable amount of carbon as the CCT10 electrode appears dark. The high-resolution TEM image in Figure 4-3 clearly shows that the thickness of the carbon coating is about 10 nm. On the other hand, 30 min heat treatment in air is believed to have removed most of the carbon since the appearance of the CCT30 electrode is almost identical to that of the BT electrode. Furthermore, the cross-sectional EDX element mapping images of CCT10 in Figure 4-4 reveal that both Ti and O are evenly distributed at the surface of the electrode. The thin layer of carbon coating, contributing to the relatively less intensified but uniform C signals, is deposited at the TiO_2 surface and would potentially alter the photoelectrochemical performance of the photoanode [102]. The composition (Table 4-1) of the three elements, i.e., titanium, oxygen and carbon in the photoelectrodes, was determined using EDX. The different weight percentage of carbon clearly indicates that heat treatment is an effective tool to tailor carbon content in the photoelectrodes.

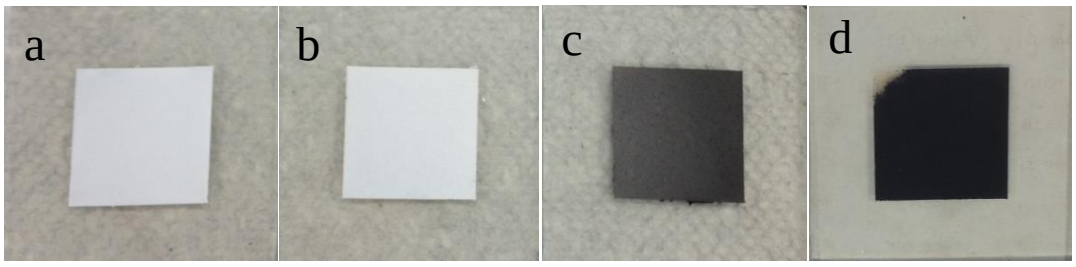

Figure 4-2 The appearance of the photoelectrodes: (a) BT, (b) CCT30, and (c) CCT10. (d) An electrode obtained under N_2 protection sintering.

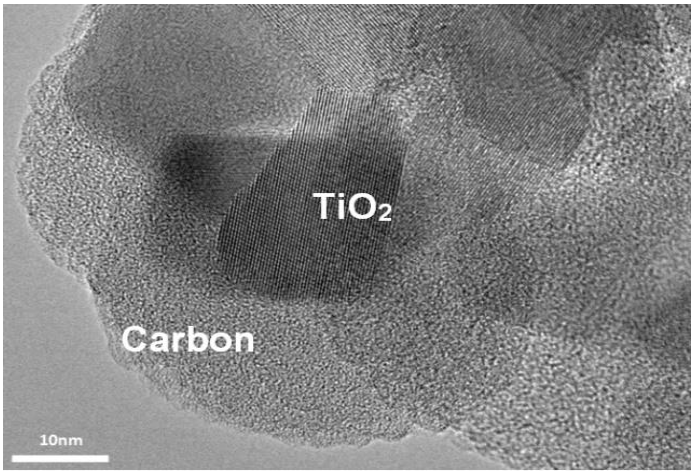

Figure 4-3 High-resolution TEM image of CCT10 sample after heat treatment in air at 500°C for 10 min.

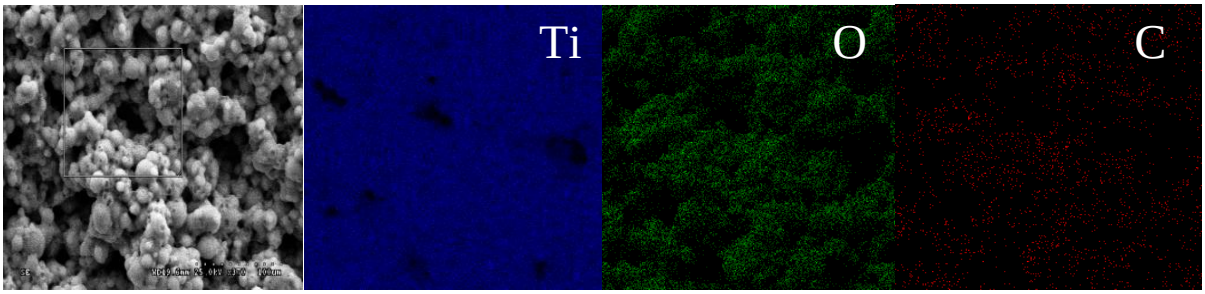

Figure 4-4 EDX elemental mapping of the CCT10 photoelectrode.

Table 4-1 Element composition of various photoelectrodes measured using EDX

	C		O		Ti	
	Wt %	**At %**	**Wt %**	**At %**	**Wt %**	**At %**
BT	1.22	3.03	28.42	53.08	70.36	43.89
CCT30	1.41	3.52	27.79	52.13	70.8	44.35
CCT10	2.07	5.25	25.58	48.72	72.35	46.03

The Raman spectra shown in Figure 4-5 (a) of the TiO_2-based photoelectrodes clearly demonstrate characteristic TiO_2 peaks between 100 and 700nm. BT and CCT30 show much intensified TiO_2 peaks than CCT10. However, the characteristic carbon bands, i.e., D and G at around 1300 and 1600 nm, respectively, only appear in the CCT10 sample. This indicates that the thin layer of carbonaceous species that cover the TiO_2 particles in CCT10 attenuates the Raman signal resulting less intensified signal. The absorbance by carbon species is confirmed by the UV-vis diffuse absorbance spectra in Figure 4-5 (b). The absorbance curve of the BT electrode is typical TiO_2 spectra with a sharp absorption edge near 380nm. For CCT30 and CCT10, the absorption edge undergoes a red shift which may be caused by the carbonaceous species. A significant absorption increase was observed between 400 and 650nm, and the extent of this increase was in good correlation with the amount of the carbon in the photoelectrodes.

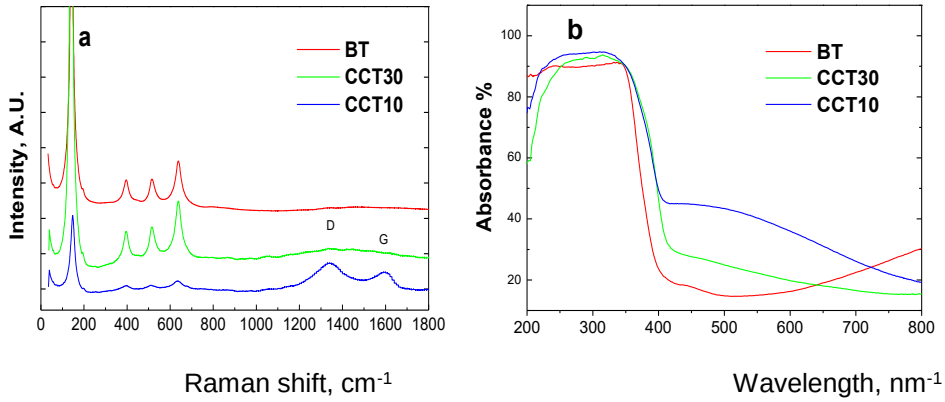

Figure 4-5 Experimental characterization of different photoelectrodes. *(*a) Raman spectra where characteristic D and G bands of carbon are labeled. (b) UV-vis diffuse absorption spectra.

The photoelectrochemical behavior of the TiO_2-based photoelectrodes in the all-V PESC was investigated using Zero Resistance Ammetry (ZRA). In the all-V PESC, all

vanadium redox pairs serve as the energy storage media while the photoelectrode converts solar energy into electrochemical energy: when sun light strikes on the TiO_2 semiconductor, photogenerated charge carriers are created and they can react with the vanadium redox pairs. The photo generated holes would oxidize VO^{2+} (V^{4+}) into VO_2^+ (V^{5+}). Meanwhile the electrons reduce V^{3+} to V^{2+} at the counter electrode. During these processes, the carbon coating at the TiO_2 surface could assist in charge transfer due to its good conductivity thus reducing electron/hole recombination. On the other hand, the VO^{2+} ions adsorption at the surface of the carbonaceous species would accelerate their reaction with the photogenerated holes.

Figure 4-6 (a) shows the photoelectrochemical response of the three photoelectrodes under on and off cycles of light (AM1.5). The anolyte and catholyte solutions were 0.01 M VO^{2+} (V^{4+}) and V^{3+}, respectively. The CCT30 electrode, with less carbon content, produces comparable photocurrent with the BT electrode (0.123 mA). As expected, CCT10 exhibits the highest photocurrent, which may result from efficient electron-hole separation enabled by the carbon coating. As only 0.01 M VO^{2+} was used in the photoanode compartment, the enhanced photoresponse (0.175mA) can be attributed to adsorption of VO^{2+} (V^{4+}) on the carbonaceous species followed by mass transfer to the photoactive TiO_2 [103]. The enhanced electron-hole separation in CCT10 enabled by carbon is further confirmed by the lower photovoltage fluctuation under intermittent illumination of light (AM 1.5) displayed in Figure 4-6 (b). The charge separation process was triggered by the space charge layer formed between redox electrolytes and TiO_2, and therefore the extent of band bending plays an important role in the charge separation process, considering the difference of TiO_2 valence band (2.73 V vs. NHE) and redox potential of $VO^{2+}(V^{4+})/VO_2^+(V^{5+})$ (1.0 V vs. NHE). By incorporation of carbon, an ohmic contact between the TiO_2 and redox electrolyte is speculated. On the other hand,

analysis of photovoltage variation under intermittent light also suggests better photoelectrochemical kinetics of the CCT10 electrode. The voltage drops when light was switched on at ca. 180s in Figure 6 (b) was 51 mV for CCT10, which is considerably lower than those of CCT30 (95 mV) and BT (78 mV) electrodes. The results were also consistent with the photocurrent measurements. The relatively small variation of photovoltage of CCT10 implies enhanced transport of charger carriers, as well as interfacial reaction kinetics between VO^{2+} (V^{4+}) and TiO_2.

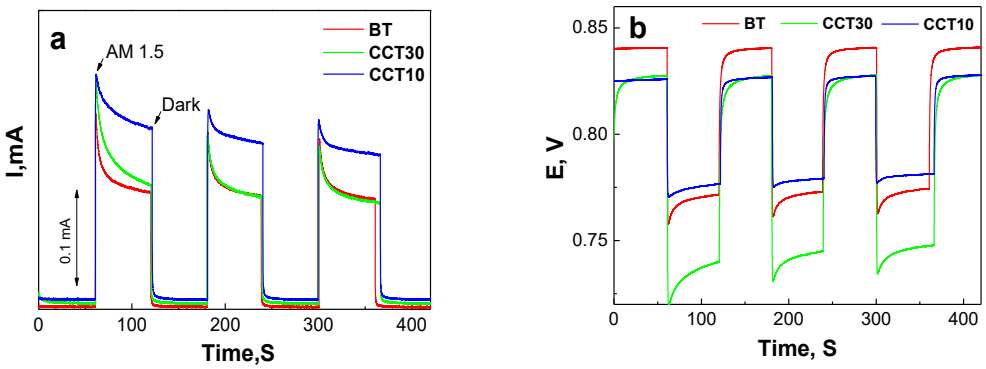

Figure 4-6 Photoelectrochemical response of the all-V *PESC* when switching illumination (AM 1.5) on and off: (a) photocurrent and (b) photovoltage. A photoelectrode (anode) and a Pt mesh are in contact with 0.01M VO^{2+} and 0.01M V^{3+} (in 3M H_2SO_4), respectively.

Nevertheless, the quick response of photocurrent to switching light on and off, and relatively stable photocurrent are due to the electrochemically reversible vanadium redox species even though at very low concentrations. To understand the photoresponse of the electrodes under different light irradiation, the PEC performance was also investigated using a series of long-pass filters at different wavelengths (Figure 4-7). The CCT10 electrode showed improved photoresponse under both 360 nm and AM1.5 filters. However, the improvement vanished after applying optical filters with wavelength longer

than 455 nm. This result suggests that the photocurrent enhancement shown in Figure 6 (a) is only observed in the UV region. It was also discovered that a thicker layer of carbon on TiO_2 surface (the sample with carbon more than 10 wt%, without heat treatment in air, shown in Figure 4-2 (d) resulted in almost no photoresponse under light. This indicates that thickener carbon coating may obstruct access of light to the surface of TiO_2.

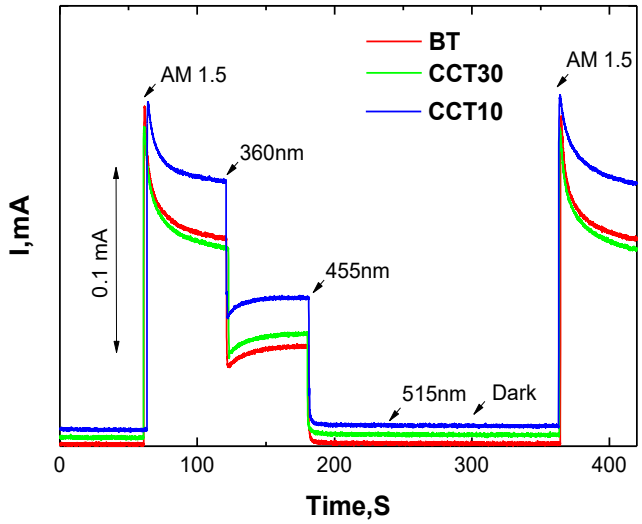

Figure 4-7. The Response of photocurrent of the all-V PESC when switching different optical filters.

The observed improvement in CCT10 and CCT30 could be attributed to enhanced charge separation and electrode conductivity. Figure 4-8 illustrates the detailed mechanism of carbon coating assisting in charge transfer during the photoelectrochemical process. Under light the photogenerated electrons migrate to the semiconductor surface and are quickly conducted through the connected network formed by conductive carbon to the Pt counter electrode where V^{3+} is reduced, while the photogenerated holes react with VO^{2+} (V^{4+}) ions that are adsorbed at the surface of carbon matrix to form VO_2^+ ions.

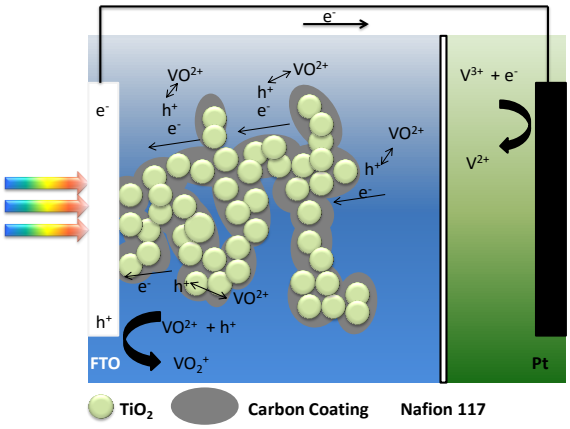

Figure 4-8 The schematic representation of the continuous carbon coating layer that assists in charges separation in the all-V PESC.

4.4 Conclusion

In this work, CCT photoanodes with different carbon contents were prepared by a facile sintering process under nitrogen protection. The electrochemical study of the photoanodes in the all-V PESC indicated that CCT10 with the highest carbon content produced the highest photocurrent of 0.175 mA. Further investigation by Raman spectra, UV-vis diffuse reflectance spectroscopy as well as TEM proved that the surfaces of TiO_2 nano particles was covered with a thin layer of carbon which accounts for the fast electron/hole separation and thus reduced charge recombination. We propose that this carbon coating on TiO_2 photoanode has two major contributions: (I) enhanced conductivity which allows faster charge transfer, and (II) adsorption sites for VO^{2+} (V^{4+}) ions facilitating electrochemical reaction with the photo generated holes. Therefore, this work indicates that creating a carbon coating on TiO_2 photoanode can be a fast and convenient approach at low cost to increase photoelectrochemical performance in our all-V PESC.

Chapter 5

TiO_2 Nanobelt TiO_2 Photoanode

5.1 Introduction

In this chapter, we developed geometry-enhanced ultra-long TiO_2 nanobelts (TNBs) to significantly improve solar energy storage efficiency in all-V PESC. The TNBs are synthesized using a simple stirring-assisted hydrothermal method, where the stirring speed is adopted to effectively tune the geometry and structure of the TNBs. We demonstrate that highly efficient solar energy storage is realized by ultra-quick oxidization and reduction reaction of vanadium ions with, respectively, holes and electrons produced on the TNB surface. The obtained incident photon-to-current efficiency (IPCE) is ~22% at 350 nm without any external bias, double that of commercial P25 TiO_2 (~11%). The observed improved efficiency results from enhanced photoactivity and charge separation in the semiconductor, and mass transport of vanadium ions in the photoelectrode.

The striking features of the all-V PESC originate from the extremely fast kinetics of vanadium redox (at least six orders of magnitude higher than oxygen evolution [92]), which, on one hand, could significantly minimize charge recombination at the TiO_2/electrolyte interface [92, 104-107], but, on the other hand, might also demand more stringent requirements on charge transport within the photoelectrode to accommodate the high photocurrent. However, it is well known that diffusion in nanocrystalline photoelectrodes is slow compared to single crystals. Grain boundaries between particles, in addition to surface trap states, contribute to poor diffusion in conventional TiO_2 nanocrystalline films. Eliminating or minimizing grain boundaries using oriented arrays of TiO_2, nanowires [108], nanorods [109], and nanobelts [110] could suppress charge recombination, and exhibit a higher diffusion coefficient than the nanocrystalline counterpart (e.g., ~200 times higher reported by Feng et al. [111]). Therefore, it would be

of great interests to exploit and integrate 1D geometry-enhanced TiO_2 in the newly developed all-V PESC.

We demonstrate how stirring-assisted hydrothermally synthesized geometry-enhanced ultra-long TiO_2 nanobelts (TNBs) can effectively double the photocurrent and IPCE for solar energy storage in an all-V PESC. For the first time, geometry and facet control of TNBs are simply realized by tuning the stirring speed, and their elongation as well photocatalytic activity are found to be proportional to the applied speed. This is considerably advantageous compared to conventional methods using shape-control agents, such as HF [112], surfactant [113] or diethanolamine [114], which require additional steps to remove these agents after formation of the TiO_2 nanostructure. This promising approach will be a critical step toward efficient solar energy storage and conversion in a PEC storage cell.

5.2 Experiment

5.2.1Synthesis of TNBs

A stirring-assisted hydrothermal synthesis method, developed in our previous study [115], was employed to synthesize the TNBs. Typically, 1.2 g anatase TiO_2 powder (Alfa Aesar) was added to 80 ml of 10 M NaOH solution with stirring for 30 min. Then 25 ml of the solution was transferred to a 50 ml Teflon-lined stainless steel autoclave with a reaction temperature at 200^{o}C under constant stirring at 0, 100, 250, 500, and 700 rpm for 48 h. After the system was cooled to room temperature, the product was first washed by 0.1 M HCl and then deionized water several times. After drying in the oven at 80^{o}C for 4 h, the product was annealed in a tube furnace at 700^{o}C for 1 h to convert the hydrogen titanate into TiO_2 TNBs.

5.2.2 Fabrication of Photoelectrodes

The above-synthesized oxide (0.5 g) was mixed with 2.15 g α-terpineol (Fisher Scientific, USA), and then sonicated for 20 min. Fluorine-doped tin oxide (FTO) glass substrates (2 in × 2 in) were prepared and cleaned by sonication in acetone (99.7%, Fisher Scientific, USA) for 20 min followed by methanol (99.8%, Fisher Scientific, USA) for 20 min, and then DI water. Degussa P25 (Evonik) and different TNB slurries were coated on the FTO glass substrates using a doctor blade to form uniform films and then dried in an oven at 80^{o}C for 2 h. The as-prepared photoanodes were sintered with air flow in a tube furnace at 500^{o}C for 1 h. The $TiCl_4$-treated photoanodes were prepared using 0.5M $TiCl_4$ solution in ethanol. One ml of the $TiCl_4$ solution was used to soak the active surface of the photoanodes, and then followed by heat treatment.

5.2.3 Materials Characterization

Powder XRD patterns were obtained using a diffractometer (Siemens, 810-M340-32-C3000). Scanning electron microscopy (Hitachi S-3000N variable pressure SEM and Hitachi S-4800 Field emission SEM) was used to examine the morphology of the photoanodes. Nanostructure of TNBs was studied using a high resolution transmission electron microscope (HR-TEM, Hitachi H-9500). UV-vis spectra of the photoanodes were obtained using a JASCO Corp V-570 spectrophotometer. Brunauer–Emmett–Teller (BET) surface areas were determined from N_2 adsorption using a Gemini VII 2390 surface area analyzer.

5.2.4 Photoelectrochemical Studies

The photodegradation test of methylene blue was conducted according to our previous study [115]. A portable UV lamp (4 W) at 360 nm wavelength was used as an irradiation source. 3 mg TiO_2 samples were dispersed in 10 ml MB solution under constant stirring in a quartz container, and then were irradiated by the UV lamp in a dark

room. The MB solution was extracted and analyzed by a UV-Vis spectrometer every 10 min. The overall MB photodegradation rate constants and specific degradation rate constants for different TNB samples were calculated based on the following equations:

$$\ln\left(\frac{C_0}{C}\right) = kt \quad \text{.....5.1}$$

$$k' = \frac{k}{S_A} \quad \text{.....5.2}$$

where C_0 is the initial MB concentration, C is the concentration at time t (min), k (min^{-1}) is the first-order rate constant, and k' (g m^{-2} min^{-1}) is the specific degradation rate constant.

The PEC experiments on different photoanodes in the all-V PESC [92, 104, 105, 116, 117] were performed using a PARSTAT 2273 potentiostat. In the all-V PESC, a Nafion 117 membrane was used to separate two different vanadium redox electrolytes, i.e., 0.01 M VO^{2+} and 0.01 M V^{3+} (balanced with 3 M H_2SO_4). The photoanode served as the working electrode (WE) in one chamber filled with VO^{2+}. A platinum mesh and an Ag/AgCl reference electrode served as the counter electrode and reference electrode (RE), respectively, in the other chamber filled with V^{3+}. Zero-resistance ammetry (ZRA) was conducted, without any external bias, to measure the photocurrent. Solar irradiance was provided by an ozone-free solar simulator system (Newport USA, calibrated using a standard photodiode) paired with an AM 1.5 global filter (Newport, USA). Electrochemical impedance spectroscopy (EIS) study was performed by applying an AC voltage of 10 mV to the cell in a frequency range from 10 mHz to 2 MHz. IPCE was recorded using a monochromator from Optometrics. The IPCE value was calculated using the following equation:

$$\mathrm{IPCE\%} = 1240 \cdot \mathrm{I} / \left(\lambda \cdot \mathrm{J_{light}}\right) \cdot 100 \quad \text{.....5.3}$$

where I (A/cm^2) is the measured photocurrent density at a specific wavelength λ (nm), and J_{light} (W/cm^2) is the measured irradiance using a photodetector (Newport, USA).

5.3 Results and Discussion

TiO_2 nanobelts have attracted particular attention against conventional nanospheres due to multiple advantages [118], including enhanced light scattering and absorption due to high length-to-diameter ratio, rapid electron transport in the longitudinal direction, and minimized charge recombination rate realized by reduced grain boundaries and less defects. In our companion study [115], we synthesized high-aspect-ratio TNBs using a stirring-assisted hydrothermal method. These TNBs were found to be 80-110 nm wide, ~10 nm thick, and up to 20 μm long. Particularly, aspect ratio of the TNBs is tailored by the stirring speed as demonstrated for its nanotube counterpart [116]. In this study, we further study the stirring effect and its vital implication to TNB length as well as photocatalytic activity, and explore the potential of TNBs as promising photocatalysts in an all-V PESC for efficient solar energy storage.

To further investigate the effect of stirring on nanostructure and morphology, TNBs were synthesized in a range of stirring speeds from 0 to 700 rpm. The stirring assisted hydrothermal reactor is illustrated in Figure 5-1 (a). The obtained samples are labeled as TNB-0, TNB-100, TNB-250, TNB-500, and TNB-700, where the numbers denote the applied stirring speed (in rpm) during the synthesis. As the SEM image in Figure 5-1 (b) shows, under no stirring, bundled spherical-shaped structures were formed in the TNB-0 sample. It is believed that the original Ti-O-Ti bonds in the starting material, i.e., anatase TiO_2 powder, have not yet been completely disrupted, and therefore anisotropic growth is delayed due to slow dissolution-recrystallization process at the static condition. In contrast, higher stirring speed entirely disentangled the TiO_2 bundles

and created structurally well-defined TNBs, as seen in Figures 5-1 (c) to 5-1 (f). In TNB-100, short (ca. 1 μm) nanobelts were obtained but with small random branches, while 700 rpm resulted in much longer (~16 μm) nanobelts (Figure 5-1 (f)). Besides, BET surface area analyses (Figure 5-2) of the synthesized TNBs suggest that the specific surface area (S_A, $m^2 \cdot g^{-1}$, shown in Figure 5-1 (g) and also tabulated in Table 5-1 continuously declines with increasing stirring speed. This, in conjunction with the averaged TNB lengths in Figure 5-1 (g), reveals that increase of stirring speed helps create more elongated TNBs, which, however, results in shrinkage of the specific surface area. In addition, powder XRD measurements were conducted to assess crystallographic information of all TNB samples. Figure 5-1 (h) shows that the characteristic anatase peaks, especially those corresponding to (101), (004) and (200) planes, become gradually intensified with increasing stirring speed, implying improved crystallinity.

Table 5-1 Specific surface area (S_A, measured from BET experiments), MB photodegradation rate constant, and specific degradation rate constant for different TNB samples.

Samples	TNB-0	TNB-100	TNB-250	TNB-500	TNB-700
S_A ($m^2\,g^{-1}$)	30.88	26.34	24.00	22.20	19.03
k (min^{-1})	0.59×10^{-2}	0.70×10^{-2}	0.79×10^{-2}	1.06×10^{-2}	1.07×10^{-2}
k' ($g\,m^{-2}\,min^{-1}$)	1.92×10^{-4}	2.65×10^{-4}	3.28×10^{-4}	4.76×10^{-4}	5.61×10^{-4}

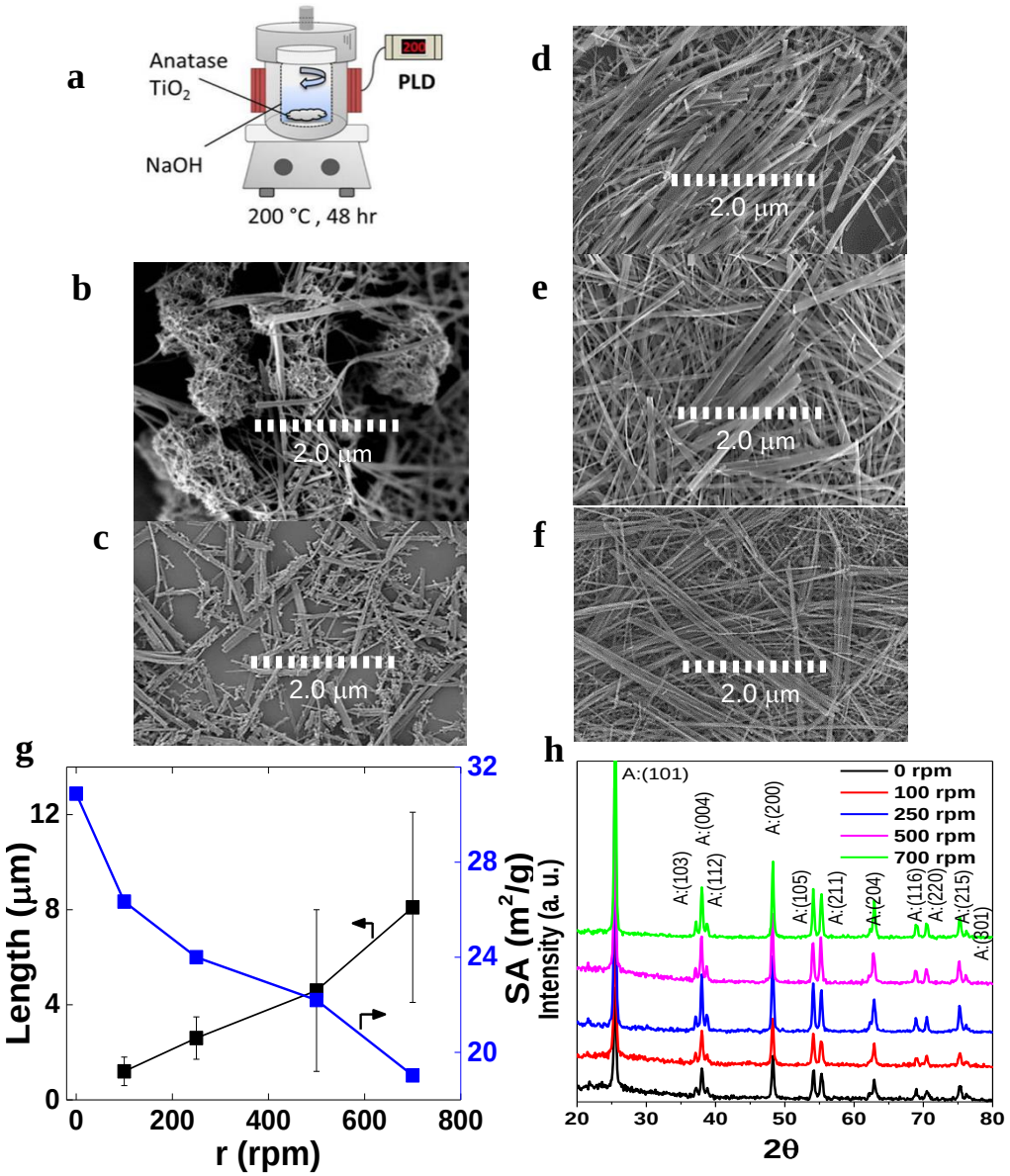

Figure 5-1 TNBs as a function of stirring speed during the hydrothermal synthesis. (a) Illustration of the stirring assisted hydrothermal method, (b) – (f) SEM images of TNB-0, TNB-100, TNB-250, TNB-500, and TNB-700, respectively. (g) Length (in μm) in the elongated direction and specific surface area (m^2/g) of TNBs synthesized at different stirring speeds. (h) XRD patterns of the synthesized TNBs. Letter A denotes anatase phase of TiO_2 (JCPDS # 21-1272).

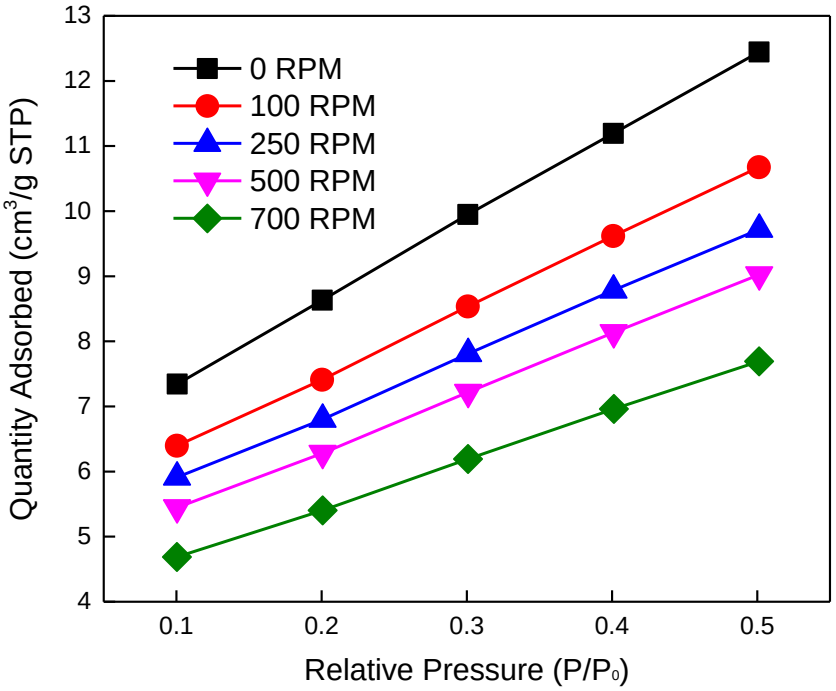

Figure 5-2 Brunauer–Emmett–Teller (BET) plots of the TNB samples synthesized at different stirring speeds in a stirring-assisted hydrothermal reactor.

To understand the role of mechanical stirring, we simulated growth of a 6μm long TNB with a 1st-order surface reaction (Figure 5-3). The parameters in the simulation was presented in Table 5-1. Formation of TNBs is assumed to be controlled by both diffusion-limited and surface reaction limited growth known as the DLSLOR model [119], which involves dissolution of solid TiO_2 precursor after breaking of original Ti-O-Ti bonds by highly concentrated NaOH, and subsequent transfer to the growth zone. We observed a monotonic decrease of surface reaction rate along the elongated direction of the TNB when the fluid flows parallel to the elongated direction of the TNB (Figure 5-4). Besides,

the front surface facing the fluid grows at a ~ 20% higher rate than the rear surface, in sharp contrast to the perpendicular case. Further study indicates that the TNBs grow at an even relatively higher rate from the front surface for the ones with higher aspect ratios, implying that the forced convective flow helps not only orientate but also grow elongated TNBs to the direction of fluid flow.

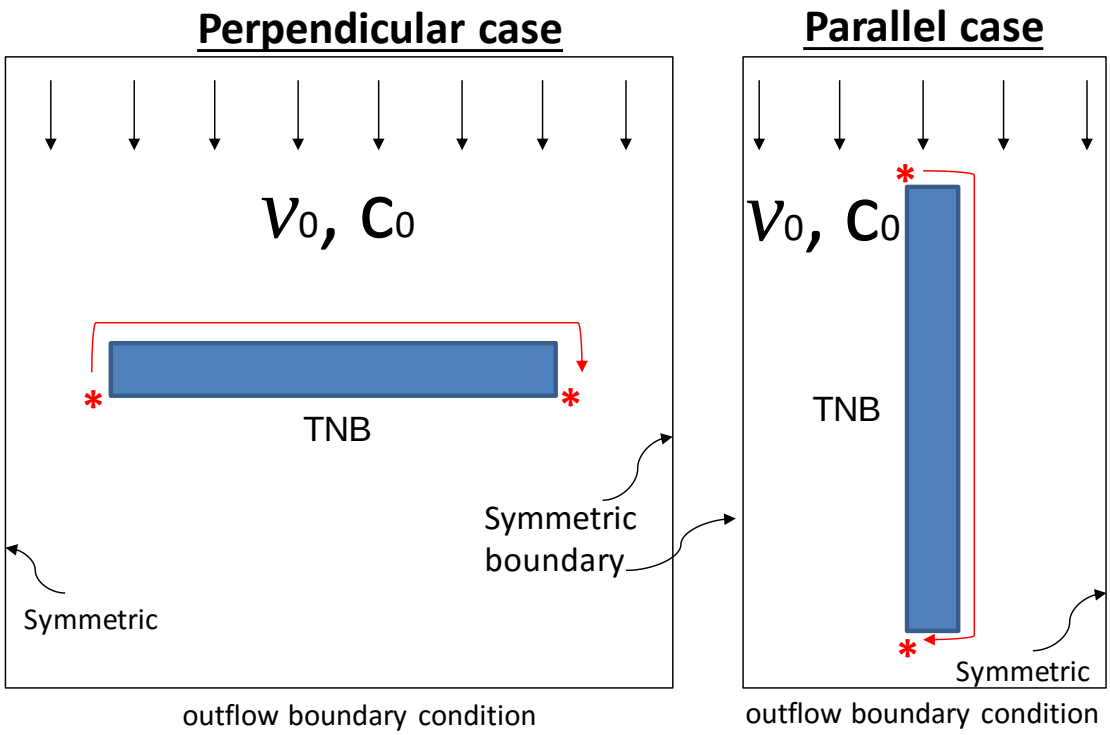

Figure 5-3 Computational domain and boundary conditions for both perpendicular and parallel cases. The TNB in both cases is 6μm long with an aspect ratio of 6:1. The direction along the surface of the TNB (an asterisk indicates either the starting or the ending point), where the simulated relative surface reaction rate is plotted in Figure 5-4, has been shown.

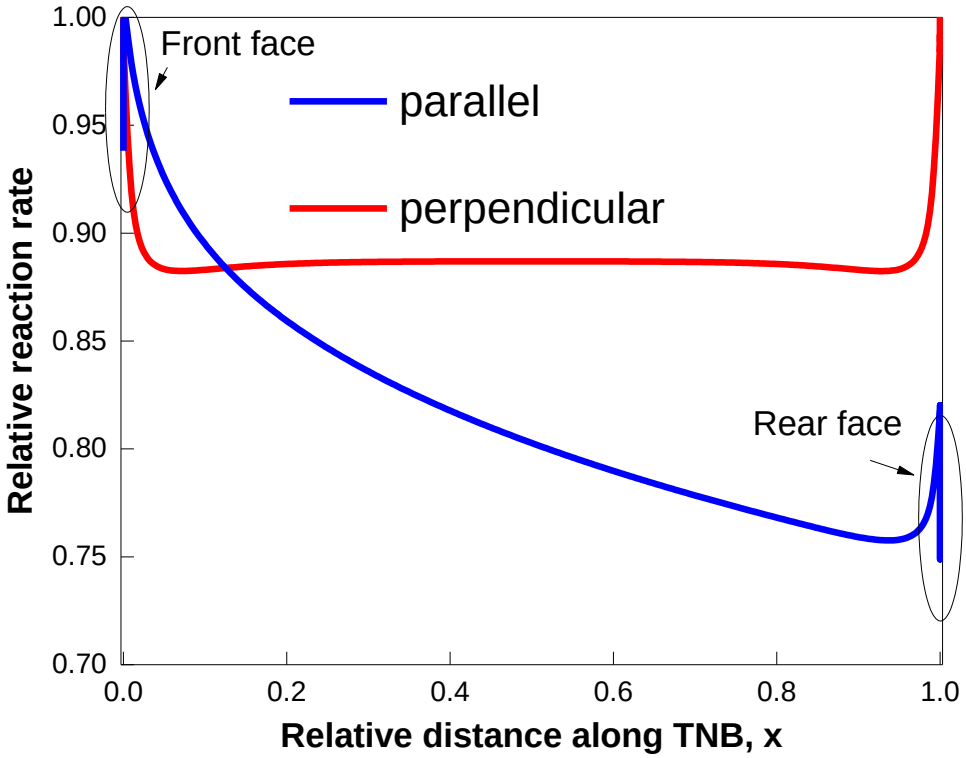

Figure 5-4 Simulated relative reaction rate along the surface of a TNB for two cases: parallel and perpendicular to the flow direction. Details of the simulation are provided in the text and Figure 5-3.

For further examination on microstructure of the TNBs, HRTEM images were taken on the TNB-700 sample. Figure 5-5 (a) shows the TEM image of a single nanobelt with a lattice spacing of 0.357 nm corresponding to the thermodynamically stable anatase (101) facets. This is consistent with our previous finding [115] and is further confirmed by the selected area electron diffraction (SAED) pattern (inset in Figure 5-5 (a)) that the main exposed plane is (101) and the growth direction is [010] (Figure 5-5 (b), denoted hereafter as Type I TNB). Additionally, considerable amounts of TNBs with a V-shape

terminus (Figure 5-5 (c)) are also observed and the opening angle of the V-shape terminus is determined to be 136.6° using a model anatase structure in Figure 5-6 created by Diamond 4.0.3. Further inspection with clear lattice fringes (inset of Figure 5-5 (c)) confirms that the V-shape terminus is formed between (011) and $(0\bar{1}0)$ planes (each with lattice spacing of 0.35 nm). According to the above analysis, the crystal structure is depicted in Figure 5-5 (d) (designated as type II TNB hereafter) with exposed (100) and (001) facets along the long axis and on the side surface of the TNBs, respectively, which are known to possess higher surface energy than (101). These exposed high-energy facets in the TNBs, i.e., (001) and (100), are more catalytically active [120, 121] than those in the thermodynamically stable geometry of nanosized TiO_2, which consists of ~ 94% of low-energy (101) facets [122].

Table 5-2 Parametric properties used in the simulation

Parameters	Value
Fluid density, ρ (kg/m^3)	950
Fluid viscosity, μ (kg·m^{-1}·s^{-1})	2.0 x 10^{-4}
Reaction rate constant (Eq. S4), k (m·s^{-1})	5.0 x 10^{-3}
Diffusion coefficient in fluid, (m^2/s)	3.0 x 10^{-9}
Inlet reactant concentration, C_0 (mole/l)	0.05
Inlet velocity, v_0 (m/s)	0.005

The exposed facets of the TNBs and their implication to photoactivity are further studied using Raman spectroscopy. Figure 5-7 reveals that all samples display similar characteristic peaks of anatase TiO_2 at 144 (E_g), 394 (B_{1g}), 514 (A_{1g}), and 636 cm^{-1} (E_g)

[123]. Here we adopted a semi-empirical approach [124] of using the intensity ratio between A_{1g} and E_g (144 cm^{-1}) to quantify the percentage of exposed (001) facets. The

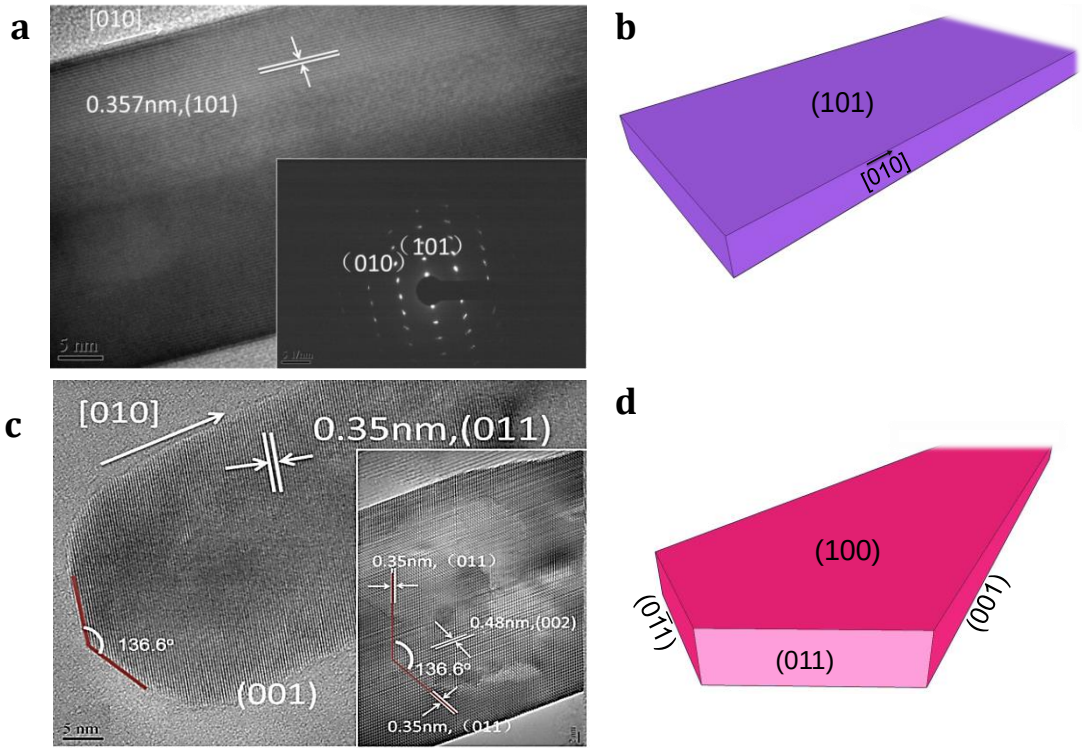

Figure 5-5 The TNBs synthesized at 700 rpm. (a) HRTEM image of a single type I TNB where the inset figure shows the SAED pattern taken along the [100] direction of the belt. (b) Crystal structure of Type I TNB. (c) Type II TNB with V-shape terminus and exposed (001) facets. The inset of (c) shows the crystalline orientation in the interior of the TNB. (d) Crystal structure of Type II TNB.

inset of Figure 5-7 shows a distinct trend that the percentage of exposed (001) facets in the TNBs increases monotonically with increased stirring speed in the hydrothermal synthesis, e.g., from 8.4 % at 0 rpm to 35.4 % at 700 rpm. According to reference [124], the surface structural difference between (001) and (101) facets may be the reason why the relative intensity changes in the Raman spectra when the stirring speed increases.

When the exposed (001) facets exist, the extent of symmetrical stretching vibration decreases, while the number of asymmetrical bending vibration (unsaturated 5c-Ti and 2c-O bonding modes, shown in Figure 5-6) increases, therefore leading to an increased relative intensity ratio between A_{1g} and E_g modes. Since there is no experimental condition change except for the stirring speed, the results undoubtedly prove that increasing stirring speed during the hydrothermal synthesis created higher fractions of exposed (001) facets (estimated to be 4.2 times more from 0 to 700 rpm), which resides primarily in type II TNBs. This simple yet effective *additive-free* process thus surpasses traditional facet-controlling strategies that rely on capping agents, as mentioned earlier, such as HF [112] or surfactant [113], which have to be removed in a tedious high-temperature process.

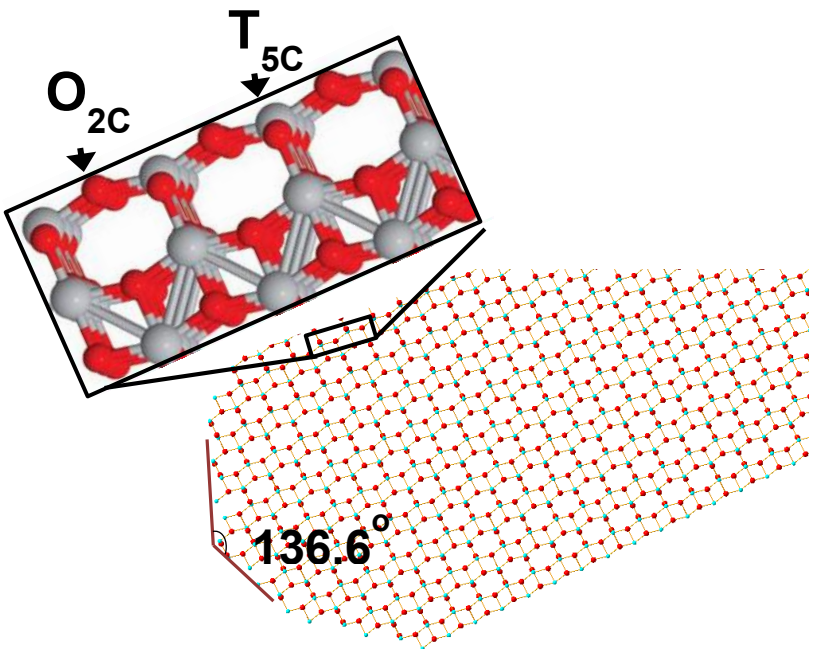

Figure 5-6 A model anatase structure showing the V-shape terminal and the unsaturated 5c-Ti and 2c-O bonding modes on the (001) plane along the side surface of type II TNBs.

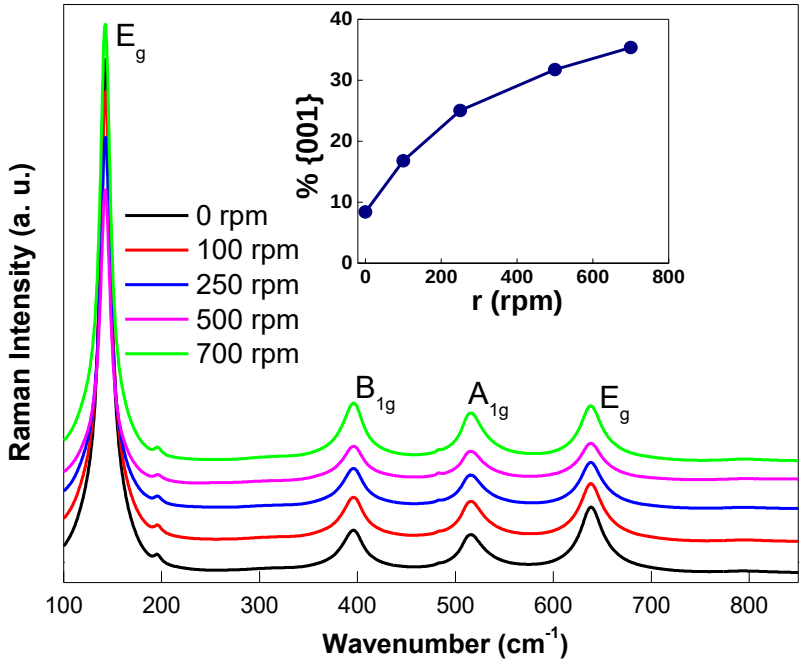

Figure 5-7 Raman spectra of TNBs synthesized at different stirring speeds. The inset shows percentage of exposed {001} facets calculated from relative intensity ratio between A_{1g} mode at 514 cm^{-1} and E_g mode at 144 cm^{-1}, as a function of the stirring speed.

Mindful of the discovered relationship between stirring speed and exposed crystal facets, we performed MB photodegradation test using the TNBs under 360 nm irradiation to evaluate their photoactivity. In Figure 5-8 (a), the TNBs synthesized at higher stirring speeds, especially at 700 rpm, display enhanced photocatalytic activity, as evidenced by faster reduction of MB concentration under illumination (e.g., 52% drop of MB concentration for TNB-700 in 30 min). The effect of the band structural change on the photocatalytic activity was insignificant as there is no apparent change in light absorption (UV-vis spectra in Figure 5-9). On the other hand, the enhanced specific photoactivity (Table 5-1) can be ascribed to more exposed highly-active (001)/(100) facets and

enhanced electron mobility. Similar results were reported by Roy et al [114] for cuboid TiO_2 single crystals but with relatively smaller surface area.

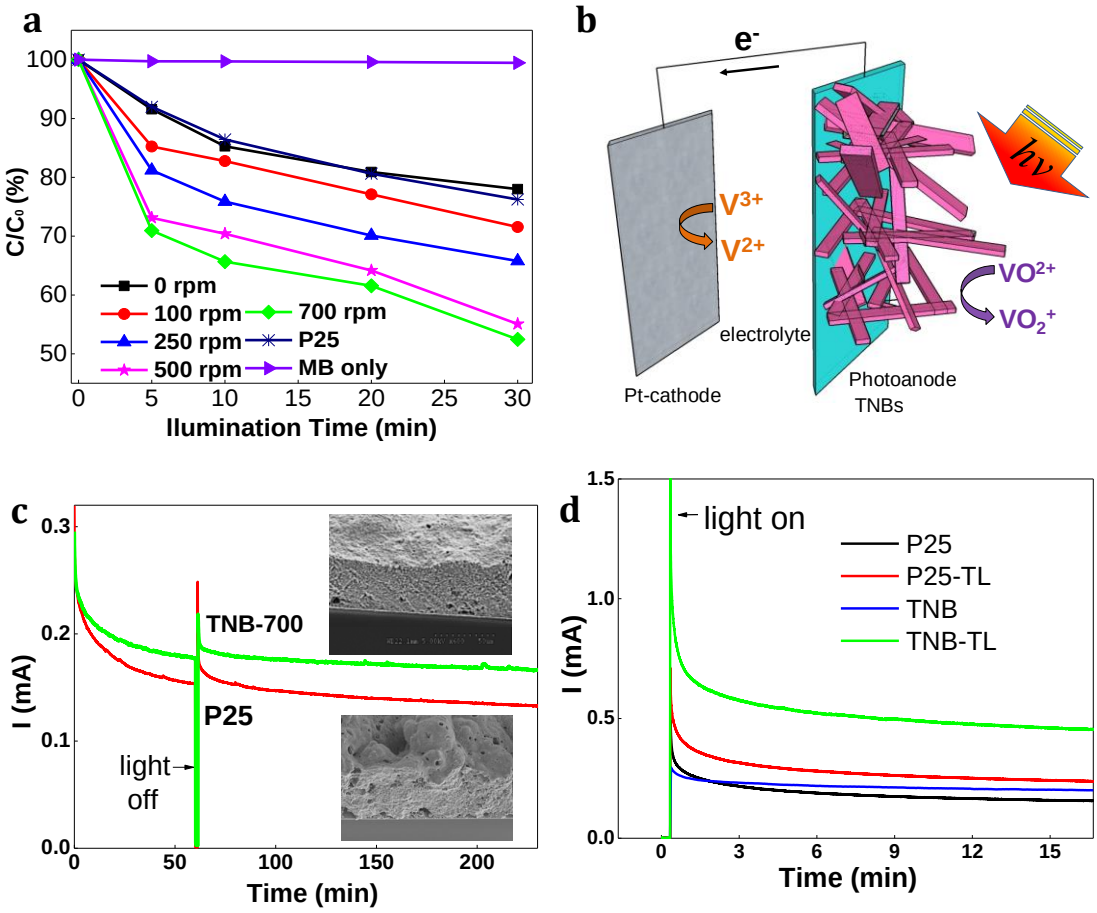

Figure 5-8 Photoelectrochemical characterization. (a) Photodegradation curves of MB under UV light for different TiO_2 samples. (b) Schematic illustration of an all-V PESC. Two different vanadium redox electrolytes, i.e., 0.01 M VO^{2+} and 0.01 M V^{3+} (balanced with 3 M H_2SO_4 and separated by a Nafion 117 membrane) were used as the anolyte (in contact with the photoanode) and catholyte (in contact with a Pt mesh), respectively. Electrode reactions at the photoanode and Pt cathode follow: $VO^{2+} + H_2O \rightarrow VO_2^+ + e^- + 2H^+$ and $V^{3+} + e^- \rightarrow V^{2+}$, respectively. (c) Photocurrents in an all-V PESC using TNBs and

P25 TiO_2. (d) Photocurrents in an all-V PESC using photoelectrodes with and without $TiCl_4$ pretreatment.

To further access the performance of TNBs in our newly-developed all-V PESC, we examined TNB-700 and P25 as photocatalysts in a cell setup schematically illustrated in Figure 5-8 (b). The initial photocurrent (Figure 5-8 (c)) of the TNB-700 electrode under AM1.5 illumination is almost identical to that of P25, in sharp contrast to the MB photodegradation results, but with less deterioration—after 4 h it remains 50 mA higher than that of P25. Furthermore, stable operation for TNB-700 could be quickly established after light was temporally switched off for 1 min at 60 min compared to that using P25 TiO_2. It is important to note here that no external bias was applied to the cell; therefore, the observed photocurrents are generated solely from the AM1.5 illumination.

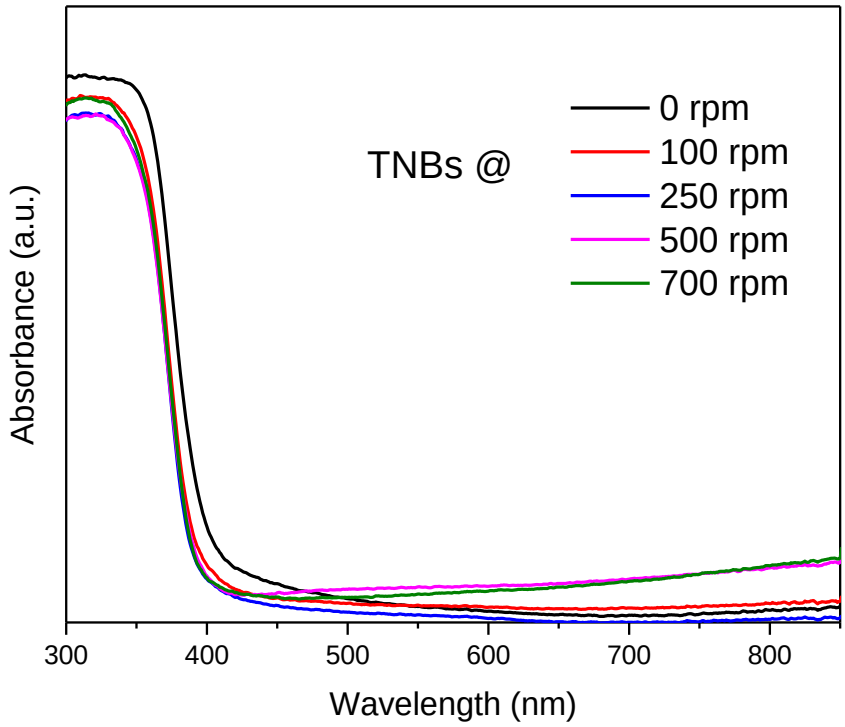

Figure 5-9 UV-vis spectra of the TNBs synthesized at different stirring speeds.

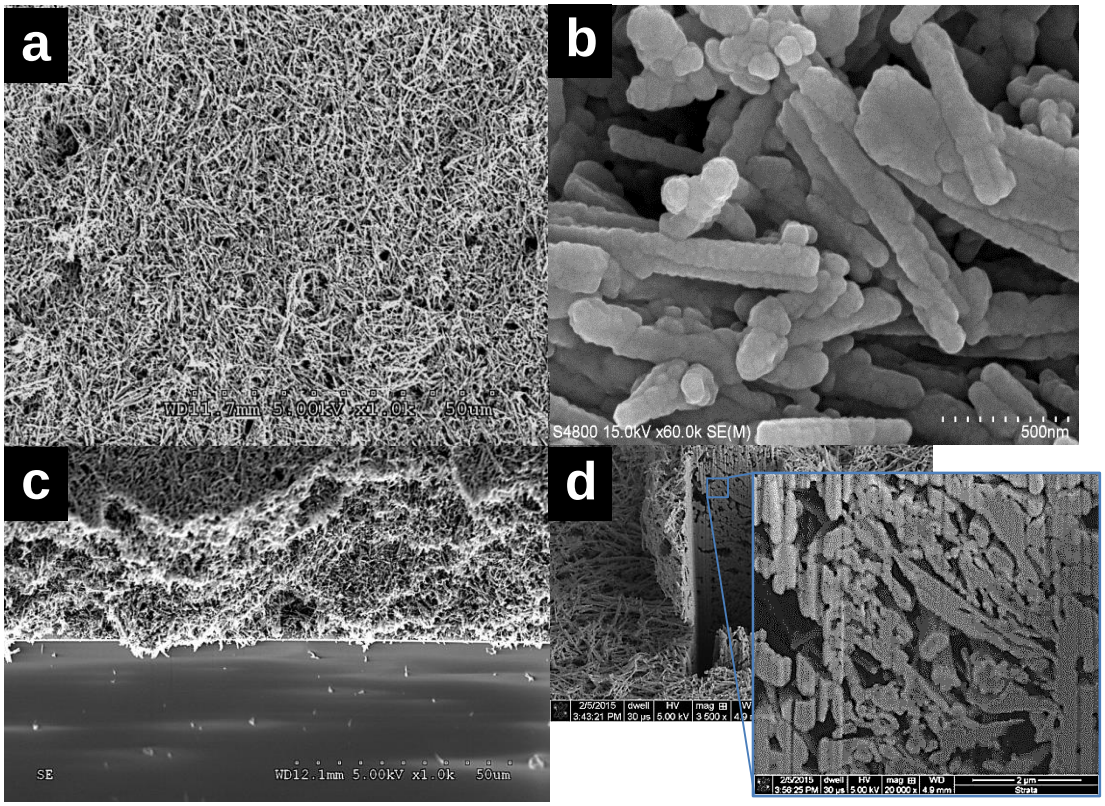

Figure 5-10 Electron microscopic images of the TNB-TL electrode: (a) low-magnification top-view SEM image, (b) high-magnification top-view SEM image, (c) cross-sectional SEM image, and (d) Microscopic images where Focused Ion Beam (FIB) was used to reveal interior of the electrode.

As for the faster decay of photocurrent observed in the P25-based cell, photocatalyst degradation due to either chemical or photoelectrochemical corrosion can be ruled out as no evident change in the surface chemistry of both electrodes before and after the test was found. In fact, the inserted SEM images in Figure 5-8 (c) give clues as to the relationship between electrode microstructure and the photocurrent. The electrode with P25 appears very dense though some discrete voids are sparsely spotted. The TNB-700 electrode, however, appears uniformly porous through the entire thickness of the electrode, and therefore may facilitate transport of vanadium redox species (i.e., VO^{2+}). Indeed, based on TiO_2 loading and the electrode thickness, calculated porosity values for two electrodes are 0.86 (TNB) and 0.66 (P25), respectively, which could account for a 1.7-fold improvement in effective diffusion coefficient of VO^{2+}, estimated via the Bruggman correlation [125], for the TNB-700 photoelectrode.

In addition, we employed $TiCl_4$ pre-treatment to the TNB-based photoelectrode in an attempt to possibly enhance the bonding and therefore charge transport between TNBs. The photoelectrode is denoted as TNB-TL hereafter. Both SEM and UV-vis spectroscopy were used to gain further insight into the structural/morphological and

optical properties of the TNB-TL electrode**.** Figures 5-10 (a) and (c) indicate that the TNB-TL still maintains its porous structure but with a well-connected 3D network. Both high-magnification top-view SEM image (Figure 5-10 (b)) and microscopic images (Figure 5-10 (b))**,** where a focused ion beam was used to reveal interior of the electrode) show that a thin layer of TiO_2 (from $TiCl_4$) film possibly form uniformly on the surface of TNBs. Further inspection using UV-vis spectroscopy (Figure 5-11) and more specifically from the red-shift of the absorption edge after $TiCl_4$ treatment, allows us to speculate that this TiO_2 thin layer formed from $TiCl_4$ might be composed of rutile phase because of its narrower bandgap (3.03 eV).

To assess performance of TNBs in the all-V PESC, we conducted two sets of photocharging experiments (Figure 5-8 (c)) using $TiCl_4$-treated (designated as P25-TL) and untreated P25, as well as treated (TNB-TL) and untreated TNBs. During the initial 1 min when the cells were kept in dark, no photocurrent was observed. Upon illumination, the photocurrents spike initially and then gradually level off. The $TiCl_4$ treatment to P25 only slightly improves the photocurrent (stabilized between 6 and 17 min) from 0.16 mA to 0.23 mA. In comparison, the TNB, after $TiCl_4$ treatment (i.e., TNB-TL), achieves a stabilized photocurrent double that of P25-TL, representing a 2.3-fold increase in photocurrent. This significant photocurrent enhancement for the TNB samples is attributed to improved charge transfer through a 3-D network of semiconductor due to $TiCl_4$ treatment, fast kinetics of the vanadium redox, and intrinsic properties of high-aspect ratio TNBs, including high crystallinity (Figure 5-1 (g)), high surface specific activity (Table 5-1), 1-D elongation of the belts, long electron diffusion length, and almost two-fold higher effective donor concentration comparing to nanoparticles. Particularly, anatase TiO_2 nanobelts have been demonstrated to have electrical conductivity of about $10^{-7}\ \Omega^{-1}\ cm^{-1}$, 100 times higher than that the nanoparticle counterpart [126].

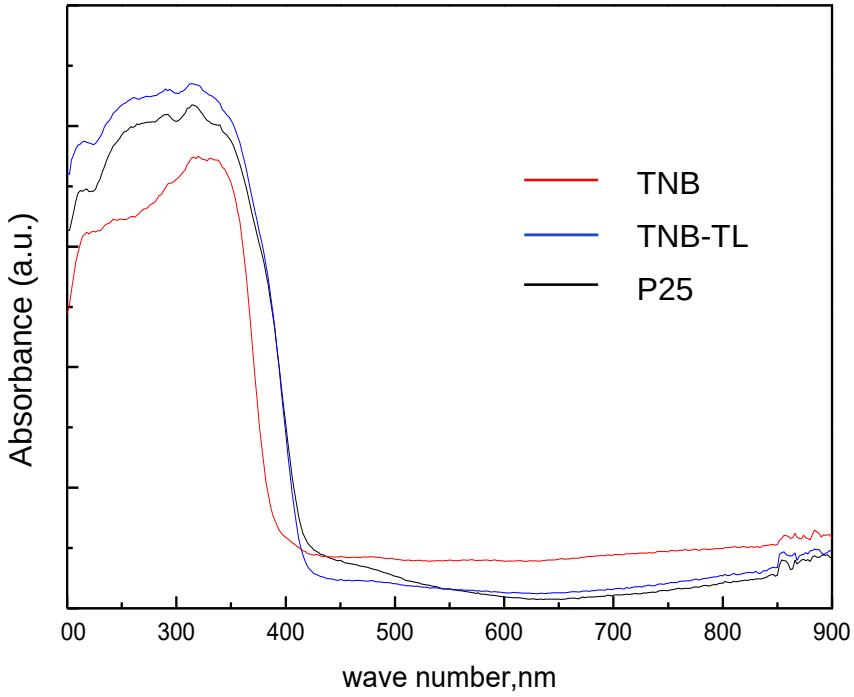

Figure 5-11 UV-Vis spectra of TNB-700, TNB-TL, and P25.

To shed light on the implication of $TiCl_4$ pre-treatment to enhanced photocatalytic activity in the TNB-TL based photoelectrode, we conducted EIS measurements at open circuit in the all-V PESC. In Figure 5-12, Nyquist plots of both TNB and TNB-TL electrodes were composed of similar arcs/partial arcs. The small arc and an even bigger arc (only a portion) at low frequency, according to references [127, 128], correspond to electron transport resistance and interfacial capacitance at the Pt/electrolyte and TiO_2/electrolyte interfaces, respectively. Upon illumination, diameter of the high-frequency arc for the TNB electrode shrinks considerably indicating that charge transfer resistance at the Pt/electrolyte interface was reduced. And the low frequency arc corresponding to charge transfer at the TiO_2/electrolyte interface was also reduced under

illumination, indicated reduced charge transfer resistance. On the other hand, smaller diameter of the high frequency arc for the TNB-TL electrode, which was only one quarter of that of the bare TNB electrode, remains almost unchanged upon light illumination, suggesting enhanced charges injection into Pt/electrolyte interface enabled by the $TiCl_4$-treated TNB photoanode. Moreover, the lower frequency arc for TNB-TL smaller than bare TNB regardless of illumination or dark condition, indicate that the charge transfer resistance and interfacial capacitance at TiO_2/vanadium (IV) interface was reduced by the $TiCl_4$ treatment.

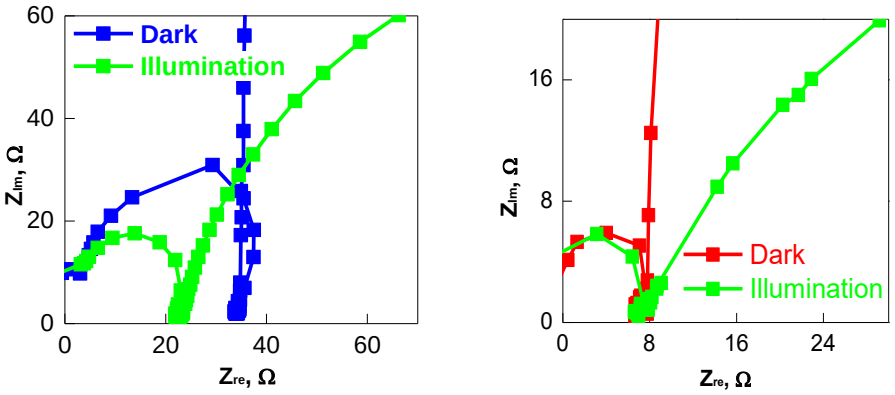

Figure 5-12**.** EIS spectra in Nyquist plots obtained from all-V PESCs using (a) TNB-700 and (b) TNB-TL as the photoelectrode.

IPCE measurements were also conducted to assess the overall photocharging efficiency of the all-V PESC using TNB-TL as the photoanode. The results were benchmarked against P25 which has been extensively used as a reference in our previous efforts [92, 104-107, 117] and treated with $TiCL_4$ in this study (P25-TL). In Figure 5-13, the IPCE remains almost zero at wavelength above 450 nm owing to the wide bandgap of TiO_2. In the range from 350 to 400 nm, the IPCE increases with

decreasing wavelength of the irradiating light. At 350 nm the IPCE of the cell with TNB-TL reaches a maximum (~22 %), double that of commercial P25-TL (~11 %). This is strongly indicative of three efficient processes in the TNB-TL based cell: light harvesting (LH), charge separation (CS), and charge collection (CC), which correspond, respectively, to three process efficiencies, i.e., η_{LH}, η_{CS}, and η_{CC}, since the IPCE can be expressed in the following equation:

$$\mathrm{IPCE} = \eta_{\mathrm{LH}} \cdot \eta_{\mathrm{CS}} \cdot \eta_{\mathrm{CC}}. \quad \text{.....5.4}$$

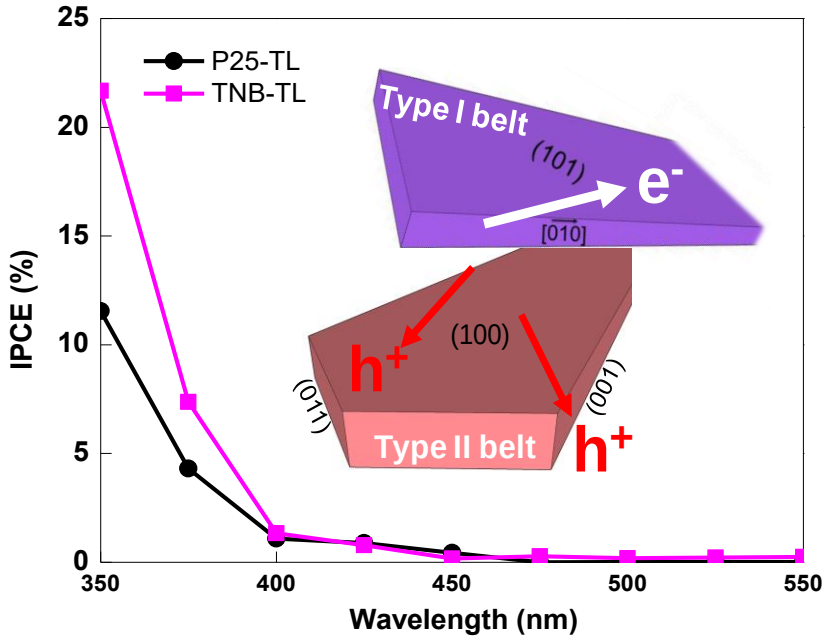

Figure 5-13. IPCE spectra of all-V PESC assembled using TNB-TL as the photoelectrode, collected at the incident wavelength range from 350 to 550 nm, in comparison to P25.

Because of comparable light absorbing characteristics (Figure 5-11) of the TNB-TL and P25 electrodes, the enhancement of IPCE for the former may solely originate from the following three factors, as illustrated in the inserted schematic in Figure 5-13. First, the more exposed high-energy (001)/(100) (in type II TNB) TiO_2 facets, as the

reaction sites for photoelectrochemical oxidation of VO^{2+}, could yield high η_{LH}. Second, the longitudinal dimension of the highly crystalline TNB-TL improves electron diffusion with depressed scattering at particle-particle interfaces. It also provides a large scale in the elongated direction to minimize electron-hole recombination. As a result, both η_{CS} and η_{CC} improve. Third, the largely populated low-energy (101) facets (in type I TNB) and high-energy (001) facets (in type II TNB) could preferentially collect electrons and holes, respectively, according to Ref. [114], therefore further enhancing e^-/h^+ separation. Most important, the above phenomena benefit from $TiCl_4$ pre-treatment that essentially bonds the geometry-enhanced ultra-long TiO_2 nanobelts. Fast charge transport is enabled within the established interconnected network of TNBs, which were found to be laid down along the in-plane direction of the photoelectrode in Figure 5-14 (therefore poor adhesion between TNBs). Research is currently underway to align the TNBs along the through-plane direction of the photoelectrode to fully assess their fast electron diffusion in the longitudinal dimension.

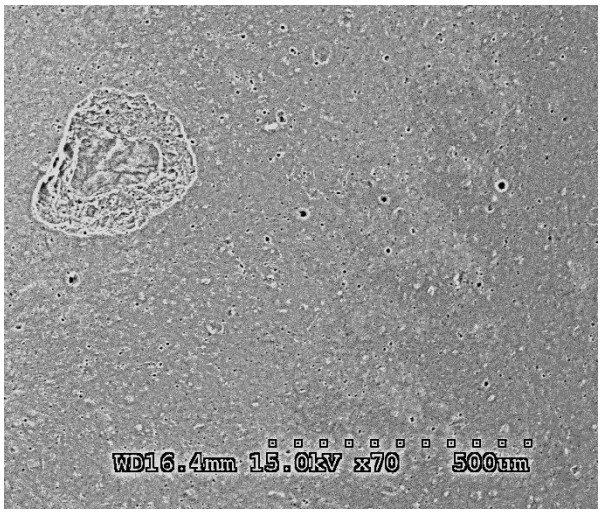

Figure 5-14 SEM image of a TNB-based photoelectrode showing a crater caused by partial delamination. The inserted high-resolution image shows that the elongated TNBs are laid down along the in-plane direction of the photoelectrode.

5.4 Conclusion

In conclusion, we have built on our companion studies and demonstrated in this study [92, 104-107, 115, 117], a facile stirring-assisted hydrothermal method to prepare geometry-enhanced TNBs for highly efficient all-vanadium photoelectrochemical storage cells. We have presented evidence that increasing the stirring speed in the hydrothermal synthesis from 0 to 700 rpm creates 4.2 times more exposed high-energy (001) facets. The all-V PESC demonstrated a peak IPCE of ~22% without any external bias, double that of commercial P25 TiO_2 (~11%) benchmark. The enhanced photocatalytic performance is largely attributed to (i) the improved charge separation efficiency because of the enhanced geometry of TNBs, (ii) more exposed high-energy (001)/(100) facets, and (iii) facilitated charge transfer enabled by high electron mobility. The capability of enhancing semiconductor geometry using mechanical stirring during synthesis could open up exciting new avenues for design and fabrication of future functional materials in various areas, such as PEC water splitting, dye sensitized solar cells, photocatalysis, and particularly in the all-V PESC.

Chapter 6

An All-vanadium Continuous-flow Photoelectrochemical Cell for Extending State-of-charge in Solar Energy Storage

6.1 Introduction

In this chapter, we have developed an all-vanadium (all-V) photoelectrochemical storage cell (PESC) and demonstrated a high Faradaic efficiency of 95% [129] and peak incident-photon-to-current efficiency (IPCE) of 45% in solar energy storage [117]; however, the photocharging depth and photocurrent are yet to be improved. Here, an all-V continuous-flow PESC was developed to address the shallow charge depth problem and improve the photoresponse. It was discovered that forced convective flow of electrolytes during photoelectrochemical conversion greatly enhanced the photocurrent by 5 times comparing to the case with static electrolytes. Electrochemical impedance spectroscopy (EIS) study indicated that the charge transfer resistance was greatly reduced with forced flow of electrolytes through the cell as a result of better mass transport at the U-turns of the tortuous serpentine flow channel of the cell. Our results also reveal that variation of flow rate, when beyond a certain minimum threshold, didn't have a significant impact on the photocurrent. Taking advantage of the improved photocurrent and diminished charge transfer resistance, the all-V continuous PESC was capable of producing ~20% change in state of charge (SOC) without using any external bias. The change of SOC during 1.7 h was more three times higher than the cell with static electrolytes during 25 h.

6.2 Experimental

6.2.1 Fabrication of photoelectrodes

0.5 g Degussa P25 (Evonik) TiO_2 nanoparticles was mixed with 2.15 g α-terpineol (Fisher Scientific, USA), and then sonicated for 20 min. Fluorine-doped tin oxide

(FTO) glass substrates (2 in × 2 in) were prepared and cleaned by sonication in acetone (99.7%, Fisher Scientific, USA) for 20 min followed by methanol (99.8%, Fisher Scientific, USA) for 20 min, and then DI water. The obtained slurries were coated on the FTO glass substrates using a doctor blade to form a uniform film (1 in ×1 in) and then dried in an oven at 80^{o}C for 2 h. The as-prepared photoanodes were sintered with air flow in a tube furnace at 500^{o}C for 1 h. [104, 106, 117, 129, 130]

6.2.2 Assembly of the all-V continuous-flow PEC cell

Schematic diagrams of the all-V continuous-flow PESC, experimental setup, and detailed cell (active area of 1 in ×1 in) construction are presented in Figure 6-1. A Nafion 117 membrane was used to separate two different vanadium electrolytes, i.e., 0.01 M VO^{2+} and 0.01 M V^{3+} (balanced with 3 M H_2SO_4) in the anode and cathode compartments, respectively. Two acrylic (Virtualplast, Israel) flow fields, machined by an Epilog Helix 24 laser cutter, were attached to both side of the Nafion 117 membrane. The depth and width of the flow channel are 1 mm and 1mm, respectively. The photoanode was placed at the anode compartment, while a carbon paper (SGL, AA30) serving as the counter electrode was inserted between the cathode flow field and current collector (endplate). Carbonaceous materials have been demonstrated to be superior to Pt in VRBs[131] partially because of depressed hydrogen evolution as a side-reaction. The layers of the cell were glued together to prevent leaking.

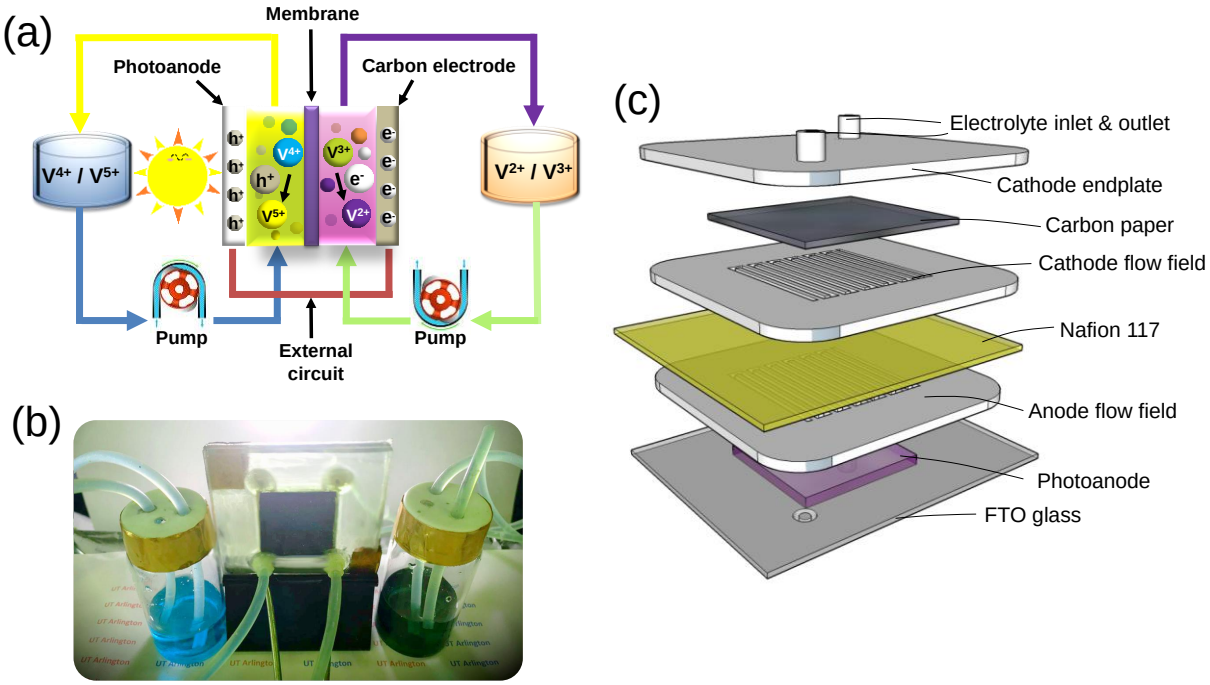

Figure 6-1 (a) Schematic representation of the all-V continuous-flow PESC. (b) Experimental setup for photoelectrochemical study of solar energy storage. The assembled cell, silicon tubes, and both the catholyte and anolyte tanks are shown. (c) Exploded view of the components in the all-V continuous-flow PESC. The depth and width of the flow channel are 1 mm and 1mm, respectively.

6.2.3 PEC studies and characterization of the all-V continuous-flow PESC

The PEC characteristics of the all-V continuous-flow PESC were studied using a PARSTAT 2273 potentiostat. During operation of the cell, the VO^{2+} anolyte and V^{3+} catholyte were continuously pumped to the cell (Figure 6-1 (a)), where the photoanode and the carbon paper served as the working electrode (WE) and counter electrode, respectively. The photocurrent was measured using the protocol of zero-resistance ammetry (ZRA) with no externally applied bias. Solar irradiance was provided by an ozone-free solar simulator system (Newport, USA) paired with an AM 1.5 global filter

(Newport, USA). Electrochemical impedance spectroscopy (EIS) study was performed by applying an AC voltage of 10 mV to the cell in a frequency range from 10 mHz to 2 MHz.

The faradaic efficiency (η_F) is calculated by the equation:

$$\eta_F = \frac{F\Delta n}{\Delta Q} \text{.....6.1}$$

where Δn is the amount of reacted vanadium redox species during the test, F is the Faraday constant (96 485 C mol^{-1}), and ΔQ is the generated charge. The overall solar-chemical-electricity conversion efficiency could be calculated according to

$$\eta_{overall} = \frac{\eta_{dis} \times I_{ph} \times E^0}{P_{in}} \text{.....6.2}$$

where I_{ph} is the photocurrent, E^0 is the reversible potential of the redox couple (1.25 V), P_{in} is the incident solar power, and η_{dis} is the discharge efficiency. η_{dis} is estimated at 90%.

To determine the concentration of the vanadium redox species during operation, a small amount of electrolyte was extracted and analyzed in a quartz cuvette by a UV-vis spectrophotometer (PerkinElmer Lambda 35). A linear relationship between the peak (765 nm) absorbance (A) of vanadium redox and its concentration is assumed, according to the Beer–Lambert law, i.e.,

$$A = \varepsilon lc \text{.....6.3}$$

where ε is the molar absorptivity, l is the path length of the cuvette, and c is the concentration of the targeted vanadium redox.

6.2.4 Computational studies

In order to theoretically study the influence of electrolyte flow rate on photoresponse of the continuous-flow PESC, simulation was conducted by the SIMPLER algorithm in a commercial CFD software Fluent 6.3.26. User defined functions (UDF) were written to account for the diffusivity and source terms of different species including

vanadium redox ions, electrons, and holes. Details of the computational models are included in the Appendix 1.

6.3 Results and discussion

6.3.1Effect of vanadium redox flow on PEC response

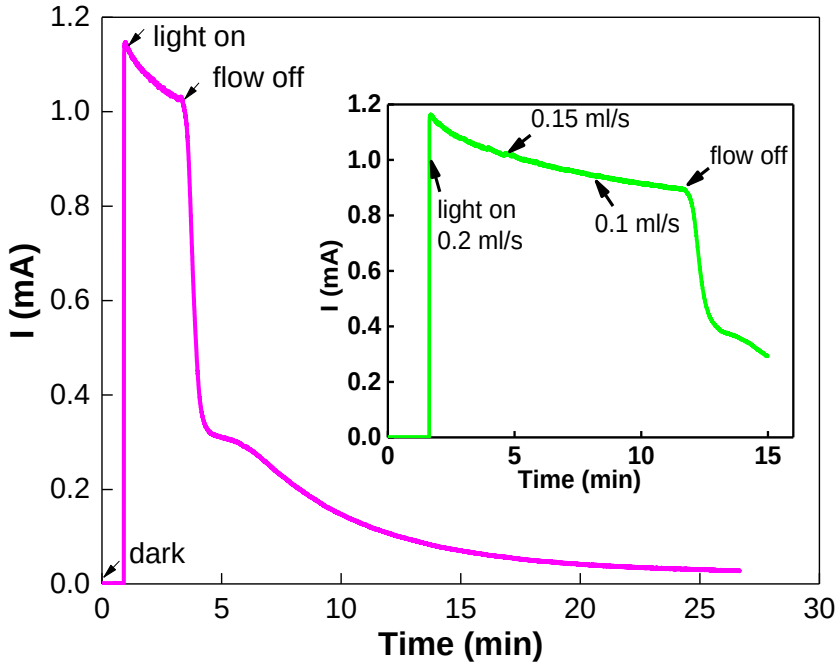

Figure 6-2 Photoelectrochemical response of the all-V continuous PESC to flow for 0.01 M all vanadium electrolytes. A TiO_2 electrode was employed together with vanadium electrolyte at 0.01 M. The flow rates of the anolyte and catholyte were changed simultaneously.

Fig 6-2 presents the impact of electrolyte flow rate on photocurrent produced from the all-V continuous-flow PESC. Two sets of experiments were conducted. In the 1st set of test, when both of the anolyte and catholyte were fed into the cell at flow rate of 0.2 ml/s, upon illumination at 60 s the photocurrent promptly jumped to 1.15 mA appearing as

the anodic overshoot (AO) [132] that is related to the surface trap states on the photocatalysts. After 3 min, complete shutting off the flow caused the photocurrent quickly drop to 0.33 mA followed by a gradual decay to 0.03 mA at 25 min when the vanadium species in the flow fields are depleted. It is evident that the forced convective flow of electrolytes plays a critical role here in the PEC conversion, resulting in a 5-fold improvement in photocurrent. Note that the all-V continuous-flow PESC is essentially a photocharged vanadium redox flow battery (RFB), which could take full advantage of fast PEC kinetics of vanadium redox under convective flow.

In the 2nd set of experiment (inset of Figure 6-2), after the light was switched on the photocurrent promptly appeared as a spike (as a result of AO), which resembles the result in the 1st set of experiment, then gradually leveled off. The initial electrolyte flow rate was 0.2 ml/s, and then reduced to 0.15 ml/s and 0.1 ml/s at 5 min and 8 min, respectively. The PEC performance of the cell, although largely affected by the forced convective flow as seen in the 1st set of test, was imperceptibly impacted by changing flow rate from 0.2 to 0.1 ml/s. Actually, current density and electrolyte flow rate are two crucial factors in RFB. According to the study [133] in VRBs, the limiting current density continuously increases with the flow rate as a result of enhanced mass transport. In our case, the cell photocurrent is determined by a complex interplay of multiple factors, including PEC process at the photoanode surface, photocatalyst and solid/electrolyte junction, electrochemical reaction at the cathode, and mass transport. Our results seem to indicate that forced convective flow of electrolytes helps shift the limiting factor in the overall cell performance from mass transport, particularly at the electrode/electrolyte interfaces, for stagnant electrolytes to photo/electrochemical reactions when a certain threshold of electrolyte flow rate is achieved.

In contrast to our previous studies [104, 129] with similar vanadium redox and photocatalysts but static electrolytes, the observed photocurrents in Figure 6-1 are more than 5 times higher. This exceptional enhancement is largely attributed to the fast reaction kinetics of vanadium species that quickly scavenge the photogenerated charges with minimized recombination: holes tend to react with the VO^{2+} in the anolyte in the photoanode while electrons reduce V^{3+} in the catholyte. Most important, introduction of forced flow in the all-V PESC is believed to not only reduce mass transport polarization [134], but also expedite the abovementioned surface processes. It is known that electron-hole recombination consumes a large fraction of the photogenerated charge carriers in a much shorter time scale [135, 136] for wide-bandgap semiconductors such as TiO_2 [137]. Typically, under illumination photogenerated charges could be trapped by the surface states of TiO_2, and the induced recombination is responsible for the rapid decrease of photocurrent after light is turned on [138]. Especially, when reactive species near the photoanode surface have been depleted by PEC reactions, charges accumulate and saturate at the TiO_2 surface. This phenomenon is supposed to be largely eliminated by the continuous flow cell design, since the exhausted vanadium redox could be effectively replenished. In addition, a carbon paper, instead of a Pt electrode in our previous studies, was utilized as the counter electrode (cathode). Carbonaceous materials have been demonstrated superior to Pt in VRBs [131] partially because of depressed hydrogen evolution as a side-reaction.

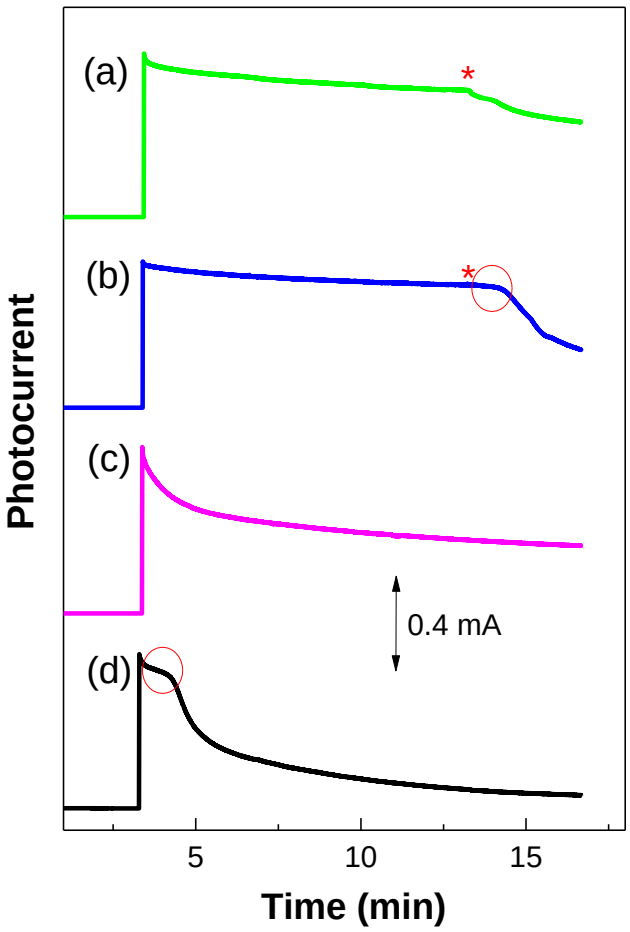

Figure 6-3 Photoelectrochemical response of the all-V continuous-flow PESC to various flow conditions using 0.01 M vanadium redox electrolytes. Both the anode and cathode flow (at 0.2 ml/s) was on at the beginning, and light was turned on at 3 min. (a) At 13 min the anode flow was switched off. (b) At 13 min the cathode flow was switched off. (c) Anode flow was turned off at 3 min. (d) Cathode flow was turned off at 3 min.

To further investigate the impact of flow on cell performance, different flow conditions were adopted at the photoanode and cathode. In Figure 6-3, after light was switched on at 3 min, in both Figure 6-3 (a) and (b) constant flow rates of vanadium electrolytes at 0.2 ml/s were applied for both the photoanode and cathode, which

produced fairly stable photocurrents. At 13 min either the anode flow (Figure 6-3 (a)) or cathode flow (Figure 6-3 (b)) was shut off while the other side remained unchanged. Apparent decrease of photocurrent was observed for both cases, indicating that mass transport in the anolyte and catholyte both plays an important role in the overall PEC reactions. However, careful examination of the curves suggests drastically different transient behavior of photoresponse for the two cases. Upon shutting off the anode flow, the photocurrent immediately dropped (Figure 6-3 (a)), gradually approaching an equilibrated value. In contrast, turning the cathode flow off resulted in a 60 s photocurrent shoulder (denoted by a red circle in Figure 6-3 (b)) followed by a more abrupt decay than the previous case.

To confirm the above results and further study the impact of electrolyte flow rate on cell photoresponse, asymmetric flow conditions with flow only on one side of the cell were adopted: 0 and 0.2 ml/s of electrolytes at the anode and cathode, respectively, in Figure 6-3 (c); and 0.2 and 0 ml/s of electrolytes at the anode and cathode, respectively, in Figure 6-3 (d) Comparison of the two cases, once again, clearly suggests a more important role of cathode flow on the cell photoresponse. Interestingly, a similar 60 s photocurrent shoulder (denoted by a red circle in Figure 6-3 (d)) emerged after turning on the light, clearly resembling that in Figure 6-3 (b). The observed shoulders in both cases actually represent a two-stage decay of photocurrent, which is closely related to the mass transport process of vanadium redox species in the cathode flow field.

These findings corroborate the observation in VRBs that the anolyte and catholyte flow rate impacts on cell performance differently[133]. In our all-V continuous-flow PESC, the observed shoulders in both Figure 6-3 (b) and Figure 6-3 (d) actually represent a two-stage decay of photocurrent, which is closely related to the mass transport process of vanadium redox species in the cathode flow field. Though the root

cause of the abovementioned observation remains ambiguous and requires a profound investigation to clarify the impact of flow rates on cell performance,[139-141] several reasons are possible. First of all, diffusivity of V^{3+} is relatively smaller than that of VO^{2+}.[134] Under stagnant catholyte, slow diffusive transport of V^{3+} to the counter electrode (carbon paper), after being partially depleted by the photogenerated electrons, could cause an abrupt drop of photocurrent. Second, overpotential at the cathode as the driving force for V^{3+} reduction is small. As discussed in our previous study,[129] the overpotential for the cathode reaction is only 0.24 V compared to 1.8 V at the photoanode under standard conditions. Albeit exhibiting excellent electrochemical kinetics, the V^{3+} reduction reaction is expected to be more dependent on vanadium redox concentration and requires convective flow to replenish V^{3+} supply.

6.3.2 Electrochemical impedance spectroscopy study

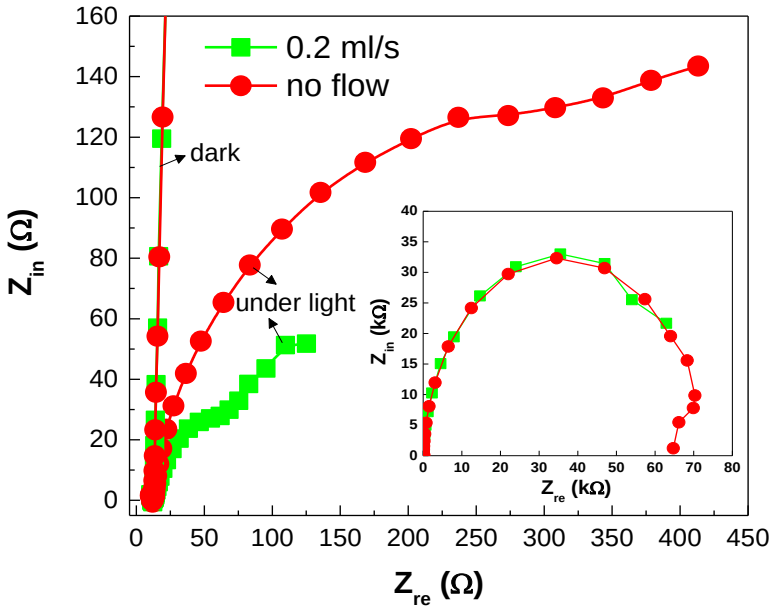

Figure 6-4 EIS spectra of the all-V continuous-flow PESC under dark/illumination and different flow conditions using 0.01 M vanadium redox species. The inset shows the full spectra under dark.

In order to investigate the impact of electrolyte flow rate on the charge-transfer process, EIS was employed to study the all-V PESC under either dark or illumination. The Nyquist plots in Figure 6-4 under dark at different flow conditions essentially overlap indicating negligible influence of electrolyte flow on electrochemical performance under dark. The obtained large diameter (inset of Figure 6-4) of EIS spectra suggests extremely large charge transfer resistance under dark. Upon illumination, the cell, especially under convective flow of electrolyte, shows distinct EIS characteristics since charge carriers have been created. In general, a semicircle in a Nyquist plot represents an electrochemical interface, and the co-existence of plural semicircles indicates combined electrochemical interfaces for charge transport in the electrochemical system [128]. Under illumination with no flow, the EIS spectra bend toward the real axis in comparison to that under dark, suggesting reduced charge transfer resistance. The low-frequency tail (a small portion) may be related to Warburg mass transport resistance due to sluggish diffusion of vanadium redox species. With the introduction of flow, the overall Nyquist plot shrinks and a new semicircle, indicative of a new electrochemical interface, emerges in the intermediate frequency range. This semicircle is believed be related to the charge transfer resistance and interfacial capacitance at the TiO_2/V^{4+} or carbon paper/V^{3+} interfaces, as a result of convective flow of electrolytes at the two electrode surface.

6.3.3 Computational study

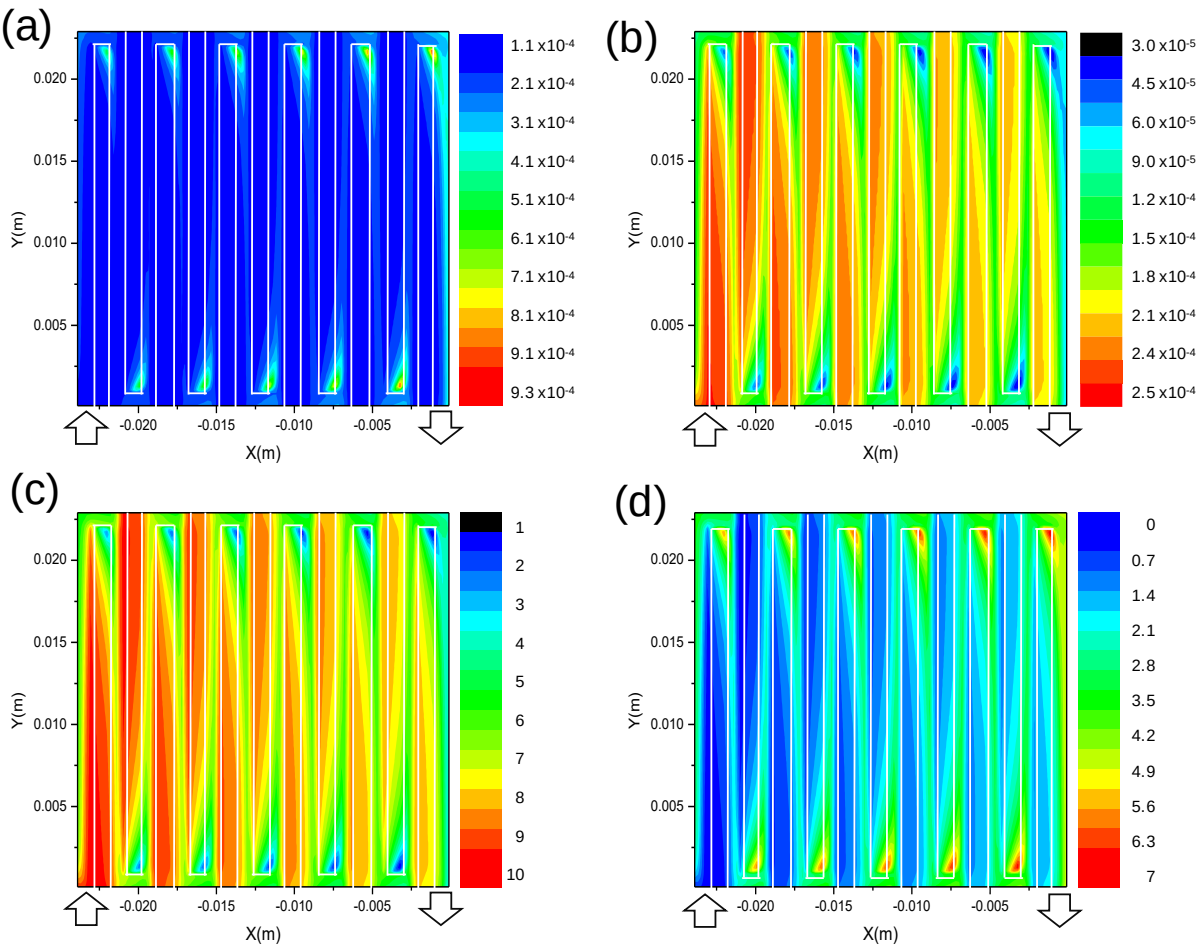

Figure 6-5 Simulated 2D concentration contour (in mole/m^3) of four active species: (a) holes, (b) electrons, (c) V^{4+}, and (d) V^{5+}, under a photocurrent of 0.5 mA and electrolyte flow rate of 0.01 ml/s.

A 3D multi-component PEC model was developed to better understand the convection-enhanced PEC reactions. Figure 6-5 shows the in-plane species distribution, including electrons, photons, V^{4+}, and V^{5+} along the mid-plane of the photoelectrode under a flow rate of 0.01ml/s (V^{4+} at 0.01 M) and a prescribed photocurrent of 0.5 mA. As expected, electrons, holes, and V^{4+} are consumed during the PEC reactions. On the

contrary, V^{5+} redox species (Figure 6-5 (d)), generated by oxidation of V^{4+}, has increased concentration along the serpentine flow channel (the inlet and outlet are indicated on each plot), which is consistent with the V^{4+} concentration contour in Figure 6-5 (c). Besides, as shown in Figure 6-5, where the serpentine flow field is superimposed on top of each figure, clearly shows the drastic impact of flow on species distribution and PEC reaction rate. The area in the photoelectrode immediately after each U-turn of the serpentine flow field appears to achieve the max reaction rate. As seen from Figure 6-5 (c) and (d), the tortuous serpentine flow channel provides better convection at the U-turns and, hence, results in better mass transport of both vanadium redox species and higher reaction rates in the photoelectrode even under the land area. Over the whole active area (1 in x 1 in), the distribution of hole concentration (Figure 6-5 (a)) in the photoelectrode seems to be dependent on that of vanadium redox species. In the steady-state simulation, the area with lower V^{4+} concentration consumes less holes, which results in a relatively higher hole concentration. Besides, the electron concentration distribution in Figure 6-5 (b) seems to be solely dominated by the charge recombination, which is proportional to both electron and hole concentrations. In addition, parallel study conducted for higher flow rates of vanadium electrolyte at 0.05, 0.1, and 2 ml/s showed relatively uniform concentration distribution of different species, reasonably due to a larger supply of V^{4+} to the cell.

On the other hand, complementary to the above simulation on the photoelectrode, steady-state simulation was also performed on the cathode to further unfold the impact of electrolyte flow. In Figure 6-6 the electrode potential E is plotted against the current under different flow rates of the catholyte (0.01M V^{3+}) 0.01 to 0.5 ml/s. The results show that the impact of flow rate on the current, if less than 0.78 mA, is trivial owning to the large stoichiometric coefficients of the supplied V^{3+} at 0.78 mA ranging from 618 at 0.5

ml/s to 12 at 0.01 ml/s. The large stoichiometric coefficients also explain why the polarization curves in Fig. 6 did not show the limiting currents. The impact of catholyte flow rate starts to show up at higher currents because a substantially negative electrode potential is required, particularly for small flow rate of V^{3+}. For the all-V continuous-flow PESC, the cathode overpotential η, as the driving force for reduction reaction of V^{3+}, is defined as $\eta = E_F - E_{V_3-V_2}$, where E_F and $E_{V_3-V_2}$ are the Fermi level electrochemical potential and equilibrium potential of V^{3+}/V^{2+}, respectively. The Fermi level, which depends on a semiconductor's surface properties [142, 143], is estimated to be -0.45 eV (the dash line in Figure 6-6), under which different flow rates of the catholyte essentially produce the same current. This result in turn determines the experimentally observed max photocurrent (Figure 6-2 and 6-3), which is consistent with our experimental study that the PEC performance of the cell does not seem to be affected by the catholyte flow rate within the studied range.

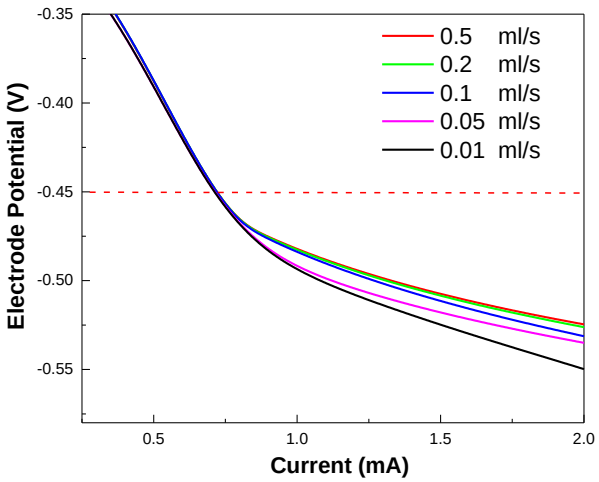

Figure 6-6 Simulated cathode electrode potential as a function of the current for an all-V continuous-flow PESC under different flow rates of V^{3+} (0.01 M). The estimated Fermi level electrochemical potential is indicated in the figure as a dashed line.

6.3.4 Efficiency of long-term photocharging

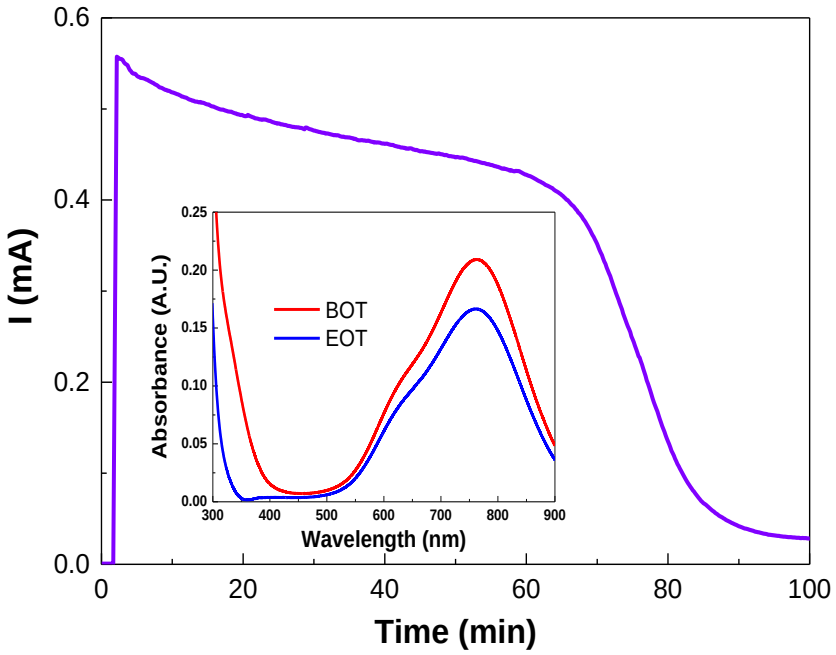

Figure 6-7 Continuous photocharging under AM 1.5 illumination using the all-V continuous-flow PESC of 0.01 M vanadium redox electrolytes. UV-Vis absorbance spectra of the beginning-of-test (BOT) and end-of-test (EOT) anolyte were shown in the inset.

A prolonged photocharging test of the all-V continuous-flow PESC under AM 1.5 illumination for 100 min has been conducted to evaluate its long-term PEC characteristics. As shown in Figure 6-7, the photocurrent of the cell continuous declined during the entire testing window, which could be mostly attributed to the concentration loss and therefore a concentration overpotential particularly at the cathode. Approximately at 60 min, a sharp decrease of the photocurrent occurred mainly due to depletion of the vanadium species.

UV-Vis absorption spectroscopy was adopted to study the vanadium concentration change of the cell. As indicated in Figure 6-7, the absorbance for the starting V^{4+} anolyte at 0.01 M is 0.210, and the absorbance after the test is 0.167, corresponding to V^{4+} concentration of 0.79 M assuming a linear relationship between the electrolyte concentration and absorbance according to the known Lambert-Beer law. The overall cell Faradaic efficiency η_F is calculated to be 95%, which is attributed to fast reaction kinetics of vanadium redox and suppressed H_2/O_2 evolution reactions. The overall solar-chemical-electricity (SCE) conversion efficiency during the first hour of the 1.7h photocharge is estimated to be 0.6 % assuming that the energy conversion efficiency of a VRB is 90%. Though this efficiency seems low, mainly due to the wide bandgap of TiO_2, to the best of our knowledge, it doubles the best solar-hydrogen-electricity efficiency using single semiconductor material. The best unbiased solar-to-hydrogen efficiency using a single-junction PEC/PV device is ~ 1%, which yields an efficiency of only ~ 0.3% in conversion to electricity using a fuel cell with 30% efficiency.

Though a rather shallow charge depth (~20% change in state of charge or SOC) was demonstrated for the 1.7h test, the present study actually represents a significant leap forward over our previous report [129], where only a 6% change of SOC over a 25h period was achieved. This high performance in photocharging is due to the applied forced convective flow in the all-V PESC, which effectively improves the photocurrent and allows for smaller volumes of vanadium redox species to be used. Future research will focus on further improving charge depth of the cell by optimizing the flow channel and cell design.

6.4 Conclusion

This study demonstrate the advantages of continuous-flow feature in the all-V PESC. With no external bias, the photocurrent produced by this newly designed device increased significantly by 5 times in comparison to the static cell, mainly due to the forced

convective flow. Catholyte flow were found to have higher impact on the photoelectrochemical performance of the device than the anolyte flow, which was ascribed their kinetic differences as well as over potential variances. Sharp reduction of charge transfer resistance by the electrolyte flow was manifested by EIS, indicating the limited diffusion was successfully compensated by the forced electrolyte transport. 3D CFD numerical studies have been adopted to provide 2D specific distribution of electrochemical active species during steady state at anode side. On the other hand, flow rates ranged from 0.001 to 0.5ml/s has been provided to the cathode side simulation, in combination with the prescribed photo current, revealing that a minimum photocurrent of 0.78mA is required to be affected by the complicated interplay between the flow rate and photo electrochemical performance. Monitored by UV-vis spectroscopy and demonstrate by photo charging, more than 3 fold increase depth of charge (20% SOC) during 100 min illumination was obtained with the continuous-flow PESC compared to our previous design during 25 hour illumination (6% SOC), while maintaining the 95% faradaic efficiency.

Chapter 7

Conclusion and Future work

7.1 Conclusion

Efficient solar energy storage has been demonstrated using an all-vanadium PESC. First, we demonstrated combining PEC energy storage with a vanadium redox-flow battery (VRB). This PESC utilized fast electrochemical kinetics of vanadium redox couples of VO_2^+/VO^{2+} and V^{3+}/V^{2+}. Continuous photocharging for 25h revealed a VO^{2+} conversion rate of 0.0042 µmol/h and Faradaic efficiency of 95% without external voltage bias. The incident photon-to-current efficiency (IPCE) at 350 nm light was calculated to be ~12%. This design appears as a promising alternative to photocatalytic water splitting

Additionally, we studied carbon-coated TiO_2 as a photoanode in all-V PESC and investigated the performance with different carbon compositions, in an attempt to improve photocurrent of the system. Due to fast PEC reaction kinetics of vanadium redox, a fast electrochemical reaction rate is achieved, rendering a high charge carrier flux in the relatively thick photonaode which requires good conductivity. The applied carbon coating was demonstrated to be beneficial to the overall electrical transport in the photoelectrode of an all-V PESC, as it provides an interconnected conductive layer for the movement of photogenerated charge carriers.

Moreover, a unique stirring-assisted hydrothermal method was developed to synthesize geometry-enhanced TiO_2 nanobelt photocatalyst for all-V PESC. It is discovered that increasing the stirring speed in the hydrothermal synthesis from 0 to 700 rpm creates 4.2 times more exposed high-energy (001) facets resulting in

improved photocatalytic performance. The all-V PESC demonstrated a peak IPCE of ~22% without any external bias, double that of commercial P25 TiO_2 (~11%) that we used in the previous case. The enhanced photocatalytic performance is ascribed to three factors, (i) the improved charge separation efficiency because of the enhanced structure of TNBs, (ii) more exposed high-energy (001)/(100) facets, and (iii) facilitated charge transfer enabled by high electron mobility within the materials.

To further optimize the cell and extend photocharge window, we designed an all-V continuous-flow PESC. Forced convective flow effects showed a large impact on the cell performance with 5 times photocurrent enhancement, 3 times of SOC solar energy conversion compared to the cell with stagnant electrolytes, mainly due to reduced charge transfer resistances in PEC/electrochemical reactions introduced by the forced convective flow. In addition, 3D numerical simulation has been conducted to gain more insights on the cell operation under convective flow of reactants indicating better mass transport is achieved at the U-turns of the tortuous serpentine flow channel of the cell. The results, compared to those using stagnant electrolytes, show great advantages of forced convective electrolyte flow in enhancing the photocurrent for solar energy storage, and particularly depth of photocharging.

7.2 Future Work

Our state of art studies demonstrate the feasibility of using redox pairs to store solar energy. With the advancement of RFB technologies, a wide range of redox pairs can be chosen for solar energy storage purpose as long as their electrochemical potentials match with band energies of the photocatalyst. There are multiple choices of redox couple, providing great flexibility for selecting the photoelctrodes. The ultimate goal is to find a good match between the fast kinetic redox

pairs and highly efficient photocatalyst to satisfy the efficiency requirement towards commercialization.

Our next step is to explore various cost-effective, kinetically favorable combination of redox species to realize more efficient unbiased solar energy conversion and storage such as 9,10-anthraquinone-2,7-disulphonic sodium/1,8-dihydroxy-9,10-anthraquinone-2,7-disulphonic sodium ($AQDS/AQDSH_2$) redox pairs.

The proposed photoelectrochemical reaction is described as:

$$PE + hv \rightarrow e^- + h^+ \quad \text{.....7.1}$$

$$h^+ + VO^{2+} \rightarrow VO_2^+ \quad E_0=1.0V \text{ vs NHE} \quad \text{.....7.2}$$

$$e^- + AQDS + 2H^+ \rightarrow AQDSH_2 \quad E_0=0.2V \text{ vs NHE} \quad \text{.....7.3}$$

The overall reaction is:

$$AQDS + 2H^+ + VO^{2+} \rightarrow AQDSH_2 + VO_2^+ \quad E_0=0.8V \quad \text{.....7.4}$$

Since the $AQDS/ AQDSH_2$ has more positive redox potential ($E_0=0.2V$) than V^{3+}/V^{2+} ($E_0=0.-26V$), it provides more driving force for the PEC reduction of the catholyte.

Appendix

Computational Fluid Dynamics Simulation of All-V Continuous-Flow Cell

1. Numerical simulation

Numerical simulation has been widely employed to study PEC water splitting (1, 2) as well as vanadium flow batteries (VRBs) (3, 4). In the present study of the all vanadium (all-V) continuous-flow PEC storage cell (PESC), the numerical models in the above studies have been adopted to investigate the impact of forced convective flow on performance of the storage cell.

1.1. 3D Steady-state simulation of the photoanode in the all-V Continuous-flow PESC

a. Model assumptions

The model is based on the following assumptions:

1) The electrolyte flow is incompressible and laminar.
2) All elements are isothermal.
3) Hydrogen and oxygen evolution reactions are neglected.
4) The dilute solution approximation is adopted for species transport.
5) The electrolyte density is constant and electrode properties are homogeneous.

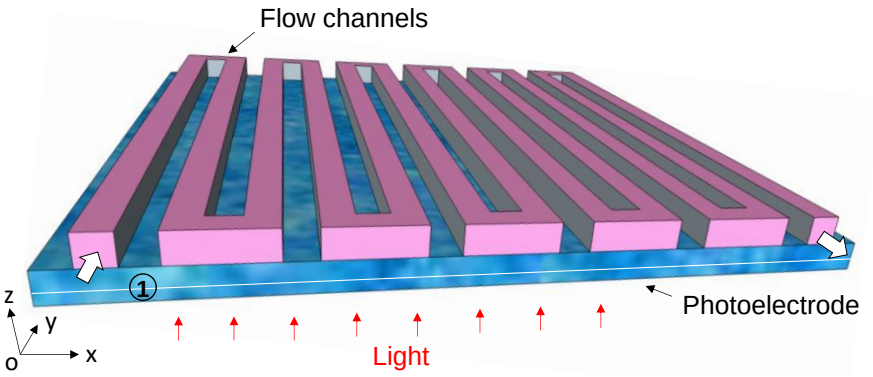

Figure A-1. 3D computational domain of the photoanode of the all-V Continuous-flow PESC (thickness of the photoelectrode not in scale). The symbol ① indicates the mid-plane in the photoelectrode where 2D concentration contour plots of different species were studied.

b. Electrochemical reactions and transport characteristics

Photons with energy higher than the TiO_2 bandgap could generate electron-hole pairs. The photogenerated holes (h^+) oxidize VO^{2+} according to the following reaction:

$$h^+ + VO^{2+} + H_2O \rightarrow VO_2^+ + 2H^+$$

The kinetics of the above light-driven reaction can be described by

$$j_1 = Fk_1 C_h{}^a C_{V^{4+}}{}^b$$

where j_1 is the current density, F is the Faraday's constant, k_1 is the standard rate constant for the photoelectrode, and $C_{V^{4+}}$ and C_h are the concentrations of VO^{2+} and hole, respectively. In this study, first-order reaction kinetics are assumed; therefore, both *a* and *b* are taken as unity.

c. *Governing equations and source terms*

Steady-state simulation was performed on the 3D domain in Figure A-1. The governing equations incorporating the aforementioned electrochemical reaction and the source terms accounting for the species generation/consumption are:

Continuity: $\nabla \cdot \vec{u} = 0$

Momentum: $\frac{1}{\varepsilon^2} \nabla \cdot (\rho \vec{u} \vec{u}) = -\nabla p - \frac{\mu}{K} \vec{u}$

where ρ is the density, ε is the porosity, μ is the electrolyte viscosity, p is pressure, and K is the permeability.

Electrons (only in the photoelectrode)**:**

$$-\nabla \cdot (D_e \nabla C_e) = \frac{\eta_{inj} \alpha(\lambda) I_0 e^{-\alpha(\lambda) z}}{N_A} - k_{recomb} C_e C_h$$

where D_e, C_e, η_{inj}, $\alpha(\lambda)$, I_0, z, and k_{recomb} are electron diffusion coefficient, electron concentration, electron injection efficiency, wavelength-dependent absorption coefficient, incident photon flux, distance to the semiconductor/electrolyte surface (see Figure A-1), and the charge recombination rate constant, respectively. N_A is the Avogadro's number. The 1st and 2nd terms on the RHS stand for the electron generation rate and consumption rate (due to charge recombination), respectively.

Holes (only in the photoelectrode)**:**

$$-\nabla \cdot (D_h \nabla C_h) = \frac{\eta_{inj} \alpha(\lambda) I_0 e^{-\alpha(\lambda) z}}{N_A} - k_{recomb} C_e C_h - a_1 \frac{j_1}{F}$$

where a_1 is the specific active surface area of the photoelectrode (m^2/m^3). The 1st, 2nd, and 3rd terms on the RHS of the above equation represent the electron generation rate,

consumption rate due to charge recombination, and consumption due to photoelectrochemical reaction with VO^{2+}, respectively.

Vanadium VO^{2+}: $\nabla \cdot (\vec{u} C_{V^{4+}}) - \nabla \cdot (D_{V^{4+}}^{eff} \nabla C_{V^{4+}}) = S_{V^{4+}}$

where $S_{V^{4+}} = -a_1 \frac{j_1}{F}$ only in the photoelectrode. The effective diffusion coefficients of vanadium species in the porous electrodes are calculated using the following equation, i.e.,

$$D_i^{eff} = D_i \, \varepsilon^{1.5} .$$

Vanadium VO_2^+: $\nabla \cdot (\vec{u} C_{V^{5+}}) - \nabla \cdot (D_{V^{5+}}^{eff} \nabla C_{V^{5+}}) = S_{V^{5+}}$

where $S_{V^{5+}} = a_1 \frac{j_1}{F}$ only in the photoelectrode.

d. Boundary conditions

The simulation was performed under steady-state conditions with a constant current flowing into the photoelectrode (at $z = 0$ in Figure A-1). Non-flux wall boundary conditions are applied to all other surfaces. Vanadium redox concentrations at the inlet boundary remained constant and velocity varied during the simulation. The simulation was conducted by the SIMPLER algorithm in a commercial CFD software Fluent 6.3.26. User defined functions (UDFs) were written to account for diffusivity and source terms for different species in the photoelectrode and flow channels. Some of the parameters employed in the simulation are listed in Table A1.

Table A-1. Parametric properties used in the simulation (4-6)

Parameters	Value
Standard reaction rate constant, k_1	1.0×10^{-5}
Standard reaction rate constant, k_2	1.25×10^{-7}
Electron injection efficiency, η_{inj}	0.93
incident photon flux, I_0 (#/m²/s)	2.8×10^{21}
Photoanode absorption coefficient, $\alpha@375nm$ (m)	300
Charge recombination rate constant, k_{recomb}	4.8×10^{7}
Porosity of the carbon paper, ε_c	0.78
Porosity of the photoanode, ε_{PE}	0.66
Permeability of the photoanode, K_{PE} (m²)	1.0×10^{-11}
Permeability of the carbon paper, K_c (m²)	5.0×10^{-11}
Specific surface area of photoanode, a_1 (m^{-1})	125000
Specific surface area of carbon paper, a_2 (m^{-1})	12645
Inlet concentration of V^{2+}, $C^0_{V^{2+}}$ (mole/l)	1.0×10^{-7}
Inlet concentration of V^{3+}, $C^0_{V^{3+}}$ (mole/l)	0.01
Inlet concentration of VO^{2+}, $C^0_{V^{4+}}$ (mole/l)	0.01
Inlet concentration of VO_2^+, $C^0_{V^{5+}}$ (mole/l)	1.0×10^{-7}
Active area, (in x in)	1.0 x 1.0
Channel dimension, depth x width (mm x mm)	1.0 x 1.0
Diffusion coefficient of V^{2+}, $D_{V^{2+}}$ (m²/s)	2.4×10^{-10}
Diffusion coefficient of V^{3+}, $D_{V^{3+}}$ (m²/s)	2.4×10^{-10}
Diffusion coefficient of VO^{2+}, $D_{V^{4+}}$ (m²/s)	3.9×10^{-10}
Diffusion coefficient of VO_2^+, $D_{V^{5+}}$ (m²/s)	3.9×10^{-10}

1.2. 3D Steady-state simulation of the cathode in the all-V Continuous-flow PESC

a. Electrochemical reactions

The electrochemical redox reaction occurring in the cathode half-cell is as follows:

$$V^{3+} + e^- \rightarrow V^{2+}$$

The transfer current j_2 for the above reaction is described as (7):

$$j_2 = a_2 F k_2 \left(c_{V^{2+}} c_{V^{3+}}\right)^{0.5} \left[\exp\left(\frac{F}{2RT}\left(E - E_{V_3-V_2}\right)\right) - \exp\left(-\frac{F}{2RT}\left(E - E_{V_3-V_2}\right)\right)\right]$$

where a_2 is the specific active surface area of the carbon paper (m^2/m^3), E is the electrode potential, $E_{V_3-V_2}$ is equilibrium potential of V^{3+}/V^{2+} which is $E_{V_3-V_2} = \frac{RT}{F}\ln(C_{V^{3+}} / C_{V^{2+}}) - 0.255$, and k_2 is the standard rate constants for the cathode. It should be noted that species migration is ignored here (8), because its contribution to species transport is not significant in the redox flow battery according to reference (4).

b. Governing equations and source terms

Simulation was conducted on the 3D domain in Figure A-2. The governing equations for flow, vanadium redox species, and electrode potential are listed in Table A-2.

Table A-2. Governing equations for the transport and electrochemical model

	Equations	Source Terms
Continuity	$\nabla \cdot \vec{u} = 0$	–
Momentum	$\frac{1}{\varepsilon^2}\nabla \cdot (\rho \vec{u}\vec{u}) = -\nabla p + S_u$	$S_u = -\frac{\mu}{K}\vec{u}$
V^{2+}	$\vec{u}\nabla C_{V^{2+}} - D^{eff}_{V^{2+}}\nabla^2 C_{V^{2+}} = S_{V^{2+}}$	$S_{V^{2+}} = -\frac{j_2}{F}$ in electrode
V^{3+}	$\vec{u}\nabla C_{V^{3+}} - D^{eff}_{V^{3+}}\nabla^2 C_{V^{3+}} = S_{V^{3+}}$	$S_{V^{3+}} = \frac{j_2}{F}$ in electrode
Electrode potential	$-\sigma_s^{eff}\nabla^2\phi_s = S_s$	$S_s = -j_2$ in electrode

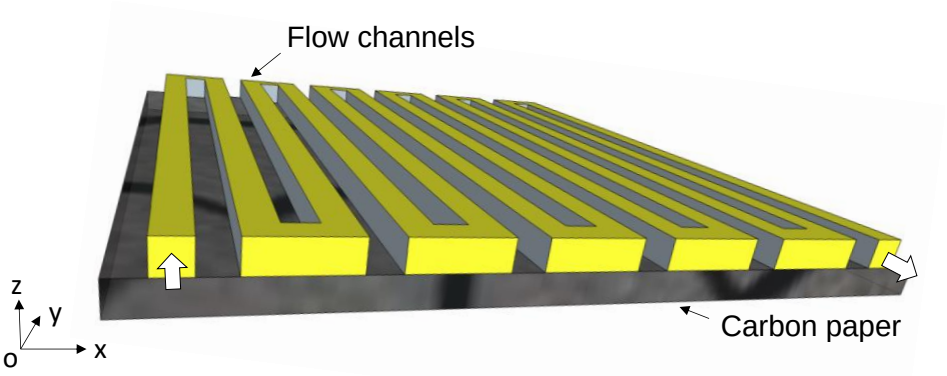

Figure A-2. 3D computational domain of the cathode in the all-V Continuous-flow PESC (thickness of the carbon paper not in scale).

c. Boundary conditions

Steady-state simulation was performed under galvanostatic operation and a constant current density is applied to the carbon paper/current collector interface, i.e., $z = 0$ (Figure A-2)

$$-\sigma_s^{eff} \frac{\partial \phi_s}{\partial x} = -I$$

Non-flux wall boundary conditions are applied to all other surfaces. Vanadium redox concentrations at the inlet boundary remained constant and velocity varied during the simulation.

References

[1] A. Becquerel, Recherches sur les effets de la radiation chimique de la lumière solaire au moyen des courants électriques, Comptes Rendus de LAcadémie des Sciences, 9 (1839) 145-149.

[2] V. Nelson, Wind energy: renewable energy and the environment, CRC Press, 2013.

[3] A.V. Herzog, T.E. Lipman, D.M. Kammen, Renewable energy sources, Encyclopedia of Life Support Systems (EOLSS). Forerunner Volume-'Perspectives and Overview of Life Support Systems and Sustainable Development, (2001).

[4] M. Liserre, T. Sauter, J.Y. Hung, Future Energy Systems: Integrating Renewable Energy Sources into the Smart Power Grid Through Industrial Electronics, Industrial Electronics Magazine, IEEE, 4 (2010) 18-37.

[5] M.A. Green, K. Emery, Y. Hishikawa, W. Warta, E.D. Dunlop, Solar cell efficiency tables (version 47), Progress in Photovoltaics: Research and Applications, 24 (2016) 3-11.

[6] T. Todorov, O. Gunawan, S.J. Chey, T.G. de Monsabert, A. Prabhakar, D.B. Mitzi, Progress towards marketable earth-abundant chalcogenide solar cells, Thin Solid Films, 519 (2011) 7378-7381.

[7] D. Schmidt, M.D. Hager, U.S. Schubert, Photo-Rechargeable Electric Energy Storage Systems, Advanced Energy Materials, 6 (2016) n/a-n/a.

[8] J.R. Swierk, T.E. Mallouk, Design and development of photoanodes for water-splitting dye-sensitized photoelectrochemical cells, Chemical Society Reviews, 42 (2013) 2357-2387.

[9] M. Yu, X. Ren, L. Ma, Y. Wu, Integrating a redox-coupled dye-sensitized photoelectrode into a lithium–oxygen battery for photoassisted charging, Nat Commun, 5 (2014).

[10] W. Guo, X. Xue, S. Wang, C. Lin, Z.L. Wang, An Integrated Power Pack of Dye-Sensitized Solar Cell and Li Battery Based on Double-Sided TiO2 Nanotube Arrays, Nano Letters, 12 (2012) 2520-2523.

[11] M. Yu, W.D. McCulloch, D.R. Beauchamp, Z. Huang, X. Ren, Y. Wu, Aqueous Lithium–Iodine Solar Flow Battery for the Simultaneous Conversion and Storage of Solar Energy, Journal of the American Chemical Society, 137 (2015) 8332-8335.

[12] X. Xia, J. Luo, Z. Zeng, C. Guan, Y. Zhang, J. Tu, H. Zhang, H.J. Fan, Integrated photoelectrochemical energy storage: solar hydrogen generation and supercapacitor, Scientific reports, 2 (2012).

[13] N. Yan, G. Li, X. Gao, Solar rechargeable redox flow battery based on Li2WO4/LiI couples in dual-phase electrolytes, J. Mater. Chem. A, 1 (2013) 7012-7015.

[14] N.S. Lewis, Research opportunities to advance solar energy utilization, Science, 351 (2016).

[15] J. Jean, P.R. Brown, R.L. Jaffe, T. Buonassisi, V. Bulovic, Pathways for solar photovoltaics, Energy & Environmental Science, 8 (2015) 1200-1219.

[16] M.A. Green, A. Ho-Baillie, H.J. Snaith, The emergence of perovskite solar cells, Nat Photon, 8 (2014) 506-514.

[17] H. Zhou, Q. Chen, G. Li, S. Luo, T.-b. Song, H.-S. Duan, Z. Hong, J. You, Y. Liu, Y. Yang, Interface engineering of highly efficient perovskite solar cells, Science, 345 (2014) 542-546.

[18] M. Bhushan, A. Catalano, Polycrystalline Zn3P2 Schottky barrier solar cells, Applied Physics Letters, 38 (1981) 39-41.

[19] L. Dou, J. You, Z. Hong, Z. Xu, G. Li, R.A. Street, Y. Yang, 25th anniversary article: a decade of organic/polymeric photovoltaic research, Advanced Materials, 25 (2013) 6642-6671.

[20] A. Hagfeldt, G. Boschloo, L. Sun, L. Kloo, H. Pettersson, Dye-sensitized solar cells, Chemical reviews, 110 (2010) 6595-6663.

[21] A.J. Nozik, Multiple exciton generation in semiconductor quantum dots, Chemical Physics Letters, 457 (2008) 3-11.

[22] M.B. Smith, J. Michl, Singlet fission, Chemical reviews, 110 (2010) 6891-6936.

[23] O. Khaselev, J.A. Turner, A Monolithic Photovoltaic-Photoelectrochemical Device for Hydrogen Production via Water Splitting, Science, 280 (1998) 425-427.

[24] S. Licht, Multiple Band Gap Semiconductor/Electrolyte Solar Energy Conversion, The Journal of Physical Chemistry B, 105 (2001) 6281-6294.

[25] S.U.M. Khan, M. Al-Shahry, W.B. Ingler, Efficient Photochemical Water Splitting by a Chemically Modified n-TiO2, Science, 297 (2002) 2243-2245.

[26] K. Maeda, Photocatalytic water splitting using semiconductor particles: history and recent developments, Journal of Photochemistry and Photobiology C: Photochemistry Reviews, 12 (2011) 237-268.

[27] J. Tang, A.J. Cowan, J.R. Durrant, D.R. Klug, Mechanism of O-2 Production from Water Splitting: Nature of Charge Carriers in Nitrogen Doped Nanocrystalline TiO2 Films and Factors Limiting O-2 Production, Journal of Physical Chemistry C, 115 (2011) 3143-3150.

[28] C.-C. Hu, Y.-L. Lee, H. Teng, Influence of Indium Doping on the Activity of Gallium Oxynitride for Water Splitting under Visible Light Irradiation, Journal of Physical Chemistry C, 115 (2011) 2805-2811.

[29] R. Abe, M. Higashi, K. Domen, Overall Water Splitting under Visible Light through a Two-Step Photoexcitation between TaON and WO3 in the Presence of an Iodate-Iodide Shuttle Redox Mediator, Chemsuschem, 4 (2011) 228-237.

[30] A. Fujishima, K. Honda, Electrochemical Photolysis of Water at a Semiconductor Electrode, Nature, 238 (1972) 37-38.

[31] F.E. Osterloh, Inorganic materials as catalysts for photochemical splitting of water, Chemistry of Materials, 20 (2007) 35-54.

[32] K. Sivula, F. Le Formal, M. Grätzel, Solar water splitting: progress using hematite (α-Fe2O3) photoelectrodes, ChemSusChem, 4 (2011) 432-449.

[33] F.F. Abdi, R. van de Krol, Nature and light dependence of bulk recombination in Co-Pi-catalyzed BiVO4 photoanodes, The Journal of Physical Chemistry C, 116 (2012) 9398-9404.

[34] C.X. Kronawitter, L. Vayssieres, S. Shen, L. Guo, D.A. Wheeler, J.Z. Zhang, B.R. Antoun, S.S. Mao, A perspective on solar-driven water splitting with all-oxide hetero-nanostructures, Energy & Environmental Science, 4 (2011) 3889-3899.

[35] A. Kudo, Y. Miseki, Heterogeneous photocatalyst materials for water splitting, Chemical Society Reviews, 38 (2009) 253-278.

[36] M. Kitano, M. Hara, Heterogeneous photocatalytic cleavage of water, Journal of Materials Chemistry, 20 (2010) 627-641.

[37] M.D. Hernandez-Alonso, F. Fresno, S. Suarez, J.M. Coronado, Development of alternative photocatalysts to TiO(2): Challenges and opportunities, Energy Environ. Sci., 2 (2009) 1231-1257.

[38] Y. Yang, K. Lee, Y. Kado, P. Schmuki, Nb-doping of TiO2/SrTiO3 nanotubular heterostructures for enhanced photocatalytic water splitting, Electrochemistry Communications, 17 (2012) 56-59.

[39] S. Yang, H. Xue, H. Wang, H. Kou, J. Wang, G. Zhu, Improved efficiency of dye-sensitized solar cells applied with nanostructured N-F doped TiO2 electrode, Journal of Physics and Chemistry of Solids, 73 (2012) 911-916.

[40] W.D. Chemelewski, N.T. Hahn, C.B. Mullins, Effect of Si Doping and Porosity on Hematite's (alpha-Fe2O3) Photoelectrochemical Water Oxidation Performance, Journal of Physical Chemistry C, 116 (2012) 5256-5262.

[41] S. Ameen, M.S. Akhtar, H.-K. Seo, Y.S. Kim, H.S. Shin, Influence of Sn doping on ZnO nanostructures from nanoparticles to spindle shape and their photoelectrochemical properties for dye sensitized solar cells, Chemical Engineering Journal, 187 (2012) 351-356.

[42] X. Zhang, K. Udagawa, Z. Liu, S. Nishimoto, C. Xu, Y. Liu, H. Sakai, M. Abe, T. Murakami, A. Fujishma, Photocatalytic and photoelectrochemical studies on N-doped TiO2 photocatalyst, Journal of Photochemistry and Photobiology a-Chemistry, 202 (2009) 39-47.

[43] X. Wang, G. Liu, Z.-G. Chen, F. Li, G.Q. Lu, H.-M. Cheng, Synthesis and Photoelectrochemical Behavior of Nitrogen-doped NaTaO3, Chemistry Letters, 38 (2009) 214-215.

[44] S. Saremi-Yarahmadi, K.G.U. Wijayantha, A.A. Tahir, B. Vaidhyanathan, Nanostructured alpha-Fe2O3 Electrodes for Solar Driven Water Splitting: Effect of Doping Agents on Preparation and Performance, Journal of Physical Chemistry C, 113 (2009) 4768-4778.

[45] D. Guan, H. Fang, H. Lu, T. Sun, F. Li, M. Liu, Preparation and Doping of Anodic TiO2 Nanotube Array, Progress in Chemistry, 20 (2008) 1868-1879.

[46] I. Cesar, K. Sivula, A. Kay, R. Zboril, M. Graetzel, Influence of Feature Size, Film Thickness, and Silicon Doping on the Performance of Nanostructured Hematite Photoanodes for Solar Water Splitting, Journal of Physical Chemistry C, 113 (2009) 772-782.

[47] H.M. Chen, C.K. Chen, Y.-C. Chang, C.-W. Tsai, R.-S. Liu, S.-F. Hu, W.-S. Chang, K.-H. Chen, Quantum Dot Monolayer Sensitized ZnO Nanowire-Array Photoelectrodes: True Efficiency for Water Splitting, Angewandte Chemie International Edition, 49 (2010) 5966-5969.

[48] P. Shen, X. Liu, S. Jiang, L. Wang, L. Yi, D. Ye, B. Zhao, S. Tan, Synthesis of new N, N-diphenylhydrazone dyes for solar cells: Effects of thiophene-derived pi-conjugated bridge, Dyes and Pigments, 92 (2012) 1042-1051.

[49] E. Hong, J.H. Kim, S. Yu, J.H. Kim, Effect of CdS contents on H-2 production from Pt-(CdS/TiO2) film-typed photocatalysts, Korean Journal of Chemical Engineering, 28 (2011) 1684-1687.

[50] L. Giribabu, V.K. Singh, M. Srinivasu, C.V. Kumar, V.G. Reddy, Y. Soujnya, P.Y. Reddy, Synthesis and photoelectrochemical characterization of a high molar extinction coefficient heteroleptic ruthenium(II) complex, Journal of Chemical Sciences, 123 (2011) 371-378.

[51] J. Chen, F. Bai, J. Wang, L. Sun, Q. Pan, H. Zhang, Theoretical studies of the structures and spectroscopic properties of the photoelectrochemical cell ruthenium sensitizers, C101 and J13, Science China-Chemistry, 55 (2012) 398-408.

[52] Y. Hou, B.L. Abrams, P.C.K. Vesborg, M.E. Björketun, K. Herbst, L. Bech, A.M. Setti, C.D. Damsgaard, T. Pedersen, O. Hansen, J. Rossmeisl, S. Dahl, J.K. Nørskov, I. Chorkendorff, Bioinspired molecular co-catalysts bonded to a silicon photocathode for solar hydrogen evolution, Nat Mater, 10 (2011) 434-438.

[53] Z. Zou, J. Ye, K. Sayama, H. Arakawa, Direct splitting of water under visible light irradiation with an oxide semiconductor photocatalyst, Nature, 414 (2001) 625-627.

[54] H. Kato, K. Asakura, A. Kudo, Highly Efficient Water Splitting into H2 and O2 over Lanthanum-Doped NaTaO3 Photocatalysts with High Crystallinity and Surface Nanostructure, Journal of the American Chemical Society, 125 (2003) 3082-3089.

[55] C. Das, P. Roy, M. Yang, H. Jha, P. Schmuki, Nb doped TiO2 nanotubes for enhanced photoelectrochemical water-splitting, Nanoscale, 3 (2011) 3094-3096.

[56] J. Ye, Z. Zou, A. Matsushita, A novel series of water splitting photocatalysts NiM2O6 (M=Nb,Ta) active under visible light, International Journal of Hydrogen Energy, 28 (2003) 651-655.

[57] K. Domen, A. Kudo, T. Onishi, N. Kosugi, H. Kuroda, Photocatalytic decomposition of water into hydrogen and oxygen over nickel(II) oxide-strontium titanate (SrTiO3) powder. 1. Structure of the catalysts, The Journal of Physical Chemistry, 90 (1986) 292-295.

[58] M. Yoshida, A. Yamakata, K. Takanabe, J. Kubota, M. Osawa, K. Domen, ATR-SEIRAS Investigation of the Fermi Level of Pt Cocatalyst on a GaN Photocatalyst for Hydrogen Evolution under Irradiation, Journal of the American Chemical Society, 131 (2009) 13218-13219.

[59] K. Maeda, K. Teramura, K. Domen, Effect of post-calcination on photocatalytic activity of (Ga1-xZnx)(N1-xOx) solid solution for overall water splitting under visible light, J. Catal., 254 (2008) 198-204.

[60] D. Pfeiffer, The myth of the hydrogen economy, Energy Bulletin, 01/03 (2006).

[61] P.V. Kamat, K. Tvrdy, D.R. Baker, J.G. Radich, Beyond photovoltaics: semiconductor nanoarchitectures for liquid-junction solar cells, Chemical reviews, 110 (2010) 6664-6688.

[62] L. Alibabaei, H. Luo, R.L. House, P.G. Hoertz, R. Lopez, T.J. Meyer, Applications of metal oxide materials in dye sensitized photoelectrosynthesis cells for making solar fuels: Let the molecules do the work, Journal of Materials Chemistry A, 1 (2013) 4133-4145.

[63] T. Hisatomi, J. Kubota, K. Domen, Recent advances in semiconductors for photocatalytic and photoelectrochemical water splitting, Chemical Society Reviews, 43 (2014) 7520-7535.

[64] T. Inoue, A. Fujishima, S. Konishi, K. Honda, Photoelectrocatalytic reduction of carbon dioxide in aqueous suspensions of semiconductor powders, Nature, 277 (1979) 637-638.

[65] M. Halmann, Photoelectrochemical reduction of aqueous carbon dioxide on p-type gallium phosphide in liquid junction solar cells, (1978).

[66] H. Homayoni, W. Chanmanee, N.R. de Tacconi, B.H. Dennis, K. Rajeshwar, Continuous Flow Photoelectrochemical Reactor for Solar Conversion of Carbon Dioxide to Alcohols, Journal of The Electrochemical Society, 162 (2015) E115-E122.

[67] W. Chanmanee, M.F. Islam, B.H. Dennis, F.M. MacDonnell, Solar photothermochemical alkane reverse combustion, Proceedings of the National Academy of Sciences, 113 (2016) 2579-2584.

[68] B. O'regan, M. Grfitzeli, A low-cost, high-efficiency solar cell based on dye-sensitized, nature, 353 (1991) 737-740.

[69] G.K. Mor, K. Shankar, M. Paulose, O.K. Varghese, C.A. Grimes, Use of highly-ordered TiO2 nanotube arrays in dye-sensitized solar cells, Nano letters, 6 (2006) 215-218.

[70] X. Wang, L. Zhi, K. Müllen, Transparent, conductive graphene electrodes for dye-sensitized solar cells, Nano letters, 8 (2008) 323-327.

[71] P. Wang, S.M. Zakeeruddin, J.E. Moser, M.K. Nazeeruddin, T. Sekiguchi, M. Grätzel, A stable quasi-solid-state dye-sensitized solar cell with an amphiphilic ruthenium sensitizer and polymer gel electrolyte, Nature materials, 2 (2003) 402-407.

[72] J.-H. Yum, E. Baranoff, F. Kessler, T. Moehl, S. Ahmad, T. Bessho, A. Marchioro, E. Ghadiri, J.-E. Moser, C. Yi, A cobalt complex redox shuttle for dye-sensitized solar cells with high open-circuit potentials, Nature communications, 3 (2012) 631.

[73] S. Mathew, A. Yella, P. Gao, R. Humphry-Baker, B.F. Curchod, N. Ashari-Astani, I. Tavernelli, U. Rothlisberger, M.K. Nazeeruddin, M. Grätzel, Dye-sensitized solar cells with 13% efficiency achieved through the molecular engineering of porphyrin sensitizers, Nature chemistry, 6 (2014) 242-247.

[74] E. Ghadiri, S.M. Zakeeruddin, A. Hagfeldt, M. Grätzel, J.-E. Moser, Ultrafast charge separation dynamics in opaque, operational dye-sensitized solar cells revealed by femtosecond diffuse reflectance spectroscopy, Scientific Reports, 6 (2016) 24465.

[75] B. Wang, S. Licht, T. Soga, M. Umeno, Stable cycling behavior of the light invariant AlGaAs/Si/metal hydride solar cell, Solar Energy Materials and Solar Cells, 64 (2000) 311-320.

[76] S. Licht, G. Hodes, R. Tenne, J. Manassen, A Light-Variation Insensitive High-Efficiency Solar-Cell, Nature, 326 (1987) 863-864.

[77] M. Sharon, P. Veluchamy, C. Natarajan, D. Kumar, Solar rechargeable battery—principle and materials, electrochimica Acta, 36 (1991) 1107-1126.

[78] P. Liu, Y.l. Cao, G.R. Li, X.P. Gao, X.P. Ai, H.X. Yang, A solar rechargeable flow battery based on photoregeneration of two soluble redox couples, ChemSusChem, 6 (2013) 802-806.

[79] A.Z. Weber, M.M. Mench, J.P. Meyers, P.N. Ross, J.T. Gostick, Q. Liu, Redox flow batteries: a review, Journal of Applied Electrochemistry, 41 (2011) 1137-1164.

[80]http://energy.gov/sites/prod/files/oeprod/DocumentsandMedia/OE_Energy_Storage_Program_Plan_Feburary_2011v3.pdf.

[81] M. Yu, W.D. McCulloch, Z. Huang, B.B. Trang, J. Lu, K. Amine, Y. Wu, Solar-powered electrochemical energy storage: an alternative to solar fuels, Journal of Materials Chemistry A, (2016).

[82] G. Hodes, J. Manassen, D. Cahen, Photoelectrochemical energy conversion and storage using polycrystalline chalcogenic electrodes, Nature, 261 (1976) 403.

[83] S. Licht, G. Hodes, R. Tenne, J. Manassen, A light-variation insensitive high efficiency solar cell, (1987).

[84] A. Hauch, A. Georg, U.O. Krašovec, B. Orel, Photovoltaically self-charging battery, Journal of the Electrochemical Society, 149 (2002) A1208-A1211.

[85] Y. Saito, A. Ogawa, S. Uchida, T. Kubo, H. Segawa, Energy-storable dye-sensitized solar cells with interdigitated nafion/polypyrrole-Pt comb-like electrodes, Chemistry Letters, 39 (2010) 488-489.

[86] N. Yan, G. Li, X. Gao, Electroactive Organic Compounds as Anode-Active Materials for Solar Rechargeable Redox Flow Battery in Dual-Phase Electrolytes, Journal of The Electrochemical Society, 161 (2014) A736-A741.

[87] L. Li, S. Kim, W. Wang, Z. Yang, Advanced Redox Flow Batteries for Stationary Electrical Energy Storage, US Department of Energy, (2012).

[88] Y. Tachibana, L. Vayssieres, J.R. Durrant, Artificial photosynthesis for solar water-splitting, Nat Photon, 6 (2012) 511-518.

[89] J. Reichman, M.A. Russak, I-V Behavior of the CdSe/Sulfide-Polysulfide and CdSe/Ferro-Ferricyanide Photoelectrochemical Systems, Journal of The Electrochemical Society, 131 (1984) 796-798.

[90] G. Kear, A.A. Shah, F.C. Walsh, Development of the all-vanadium redox flow battery for energy storage: a review of technological, financial and policy aspects, International Journal of Energy Research, (2011) n/a-n/a.

[91] G. Kear, A.A. Shah, F.C. Walsh, Development of the all-vanadium redox flow battery for energy storage: a review of technological, financial and policy aspects, International Journal of Energy Research, 36 (2011) 1105-1120.

[92] D. Liu, F. Liu, J. Liu, Effect of vanadium redox species on photoelectrochemical behavior of TiO2 and TiO2/WO3 photo-electrodes, J. Power Sources, 213 (2012) 78-82.

[93] Q.H. Liu, G.M. Grim, A.B. Papandrew, A. Turhan, T.A. Zawodzinski, M.M. Mench, High Performance Vanadium Redox Flow Batteries with Optimized Electrode Configuration and Membrane Selection, Journal of The Electrochemical Society, 159 (2012) A1246-A1252.

[94] M. Skyllas-Kazacos, M. Kazacos, State of charge monitoring methods for vanadium redox flow battery control, Journal of Power Sources, 196 (2011) 8822-8827.

[95] T. Hisatomi, T. Minegishi, K. Domen, Kinetic Assessment and Numerical Modeling of Photocatalytic Water Splitting toward Efficient Solar Hydrogen Production, Bull. Chem. Soc. Jpn., 85 (2012) 647-655.

[96] D. Aaron, C.-N. Sun, M. Bright, A.B. Papandrew, M.M. Mench, T.A. Zawodzinski, In Situ Kinetics Studies in All-Vanadium Redox Flow Batteries, ECS Electrochemistry Letters, 2 (2013) A29-A31.

[97] N.H. Choi, S.-k. Kwon, H. Kim, Analysis of the Oxidation of the V(II) by Dissolved Oxygen Using UV-Visible Spectrophotometry in a Vanadium Redox Flow Battery, Journal of The Electrochemical Society, 160 (2013) A973-A979.

[98] T. Tsumura, N. Kojitani, I. Izumi, N. Iwashita, M. Toyoda, M. Inagaki, Carbon coating of anatase-type TiO 2 and photoactivity, Journal of Materials Chemistry, 12 (2002) 1391-1396.

[99] Y.-F. Lee, K.-H. Chang, C.-C. Hu, K.-M. Lin, Synthesis of activated carbon-surrounded and carbon-doped anatase TiO 2 nanocomposites, Journal of Materials Chemistry, 20 (2010) 5682-5688.

[100] Y. Miseki, A. Kudo, Water Splitting over New Niobate Photocatalysts with Tungsten-Bronze-Type Structure and Effect of Transition Metal-Doping, ChemSusChem, 4 (2011) 245-251.

[101] Z. Zhang, Y. Zhou, Y. Zhang, S. Zhou, J. Shi, J. Kong, S. Zhang, Well-crystallized mesoporous TiO 2 shells for enhanced photocatalytic activity: prepared by carbon coating and silica-protected calcination, Dalton Transactions, 42 (2013) 5004-5012.

[102] R. Leary, A. Westwood, Carbonaceous nanomaterials for the enhancement of TiO< sub> 2</sub> photocatalysis, Carbon, 49 (2011) 741-772.

[103] Y. Tamaura, N. Hasegawa, M. Kojima, T. Sano, M. Tsuji, Stoichiometry of H< sub> 2</sub> evolution in the 2-step water splitting by a CIO-layered Ni (II)-ferrite, International journal of hydrogen energy, 22 (1997) 567-573.

[104] D. Liu, Z. Wei, C.-j. Hsu, Y. Shen, F. Liu, Efficient Solar Energy Storage Using A TiO2/WO3 Tandem Photoelectrode in An All-vanadium Photoelectrochemical Cell, Electrochimica Acta, 136 (2014) 435-441.

[105] D. Liu, W. Zi, S.D. Sajjad, C. Hsu, Y. Shen, M. Wei, F. Liu, Reversible Electron Storage in an All-Vanadium Photoelectrochemical Storage Cell: Synergy between Vanadium Redox and Hybrid Photocatalyst, ACS Catal., 5 (2015) 2632-2639.

[106] Z. Wei, D. Liu, Y. Shen, H. Chia-jen, F. Liu, Carbon Coated TiO2 Photoanodes for All-vanadium Redox Photoelectrochemical Cells as Efficient Solar Energy Storage Device, ECS Transactions, 66 (2015) 213-221.

[107] Z. Wei, D. Liu, C. Hsu, F. Liu, All-Vanadium Redox Photoelectrochemical Cell: An Approach to Store Solar Energy, Electrochem. Commun., 45 (2014) 4.

[108] Y.-C. Pu, G. Wang, K.-D. Chang, Y. Ling, Y.-K. Lin, B.C. Fitzmorris, C.-M. Liu, X. Lu, Y. Tong, J.Z. Zhang, Y.-J. Hsu, Y. Li, Au Nanostructure-Decorated TiO2 Nanowires Exhibiting Photoactivity Across Entire UV-visible Region for Photoelectrochemical Water Splitting, Nano Lett., 13 (2013) 3817-3823.

[109] J. Yan, G. Wu, N. Guan, L. Li, Z. Li, X. Cao, Understanding the effect of surface/bulk defects on the photocatalytic activity of TiO2: anatase versus rutile, Physical Chemistry Chemical Physics, 15 (2013) 10978-10988.

[110] W. Zhou, Z. Yin, Y. Du, X. Huang, Z. Zeng, Z. Fan, H. Liu, J. Wang, H. Zhang, Synthesis of Few-Layer MoS2 Nanosheet-Coated TiO2 Nanobelt Heterostructures for Enhanced Photocatalytic Activities, Small, 9 (2013) 140-147.

[111] X. Feng, K. Zhu, A.J. Frank, C.A. Grimes, T.E. Mallouk, Rapid Charge Transport in Dye-Sensitized Solar Cells Made from Vertically Aligned Single-Crystal Rutile TiO2 Nanowires, Angew. Chem., 124 (2012) 2781-2784.

[112] H.G. Yang, C.H. Sun, S.Z. Qiao, J. Zou, G. Liu, S.C. Smith, H.M. Cheng, G.Q. Lu, Anatase TiO2 single crystals with a large percentage of reactive facets, Nature, 453 (2008) 638-641.

[113] D.L. Liao, B.Q. Liao, Shape, size and photocatalytic activity control of TiO2 nanoparticles with surfactants, J. Photochem. Photobiol. A, 187 (2007) 363-369.

[114] N. Roy, Y. Sohn, D. Pradhan, Synergy of Low-Energy {101} and High-Energy {001} TiO2 Crystal Facets for Enhanced Photocatalysis, ACS Nano, 7 (2013) 2532-2540.

[115] C. Hsu, Y. Shen, Z. Wei, D. Liu, F. Liu, Anatase TiO2 nanobelts with plasmonic Au decoration exhibiting efficient charge separation and enhanced activity, Journal of Alloys and Compounds, 613 (2014) 117-121.

[116] Y. Tang, Y. Zhang, J. Deng, J. Wei, H.L. Tam, B.K. Chandran, Z. Dong, Z. Chen, X. Chen, Mechanical Force-Driven Growth of Elongated Bending TiO2-based Nanotubular Materials for Ultrafast Rechargeable Lithium Ion Batteries, Adv. Mater., 26 (2014) 6111-6118.

[117] D. Liu, Z. Wei, Y. Shen, S.D. Sajjad, Y. Hao, F. Liu, Ultra-long electron lifetime induced efficient solar energy storage by an all-vanadium photoelectrochemical storage cell using methanesulfonic acid, Journal of Materials Chemistry A, (2015).

[118] J. Wang, D.N. Tafen, J.P. Lewis, Z. Hong, A. Manivannan, M. Zhi, M. Li, N. Wu, Origin of Photocatalytic Activity of Nitrogen-Doped TiO2 Nanobelts, JACS, 131 (2009) 12290-12297.

[119] K. Biswas, B. Das, C.N.R. Rao, Growth Kinetics of ZnO Nanorods: Capping-Dependent Mechanism and Other Interesting Features, J Phys Chem C, 112 (2008) 2404-2411.

[120] J. Pan, G. Liu, G.Q. Lu, H.-M. Cheng, On the True Photoreactivity Order of {001}, {010}, and {101} Facets of Anatase TiO2 Crystals, Angew. Chem. Int. Ed., 50 (2011) 2133-2137.

[121] B. Wu, C. Guo, N. Zheng, Z. Xie, G.D. Stucky, Nonaqueous Production of Nanostructured Anatase with High-Energy Facets, JACS, 130 (2008) 17563-17567.

[122] A.S. Barnard, L.A. Curtiss, Prediction of TiO2 Nanoparticle Phase and Shape Transitions Controlled by Surface Chemistry, Nano Lett., 5 (2005) 1261-1266.

[123] R. Baddour-Hadjean, J.-P. Pereira-Ramos, Raman Microspectrometry Applied to the Study of Electrode Materials for Lithium Batteries, Chem. Rev., 110 (2010) 1278-1319.

[124] F. Tian, Y. Zhang, J. Zhang, C. Pan, Raman Spectroscopy: A New Approach to Measure the Percentage of Anatase TiO2 Exposed (001) Facets, J Phys Chem C, 116 (2012) 7515-7519.

[125] C. Ding-Wen, E. Martin, R.E. David, W. Vanessa, R.E. García, Validity of the Bruggeman relation for porous electrodes, Modell. Simul. Mater. Sci. Eng., 21 (2013) 074009.

[126] Z. Zhao, J. Tian, Y. Sang, A. Cabot, H. Liu, Structure, Synthesis, and Applications of TiO2 Nanobelts, Adv. Mater., 27 (2015) 2557-2582.

[127] I. Abayev, A. Zaban, F. Fabregat-Santiago, J. Bisquert, Electronic conductivity in nanostructured TiO2 films permeated with electrolyte, Phys Status Solidi A, 196 (2003) R4-R6.

[128] Y.R. Ahn, C.R. Park, S.M. Jo, D.Y. Kim, Enhanced charge-discharge characteristics of RuO2 supercapacitors on heat-treated TiO2 nanorods, Applied Physics Letters, 90 (2007) 122106.

[129] Z. Wei, D. Liu, C. Hsu, F. Liu, All-vanadium redox photoelectrochemical cell: An approach to store solar energy, Electrochemistry Communications, 45 (2014) 79-82.

[130] D. Liu, Z. Wei, S.D. Sajjad, C. Hsu, Y. Shen, M. Wei, F. Liu, Reversible Electron Storage in an All-Vanadium Photoelectrochemical Storage Cell: Synergy between Vanadium Redox and Hybrid Photocatalyst, ACS Catalysis, (2015).

[131] B. Sun, M. Skyllas-Kazakos, Chemical modification and electrochemical behaviour of graphite fibre in acidic vanadium solution, Electrochimica Acta, 36 (1991) 513-517.

[132] J. Ronge, D. Nijs, S. Kerkhofs, K. Masschaele, J.A. Martens, Chronoamperometric study of membrane electrode assembly operation in continuous flow photoelectrochemical water splitting, Physical Chemistry Chemical Physics, 15 (2013) 9315-9325.

[133] Q. Xu, T.S. Zhao, Determination of the mass-transport properties of vanadium ions through the porous electrodes of vanadium redox flow batteries, Physical Chemistry Chemical Physics, 15 (2013) 10841-10848.

[134] A. Khazaeli, A. Vatani, N. Tahouni, M.H. Panjeshahi, Numerical investigation and thermodynamic analysis of the effect of electrolyte flow rate on performance of all vanadium redox flow batteries, Journal of Power Sources, 293 (2015) 599-612.

[135] S.R. Pendlebury, A.J. Cowan, M. Barroso, K. Sivula, J. Ye, M. Gratzel, D.R. Klug, J. Tang, J.R. Durrant, Correlating long-lived photogenerated hole populations with photocurrent densities in hematite water oxidation photoanodes, Energy & Environmental Science, 5 (2012) 6304-6312.

[136] Y. Tamaki, A. Furube, M. Murai, K. Hara, R. Katoh, M. Tachiya, Direct Observation of Reactive Trapped Holes in TiO2 Undergoing Photocatalytic Oxidation of Adsorbed Alcohols: Evaluation of the Reaction Rates and Yields, Journal of the American Chemical Society, 128 (2006) 416-417.

[137] A.J. Cowan, J. Tang, W. Leng, J.R. Durrant, D.R. Klug, Water Splitting by Nanocrystalline TiO2 in a Complete Photoelectrochemical Cell Exhibits Efficiencies Limited by Charge Recombination, The Journal of Physical Chemistry C, 114 (2010) 4208-4214.

[138] A. Hagfeldt, H. Lindström, S. Södergren, S.-E. Lindquist, Photoelectrochemical studies of colloidal TiO2 films: The effect of oxygen studied by photocurrent transients, Journal of Electroanalytical Chemistry, 381 (1995) 39-46.

[139] H. Al-Fetlawi, A. Shah, F. Walsh, Non-isothermal modelling of the all-vanadium redox flow battery, Electrochimica Acta, 55 (2009) 78-89.

[140] A. Shah, R. Tangirala, R. Singh, R. Wills, F. Walsh, A dynamic unit cell model for the all-vanadium flow battery, Journal of the Electrochemical society, 158 (2011) A671-A677.

[141] C.-Y. Wang, Fundamental models for fuel cell engineering, Chemical reviews, 104 (2004) 4727-4766.

[142] C. Fàbrega, D. Monllor-Satoca, S. Ampudia, A. Parra, T. Andreu, J.R. Morante, Tuning the Fermi Level and the Kinetics of Surface States of TiO2 Nanorods by Means of Ammonia Treatments, The Journal of Physical Chemistry C, 117 (2013) 20517-20524.

[143] I. Mora-Seró, J. Bisquert, Fermi Level of Surface States in TiO2 Nanoparticles, Nano Letters, 3 (2003) 945-949.

[144] M. Ni, M.K.H. Leung, D.Y.C. Leung, K. Sumathy, A review and recent developments in photocatalytic water-splitting using for hydrogen production, Renewable and Sustainable Energy Reviews, 11 (2007) 401-425.

Biographical Information

Zi Wei received her BEng from Wuhan Institute of Technology in 2011. She is currently a PhD candidate at the Electrochemical Energy Laboratory in the Department of Materials Science and Engineering. She has been the recipient of many awards, including numerous scholarships and fellowships. Her current research mainly focuses on photoelectrochemical materials and devices for efficient solar energy storage, Li-ion batteries, and redox flow batteries.

PUBLICATIONS

JOURNALS

1. **Wei, Z**.; Liu, D.; Hsu, C.; Liu, F.; All-vanadium redox photoelectrochemical cell: An approach to store solar energy, **Electrochemistry Communications** 2014

2. Hsu, C.; Shen, Y.; **Wei, Z**.; Liu, D.; Liu, F.; Anatase TiO_2 nanobelts with plasmonic Au decoration exhibiting efficient charge separation and enhanced activity, **Journal of Compounds and Alloys** 2014

3. Liu, D.; **Wei, Z**.; Hsu, C.; Shen, Y.; Liu, F.; Efficient Solar Energy Storage Using A TiO_2/WO_3 Tandem Photoelectrode in An All-vanadium Photoelectrochemical Cell, **Electrochimica Acta** 2014

4. Liu, D.; **Wei, Z**.; Sajjad, S, D.; Hsu, C.; Shen, Y.; Wei, M.; Liu, F.; Reversible Electron Storage in an All-Vanadium Photoelectrochemical Storage Cell: Synergy between Vanadium Redox and Hybrid Photocatalyst, **ACS Catal** 2015

5. Siddique, N.A.; Salehi, A.; **Wei, Z**.; Liu, D.; Sajjad, S.D.; Liu, F.; Length-scale Dependent Phase Transformation of $LiFePO_4$: An In situ and Operando Study Using Micro Raman Spectroscopy and XRD, **Chem Phys Chem** 2015

6. **Wei, Z**.; Liu, D.; Shen, Y.; Hsu, C.; Liu, F.; Carbon Coated TiO_2 Photoanodes for All-vanadium Redox Photoelectrochemical Cells as Efficient Solar Energy Storage Device, **ECS Transactions** 2015

7. Sajjad, S.D.; Liu, D.; **Wei, Z**.; Sakri, S.; Shen, Y.; Hong, Y.; Liu, F.; Guanidinium Based Blend Anion Exchange Membranes for Direct Methanol Alkaline Fuel Cells DMAFCs, **Journal of Power Sources** 2015 (IF 6.217)

8. Liu, D.; **Wei, Z**.; Shen, Y.; Sajjad, S.D.; Hao, Y.; Liu, F.; Ultra-long electron lifetime induced efficient solar energy storage by an all-vanadium photoelectrochemical storage cell using methanesulfonic acid, **Journal of Mater Chemistry. A** 2015 (IF 7.443)

9. Vishwakarma, V.; Waghela, C.; **Wei, Z**.; Nagpure, R.P.S.; Li, J.; Liu, F.; Daniel, C.; Jain, A.; Heat Transfer Enhancement in a Li-ion Cell Through Improved Material-Level Thermal Transport, **Journal of Power Sources** 2015 (IF 6.217)

10. Liu, F.; Liu, D.; **Wei, Z**.; Efficient solar energy storage for light and dark conditions **SPIE** 2015

11. Hsu, C.; Wei, M.; **Wei, Z**.; Liu, F.; Improving the catalytic activity of Au/Pd core–shell nanoparticles with a tailored Pd structure for formic acid oxidation reaction, **RSC Advances** 2016

12. **Wei, Z**.; Shen, Y.; Liu, D.; Hsu, C.; Sajjad, S.D; Liu, F.; Geometry-Enhanced Ultra-long TiO_2 Nanobelts in an All-Vanadium Photoelectrochemical Cell for Efficient Storage of Solar Energy, **Nano Energy**, 2016

13. Xu, C.; **Wei, Z**.; Liu, F.; Bugarin, A.; Hong, Y.; Synthesis and Characterization of Conductive, Biodegradable, Elastomeric Polyurethanes for Biomedical Applications, **Journal of Biomedical Materials Research**, 2016

14. **Wei, Z**.; Siddique, N.A. ; Liu, D.; Sakri, S.; Sajjad, S.D.; Shen, Y.; Liu, F.; Numerical Study of Effect of Membrane Properties on Long-cycle Performance of Vanadium Redox Flow Batteries, **Advances in Energy Research**, Under review

15. Xu, C.; **Wei, Z**.; Liu, F.; Bugarin, A.; Hong, Y.; Dopant-free conductive bioelastomers, In preparation

16. **Wei, Z**.; Liu, F.; In-situ harvesting solar energy by an all-vanadium photo electrochemical continuous flow storage cell, In preparation

CONFERENCES:

1. **Zi Wei**, Dong Liu and Fuqiang Liu, All-vanadium Redox Photo-electrochemical Cell: An New Approach to Store Solar Energy, The 49th anniversary TSM meeting, 2014, Arlington

2. **Zi Wei**, Dong Liu, Yi Shen and Fuqiang Liu, Enhanced Photoactivity using TiO_2 nanobelts in an All Vanadium Redox Photoelectrochemical Cell, The 50th anniversary TSM meeting, 2015, Austin

3. **Zi Wei** and Fuqiang Liu, All-vanadium redox Photo-electrochemical Cell, ACES, 2015, Arlington

4. **Zi Wei**, Yi Shen, Dong Liu and Fuqiang Liu, An Efficient Solar Energy Storage System: All Vanadium Redox Photoelectrochemical Cell, The 227th ECS Conference, 2015, Chicago

5. **Zi Wei** and Fuqiang Liu, Improved Solar Energy Storage Efficiency of All-Vanadium Photoelectrochemical Cell using Geometry-Enhanced TiO_2 Nanobelts, AVS, 2015, Dallas

6. **Zi Wei**, Yi Shen, Dong Liu and Fuqiang Liu, Improved solar energy storage efficiency of all vanadium photoelctrochemical cell, The 51th anniversary TSM meeting, 2016, Houston

INVENTIONS:

1. Liu, F.; Liu, D.; **Wei, Z.**; Shen, Y.; Photoelectrochemical Energy Harvesting and Storage Cell, US 62/162,976

2. Vishwakarma, V.; **Wei, Z**.; Liu, F.; Jain, A.; Enhancement of Rate-limiting Interfacial Thermal Conduction in Cell Batteries, US 62/218,854